The Development of a Fluorescent Optical Ammonia Gas Sensor based on FRET Mechanisms embedded in Xerogel Matrices

Inauguraldissertation

zur

Erlangung der Würde eines Doktors der Philosophie

vorgelegt der

Philosophisch-Naturwissenschaftlichen Fakultät

der Universität Basel

von

Susanne Widmer

aus Gränichen AG, Schweiz

St.Gallen, 2015

Genehmigt von der Philosophisch-Naturwissenschaftlichen Fakultät
auf Antrag von

Prof. Dr. Edwin C. Constable

Prof. Dr. Oliver S. Wenger

Basel, den 15. September 2015

Prof. Dr. Jörg Schibler

Dekan

Table of Contents

Acknowledgement

This section gives me the great opportunity to express my gratitude to all those people who contributed to this work.

I must begin with my first supervisor Lukas Scherer and thank him for giving me a place in his research group at Empa. I was lucky in getting a beautiful project in terms of the very colourful and luminescent chemistry. His enthusiasm for research and science was very infectious and he managed to promote my creativity during this project. With the office door always open he took unpredictitable long, but exciting discussions on recently performed experiments into account. When he had time, he made a tour through our labs during which he was asking challenging questions about the experiments that led to thinking and smoking heads when he left again. His fascinating way to solve chemical problems and to develop new ideas always was an inspiration for me. I am very grateful that he continued his support and interest on the thesis although he left Empa to face a new professional challenge.

Luciano Boesel became the new head of the group. He familiarised himself quickly with the new topics and supported me until the end of my time at Empa, thanks!

I would like to thank René Rossi for the opportunity to work in this multisided department that offered me the freedom to explore the world of smart textiles and chemistry.

With Prof. Ed. Constable as the second supervisor from Uni Basel I had the benefit of great experience and knowledge. I enjoyed my early trips to Basel for attending the Constable/Housecroft research group meetings. It was great to get an insight into the complex coordination chemistry aming the efficient use and conversion of energy.

I am indebted to Prof. Catherine Housecroft for proof-reading of this thesis and the publication manuscripts. I thank her a lot for taking the time for doing this and her valuable and helpful advices.

I am also very thankful to Prof. Oliver Wenger for being my co-referee and co-examiner.

A close collaboration was done with the Brühwiler's group at ZHAW. With Dominik Brühwiler's and Michael Reber's great expertise on silica particles I managed to explain the findings in the second publication. Special thanks go to Michael for performing all the N_2-sorption and CLSM measurements.

The co-condensed silica material was provided by Patrick Müller, who was the second Bachelor student from ZHAW I was allowed to supervise for 2 months at Empa. I thank him for his patience and his endurance in performing the sensor experiments. He had to apply a lot of finesse in preparing the samples. When he left I missed his critical questions on the experiments that always led to nice scientific discussions.

The first Bachelor student from ZHAW I supervised was Emir Cetojevic. He did a great job (which is not included in this thesis) and has been a very pleasent person to work with.

The help and the support of the people in the lab at Empa was great at any time. The three years I spent at Empa were unforgettable and it was nice to meet people of different cultures.

I am grateful to Agathe Camerlo and Marco Dorrestijn, who did the first ammonia exposure experiments on dye-doped xerogels in the framework of a master thesis. Their great results were the starting basis for my PhD project.

Lea Bommer became my office-mate during the last year. She has always been taking care of the lab order. I thank her for that since I know that it is not always easy to assert oneself against a number of crazy scientists. Today, I am lucky to consider her one of my best friends.

I would like to thank Maike Quandt-Britt and Marek Krehel for explaining me the basics on optical fibres and related measurement techniques.

Most calibration curves were done by Karl Kehl, who always greeted me with a tricksy smile when I entered his lab. I must not forget Elisabeth Michel, a very kind-hearted woman, who helped me finding disappeared chemicals and lab materials. I am very thankful for their lovely and caring intercourse.

Going to the second lowest floor, you meet nice people from the Empa intern workshop. Jörg Gschwend, Lino Missaggia and Ernst Rüegg were very patient in listening to my wishs concerning the design of the sensors. Especially if one considers that I had no idea of electronic components and no information about any measurement conditions but just a fixed vision in mind how the sensor should finally perform. With a wide grin on their faces they took note of my expectations and did their best to realize them, thanks!!!

Rolf Stämpfli, Michel Schmid and Sebastian Lehner helped me to install the sensor components and adapted the circuit diagram if neccessary. I thank them for their great and spontaneous help.

All the AFM, lifetime and quantum yield experiments were performed at Uni Basel. Niamh Murray was so kind to do the AFM measurements which certainly required a lot of time. Jonas Schönle competently explained me the lifetime and quantum yield measurements and made sure that the lab door was always open for me. Generally I felt very welcome in this group.

I would like to offer particular thanks to my family. Without their love, support and motivation I would never had achieved all that.

A special thank goes to my boyfriend who had the patience and energy to discuss some sensor results far into the night. He spent a lot of time on explaining me the function of some electronic components and circuits. Our guests at home were really impressed when they discovered our wall chart completely scribbled of sensor responses and impressive equations.

ABSTRACT

This thesis contains the development of optical-based *planar* and *fibre waveguide* ammonia gas sensor prototypes. The sensing mechanism is based on the change of the fluorescence emission intensities of selected dye pairs caused by ammonia which is due to the Förster resonance energy transfer (FRET) between the dyes.

Chapter 1 introduces the reasons for investigating optical ammonia sensors. It highlights the advantage of fluorescence-based optical sensors and discusses the theoretical basics and sensor platform technologies connected to this topic.

Chapter 2 focuses on the development of an optical planar waveguide ammonia gas sensor, the sensing mechanism of which is based on FRET between coumarin and fluorescein. The dyes were immobilized into an organically modified silicate matrix during polymerizing methyltriethoxysilane with trifluoropropyl-trimethoxysilane on a PMMA substrate. The resulting dye-doped xerogel films were exposed to different gaseous ammonia concentrations. A logarithmic decrease in coumarin fluorescence emission intensity was observed with increasing ammonia concentration. The coumarin/fluorescein composition was optimized in order to obtain the best ammonia sensitivity. Experiments in the gas sensor setup demonstrated a sensitive and reversible response of the xerogel films to gaseous ammonia.

Chapter 3 reports on the development of silica particle impregnated xerogel sensor coatings on PMMA substrates. Fluorescein and rhodamine B labelled mesoporous silica particles were synthesized by post-grafting and co-condensation approaches. The resulting materials exhibited different pore size distributions, particle shapes and sizes. The Förster resonance energy transfer between this dye pair was explored for the different materials by exposure to various concentrations of gaseous ammonia. A logarithmic increase in rhodamine B emission intensity with increasing ammonia concentration was observed for both post-grafted and co-condensed materials. The dye accessibility by ammonia gas in the silica framework was evaluated by the same gas sensor setup reported in Chapter 2. The response to ammonia gas and the recovery with nitrogen gas is explained by comparing the structure properties and dye loading of the materials.

Chapter 4 contains the development an optical fibre waveguide ammonia gas sensor. The sensor performance of a PMMA fibre clad with the FITC and RBITC doped xerogel reported in Chapter 3 was investigated. The results of the preliminary fibre sensor measurements and the suitability of this system for wearable applications are discussed.

Chapter 5 concludes the thesis by highlighting the most important results and discussing possible experiments or procedures for the improvement of the ammonia gas sensor performance.

Abbreviations and Symbols

A	A	acceptor
	Å	Angström
	AFM	atomic force microscopy
	APTES	3-aminopropyltriethoxysilane
	aq.	aqueous
	arb. unit	arbitrary units
	ATR	attenuated total reflection
B	BET	Brunauer-Emmett-Teller
C	C	7-diethylamino-4-methylcoumarin/coumarin
	C_{AcH}	7-(diethylamino)coumarin-3-carboxylic acid
	C_{CA}	7-(diethylamino)coumarin-3-carboxylic acid
	C/F	coumarin and fluorescein doped
	CLSM	confocal laser scanning microscopy
	CoCo	co-condensed
	conc.	concentration/concentrated
	CTAB	hexadecyl-trimethyl-ammonium bromide
D	D	donor
	δ	chemical shift
	DCF	2',7'-dichlorofluorescein
	DFT	density functional theory
	d_{NLDFT}	average pore diameter obtained by NLDFT method
E	*E*	FRET efficiency
	ε	extinction coefficient
	econ.	economic
	ed.	edited
	edn.	edition
	e.g.	for example (Latin: exempli gratia)
	em	emission
	EoY	eosin-5-isothiocyanate
	EtN_3	triethylamine
	EtOH	ethanol
	ex	excitation
F	F	fluorescein/coupled fluorescein isothiocyanate

	F_D	fluoresence intensity of donor in absence of acceptor
	F_{DA}	fluoresence intensity of donor in presence of acceptor
	FITC	fluorescein-5-isothiocyanate
	FITC/RBITC	fluorescein-5-isothiocyanate and rhodamine B isothiocyanate doped
	F/R	fluorescein and rhodamine B doped
	FRET	Förster resonance energy transfer
	FOCS	fibre optical chemical sensor
	FTIR	Fourier transform infrared
	FWHM	full width at half maximum
G	η	viscosity
H	HCl	hydrochloric acid
	HD	high dye loading
	H_2O	distilled water
	HPLC	high-performance liquid chromatography
	Hz	hertz
I	I_0	reference emission (0 ppm NH_3)
	I_{MeNH_2}	emission intensity after $MeNH_2$ exposure
	Ind	indicator
	I_{NH_3}	emission intensity after NH_3 exposure
	IR	infrared
J	J	spectral overlap
K	κ	dipole orientation factor
	k_τ	rate of energy transfer
	KCl	potassium chloride
L	LCST	lower critical solution temperature
	LD	low dye loading
	LED	light emitting diode
M	MAS	magic-angle spinning
	MCM-41	Mobil Composition of Matter No. 41
	$MeNH_2$	methylamine
	$MgCl_2$	magnesium chloride
N	n	refractive index
	N_2	nitrogen
	N_A	Avogadro constant

	NaCl	sodium chloride
	NDIR	non-dispersive infrared
	NLDFT	non localized density functional theory
	NH_3	ammonia
	NIR	near infrared
	NMR	nuclear magnetic resonance
	No.	number
O	ormosil	organically modified silane
P	P123	poly(ethylene glycol)-*block*-poly(propylene glycol)-*block*-poly(ethylene glycol) ($EO_{20}PO_{70}EO_{20}$)
	PG	post-grafting
	pK_a	acid dissociation constant
	pK_b	base dissociation constant
	PMMA	poly(methyl methacrylate)
	p(p).	page(s)
	ppm	parts per million
	PSD	pore size distribution
	PWCS	planar waveguide chemical sensor
Q	Q_0 or Φ	quantum yield
R	R	coupled rhodamine B isothiocyanate
	r	distance between donor and acceptor
	R_0	Förster distance
	RBITC	rhodamine B isothiocyanate
	rel.	relative
	RET	resonance energy transfer
	rpm	revolutions per minute
	RT	room temperature
S	SBA-15	Santa Barbara Amorphous No. 15
	S_{BET}	surface area
	SEM	scanning electron microscopy
	S_{ext}	external surface area
T	τ	lifetime
	t_{90}	time to achieve 90% of the signal
	t_{95}	time to achieve 95% of the signal
	TEOS	tetraethoxysilane

	TMB	1,3,5-trimethylbenzene
	TMOS	tetramethoxysilane
	Tr	sulforhodamine 101 acid chloride (Texas red)
U	UV	ultraviolet
V	V	volt
	VOC	volatile organic compounds
	V_{tot}	total pore volume
W	W	watt
X	χ^2	chi-squared

Chapter 1

Introduction

1.1 Motivation

Ammonia is a toxic flammable colourless compound that is widespread in the biosphere. In addition to biological processes, human activities lead to the production of ammonia from chemical plants and motor vehicles and by the chemical industry for the production of fertilizers, plastics and refrigerating systems.[1] The human ammonia odour threshold is between 5–50 ppm, but eye and respiratory irritation can appear below this value.[1,2] The maximum admissible workplace concentration (MAC) dictated by Suva in 2015 is 20 ppm.[3] In medicine, the ammonia concentration in breath analysis is directly related to organ dysfunction and diabetes.[1,4-6] The development of non-invasive, in-situ and long term monitoring sensor technologies for medicinal applications is nowadays an important issue and enjoys a high degree of attention in research and industry. In view of the toxicity at low concentrations, there is a demand for efficient and easily deployed sensors for ammonia, with detection limit, response time and working temperature depending on the application area as shown in Table 1.[1]

Table 1: Requirements for ammonia gas analysis in different application areas according to reference 1.

Application	Detection Limit	Required response time	Temperature range
Environmental			
• Monitoring ambient conditions	0.1 ppb to 200 ppm	Minutes	0–40 °C
• Measure in stables	1 to 25 ppm	ca. 1 min	10–40 °C
Automotive			
• NH_3 emission from vehicles	4 to 2,000 g/min (concentration unknown)	Seconds	Up to 300 °C
• Passenger cabinet air control	50 ppm	ca. 1 s	0–40 °C
Chemical			
• Leakage alarm	20 to 1,000 ppm	Minutes	Up to 500 °C
Medical			
• Breath analysis	50 to 2,000 ppb	ca. 1 min	20–40 °C

1.2 Chemical Gas Sensors in General

Chemical sensors consist of a recognition element that is sensitive to stimuli generated by various chemical compounds (analytes). The chemical response of this sensing element is transduced into an electric signal. This signal is finally subjected to signal processing after which the analyte concentration is displayed. A large number of chemical gas sensor technologies are available. Principles, applications as well as the pros and cons of the most common gas sensor technologies, that can be used in-situ, are listed in Table 2.

Table 2: Pros and Cons of different sensor technologies[a]

Technology	Pros	Cons
Electrochemical sensors		
Conductometric sensors		
Polymer-Absorption Chemiresistors *Principle*: Analyte gas causes swelling of the polymer due to charge transfer or sorption characteristics that leads to changes in resistance. *Application*: VOCs and simple gases (water vapour, O_2, CO_2, NO_2, NH_3 etc.), used in arrays as "electronic" nose (chip-technology)	• Small and compact devices • Inexpensive • Good sensitivity • Monitoring capability • Real-time measurement	• Moderate response time • Moderate selectivity • Moderate lifetime • Poor reversibility • Susceptible to humidity • Polymer poisoning
Metal-oxide semiconductors *Principle*: The metal-oxide causes the gas either to dissociate into charged species or to oxidize which results in the transfer of electrons that leads to a change in conductivity of the semiconductor. *Application*: Detection of combustible VOCs and simple gases (H_2, CO, O_2, H_2S, NO_2, NH_3 etc.)	• Small and compact devices • Good sensitivity • Real-time measurement • Inexpensive • Long lifetime • Good response time • Monitoring capability	• Susceptible to humidity • Surface poisoning • Moderate selectivity • Commonly a non-linear concentration dependency • Requires a heater • High power consumption

Continue Table 2

Technology	**Pros**	**Cons**
Catalytic bead sensors *Principle*: Oxidation of the gas on the catalytic bead raises the temperature of the device which increases the resistance of a metal coil. *Application*: Detection of combustible VOCs and simple gases (H_2, CO, NO, CH_4 etc.)	• Small and compact devices • Good sensitivity • Real-time measurement • Short response time	• Susceptible to humidity • Catalyst poisoning • Moderate selectivity • Requires a heater
Amperometric sensors		
Electrochemical cells *Principle*: Analyte gas leads to oxidation or reduction at the sensing electrode. The resulting current is a measurement for the gas concentration. *Application*: Detection of numerous anorganic and organic gases such as H_2, O_2, CO_2, SO_2, NO, NO_2, N_2O, chlorine etc.	• Short response time • Good sensitivity • Real-time measurement • Monitoring capability	• Moderate selectivity • Moderate lifetime • Susceptible to humidity and poisoning • Drift compensation • Frequent calibration • Temperature sensitive • Mechanical fragile • Limited miniaturization
Potentiometric sensors		
Field effect transistors *Principle*: Analyte gas is adsorbed at the sensing surface and causes an electrical potential. *Application*: Detection of VOCs and simple gases (H_2, CO, NO, CH_4 etc.)	• Good sensitivity • Good selectivity • Short response time • Monitoring capability	• Still at the development stage • Limited reproducibility • Moderate lifetime • Expensive

Continue Table 2

Technology	Pros	Cons
Mass sensors		
Piezoelectric sensors		
Acoustic wave sensors *Principle*: Analyte gas is adsorbed on a sensing film altering its mass causing a change in the acoustic wave which travels through the membrane. *Application*: Detection of VOCs and simple gases (H_2, CO_2, NO etc.)	• Good sensitivity • Short response time • Small devices • Monitoring capability	• Susceptible towards humidity • Moderate lifetime • Temperature sensitive • Moderate selectivity
Cantilever *Principle*: Analyte gas is adsorbed on a sensing film altering its mass that is detected by the mass-sensitive cantilever due to a change in frequency. *Application*: Detection of VOCs	• Good sensitivity • Monitoring capability	• Still at the development stage • Expensive
Optical sensors		
Direct spectroscopic sensors		
Absorption-based sensors *Principle*: Absorption measurement at the specific IR, Raman or UV wavelength of the analyte gas. *Application*: Detection of VOCs	• Excellent sensitivity • Excellent selectivity if analyte gas has a clearly differentiated absorption • Less or no calibration • Long lifetime • Short response time • Real-time measurement • Monitoring capability • Good reproducibility and reversibility • No electrical or electromagnetic interferences	• Dust can coat the optics • Not all molecules are IR and/or Raman active or absorb in the UV range

Continue Table 2

Technology	**Pros**	**Cons**
Photoionization *Principle*: The analyte gas is ionized by UV light generating a change in voltage at the sensing electrode. *Application*: Detection of VOCs	• Good sensitivity • Real-time measurement • Monitoring capability • Good reproducibility and reversibility	• Expensive light source • Lifetime dependent on light source • Moderate selectivity
Reagent-mediated sensors		
Colorimetric sensing *Principle*: Analyte gas induces a change in colour (change in absorption wavelengths of an indicator) of the sensing film. Often used in arrays. *Application*: Detection of CO_2 and VOCs	• Excellent sensitivity • Good selectivity in arrays • Real-time measurement • No electrical or electromagnetic interferences • Less susceptibility towards humidity	• Moderate response time • Moderate lifetime due to bleaching of the dye
Fluorometric sensing *Principle*: Analyte gas induces a change in fluorescence intensity of the fluorescent sensing film. Often used in arrays. *Application*: Detection of O_2, CO_2, NH_3, water vapour, H_2O_2, NO and H_2S	• Good sensitivity • Long lifetime • Good selectivity • Good response time • No electrical or electromagnetic interferences • Monitoring capability • Real-time measurement • Many platform sensor technologies available • Inexpensive • Less susceptibility towards humidity	• Dust can coat the optics • Temperature sensitive • Lifetime dependent on photobleaching • Has to be calibrated • Limited selectivity

Continue Table 2

Technology	**Pros**	**Cons**
Lifetime sensing *Principle*: Analyte gas leads to a change in fluorescence excited state lifetime of the sensing molecule. *Application*: Detection of O_2, CO_2 and NH_3	• Photobleaching has less impact • Good selectivity • Good sensitivity • Short response time • Long lifetime	• Expensive and complex technology

[a]Electrochemical sensors have been categorized in (1) potentiometric (measurement of voltage), (2) amperometric (measurement of current) and (3) conductometric (measurement of conductivity) sensors. Response times are declared as "short" if the time to achieve 90% of the signal intensity (t_{90}) is typically in the range of a few seconds, "good" if t_{90} ranges typically from a few seconds to 1 minute and "moderate" if t_{90} ranges typically from 1 minute to a few minutes. The lifetime is declared "long" if the life expectancy is over 3 years and "moderate" if it is below three years. "Excellent sensitivity" is given for sensors with detection limits in the sub-ppm range, "good" for detection limits in the low ppm range. The data were assembled from references 1 and 7-27. VOC is the abbreviation for organic volatile compounds.

Desired properties of a chemical gas sensor include high sensitivity, high selectivity and high stability – the three important "S" in the sensor technology. Other important requirements are reversibility and the speed of response. However, from Table 2 it appears that not every requirement can be met by one single sensor technology. For chemical sensors, high sensitivity and perfect reversibility impose contradictory constraints: sensitivity requires strong interaction with the sensor whereas reversibility requires a weak interaction.[7] Selectivity is more difficult to achieve by sensors based on combustion of the analyte gas since the combustion process results in a thermal signature depending on the type and concentration of the gas. Overlapping thermal signatures and the resulting equal change in conductivity or resistance of the sensor from different gases make the gas discrimination challenging. Generally, the sensors are fairly selective to the target gas they are designed for and have been accordingly calibrated and compensated. Sensor arrays relying on different transducer and sensitive material types have been investigated aiming the development of "electronic noses" which are able to selectively discriminate various gases and their particular concentrations. Hierarchical cluster analysis is applied to distinguish between the different components.[7,17] Calibrations due to poisoning or non-linearity and/or drift compensations due to thermal or

humidity fluctuations are required for almost all sensor technologies. However, the time intervals can be significantly different, not only among the different sensor technologies but also within a certain technology because of varying sensing chemistry. The speed of response is dependent on the sensing chemistry but also on physical factors such as the time needed to transport the gas to the sensing surface and diffusion of the gas into the sensor coating. A clear advantage of optical sensors over electrochemical sensor technologies is that they do not suffer from electrical or electromagnetic interferences.[14] In addition, the electronics for readout and signal processing can be separated and independent from the analyte sensing platform. In this way, the electronic is insulated from ageing processes triggered by the analyte (or other components of the gas mixture) and only the sensor platform has to be calibrated or replaced. Furthermore, the analogue to digitial conversion can be done earlier, which facilitates the signal transporting.

Generally, it is obvious that it is necessary to compromise. Regarding these various sensor technologies, a tailored sensor solution has to be elaborated for the required sensor operation. Therefore, advantages and disadvantages of a certain sensor technology (and sensing chemistry) have to be weighed up for the specific field of application and environment of the projected sensor.

1.3 Ammonia Gas Sensors

A large number of ammonia gas sensors have been reported, demonstrating the continuing demand for efficient detection systems. A range of methods is available for monitoring gaseous ammonia, based on electrochemical cells, semiconducting metal-oxides, conducting polymer and optical detection techniques.[1,7-9,26,27] The ammonia detection techniques have been classified into *electrochemical* and *optical* sensors which are discussed in detail below.

1.3.1 Electrochemical ammonia gas sensors

Electrochemical ammonia gas sensors usually depend on an oxidation reaction where ammonia is converted into electro-inactive ammonium, nitrogen and hydrogen protons at the sensing electrode.[24,25] They are compact, require little power and exhibit good linearity and repeatability.[25] However, they have a temperature dependent calibration graph, the opportunity of electrolyte

poisoning and, as a consequence, suffer on temporal degradation that limits the sensor performance significantly.[9,25] Semiconducting metal-oxide based sensors work on the basis of chemosorption of ammonia usually on a heated metal-oxide surface where the ammonia is oxidized. The oxidation process leads either to a change in temperature or removes oxygen from the metal-oxide grains surface.[1,28-33] Both processes lead to a change in conductivity that can be detected. Sensors based on the metal-oxide semiconducting technology can be produced at low prices and are quite sensitive, but suffer from non-linearity, drifting due to ageing processes, low selectivity and cross-sensitivity to humidity.[1,9,25] Another measurement principle makes use of conducting polymers where ammonia can reversibly reduce the oxidized form of the polymer that leads to a change in conductivity of the material.[1,34-37] The major drawback of polymer based sensors is the low reversibility and longer response time.[1,10,38,39]

1.3.2 Optical ammonia gas sensors

Reagent-mediated optical ammonia gas sensors

All the electrochemical sensor principles described above transform ammonia into another chemical species. For closed systems with a limited volume and a low concentration, this can result in an underestimating of the real value. Optical sensors offer better possibilities for direct sensing of the target gas meaning that the gas does not need to be transformed into another species for the detection procedure. The focus of this work will be on optical chemical sensors, which have found numerous applications in areas such as the chemical industry, in biotechnology and medicine. Most optical sensors for gaseous as well as dissolved ammonia are based on optical absorption[40-50] and luminescence.[51-59] Ammonia sensors based on other optical parameters, such as refractive index[60-62] and reflectance,[63-66] have also been developed. In the case of colorimetric absorption and luminescent ammonia detection, the measurement principle relies on the change of absorbance or luminescence of a pH-indicator (Ind) which is deprotonated in the presence of ammonia:

$$NH_3 + IndH \rightleftharpoons NH_4^+ + Ind^-$$

The indicators usually are immobilized in a transparent polymer or sol-gel film which is deposited on a fibre or planar substrate. These changes in absorbance and luminescence wavelengths or intensities can be measured by spectroscopic methods or optoelectronic devices. A disadvantage of luminescence intensity detection is the susceptibility to signal fluctuations due to changes in excitation source intensity and photobleaching of the luminescent pH-indicator dye.[8] However, the limitations for reagent mediated optical sensors such as photobleaching and temperature dependency can be addressed through the appropriate choice of the indicator dye, the sensing mechanism and an adequate referenced detection method.[14] The more recent lifetime-based ammonia sensing[67-70] is less dependent on the indicator dye concentration so that photobleaching has less impact on the sensor performance. However, lifetime sensing systems require still more complex and expensive electronics, which make them less attractive for mass production.[8] Reflectance based ammonia sensors differs from the photometric sensors only by the fact that the light reflection by the reagent phase is measured instead of the light transmission.[9] Electrostatic interactions, the formation of hydrogen bonds or the deprotonation of an incorporated dye can lead to a change in the refractive index of the sensing film which results in a change in the reflected light angles from the waveguide-film interface.[60-66]

Direct optical ammonia gas sensing

Another optical sensor technology is available for ammonia gas sensing such as direct absorption-based sensing by infrared spectroscopy. Infrared (IR) spectroscopy has been widely used for the detection of gases. In this technique the gas is confined in an optical absorption cell where the specific IR wavelengths are measured, which are characteristic of the vibrational modes of the molecule. Ammonia exhibits medium IR absorption bands around 10 µm (symmetric bending mode) and weak absorption bands around 6 (N-H bond stretching and bending) and 3 µm (N-H bond stretching and contraction) as illustrated in Figure 1.[18,71,72] The system components usually are an IR source, optical filters to select the specific absorption wavelengths and a detector, that is sensitive at the wavelength of interest.[8] Non-dispersive infrared sensors (NDIR) make use of band-pass filters in order to choose the specific analyte absorption wavelength in contrast to the light dispersion by a prism or a grating in a normal

spectrometer.[8] Fourier transform infrared spectroscopy (FTIR) generates an interferogram from the IR emission of the sample which is then Fourier transformed to obtain the spectrum. The ability of FTIR spectroscopy to measure multiple analytes simultaneously differentiates this technique from NDIR sensors. Diode lasers and novel quantum cascade lasers (QCL) have led to the development of highly sensitive and selective sensor systems. Diode lasers cover the wavelengths ranging from 1 to > 2 µm whereas QCLs span wavelengths from 2 to > 4 µm.[8] Laser spectroscopy is the choice for trace gas analysis because of its higher sensitivity and selectivity, which arises when a spectrally narrow laser source probes a narrow and analyte specific absorption feature.[8] Cheaper and smaller IR sources are IR LEDs and black body emitters. Both have broader emission bands than QCLs and diode lasers which can affect the selectivity if other gases absorb in this wavelength range covered by the LED. However, this problem can often be solved by the choice of appropriate optical filters. Ammonia can be clearly distinguished from other common gases since the molecule has absorption bands at wavelengths where the other gases do not absorb (Figure 1). Since few NH_3 vibration modes are Raman active, Raman spectroscopy is another direct spectroscopic method to detect ammonia.[8,73]

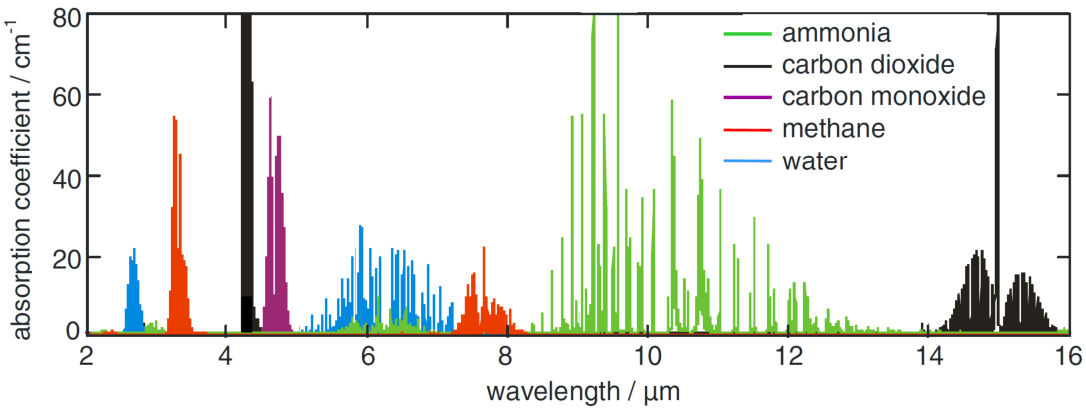

Figure 1: Absorption spectra of NH_3, CO, CO_2, CH_4 and H_2O in the mid IR spectrum taken from reference 18.

1.4 Sol-Gels in Optical Sensing

The sol-gel process is a convenient method to synthesize xerogel glass films or aerogels from silicon alkoxide precursors. In a first step, the precursors,

commonly tetraethoxysilane (TEOS) and organic modified silanes (ormosil) such as tetramethoxysilane (TMOS) are dispersed in methanol or ethanol forming a sol. Upon addition of water and a base or an acid, the silicon alkoxide precursors ($Si(OR)_4$) are hydrolyzed (a) and finally condensed to form siloxane bridges (b and c).[74-77] At this stage, the solvent can be evaporated at room or elevated temperature, or the sol is first allowed to condense forming a gel as shown in Figure 2. Solvent evaporation typically causes shrinkage since the solvent leaves the micropores of the silica network.[74-77] Evaporation of the solvent at the sol stage lead to more compact films whereas the evaporation at the gel stage can lead to more porous ceramics since the previous gelation has formed a silica network.[74-77] Alternatively, removal of the solvent by supercritical drying of the gel leads to a material which is similar in the size and shape of the original gel (Figure 2). The resulting aerogel has low solid volume fractions near 1% and thus very high pore volumes.[77]

(a) Hydrolysis: $Si(OR)_4 + xH_2O \longrightarrow HO_x\text{-}Si(OR)_{4-x} + xROH$

(b) Condensation: $(RO)_3Si\text{-}OH + HO\text{-}Si(OR)_3 \longrightarrow (RO)_3Si\text{-}O\text{-}Si(OR)_3 + H_2O$

(c) And/or $(RO)_3Si\text{-}OR + HO\text{-}Si(OR)_3 \longrightarrow (RO)_3Si\text{-}O\text{-}Si(OR)_3 + ROH$

Process parameters such as pH, ratio of water to silicon alkoxide precursor, drying conditions and solvent contribute to the properties of the resultant silica films.[74-80]

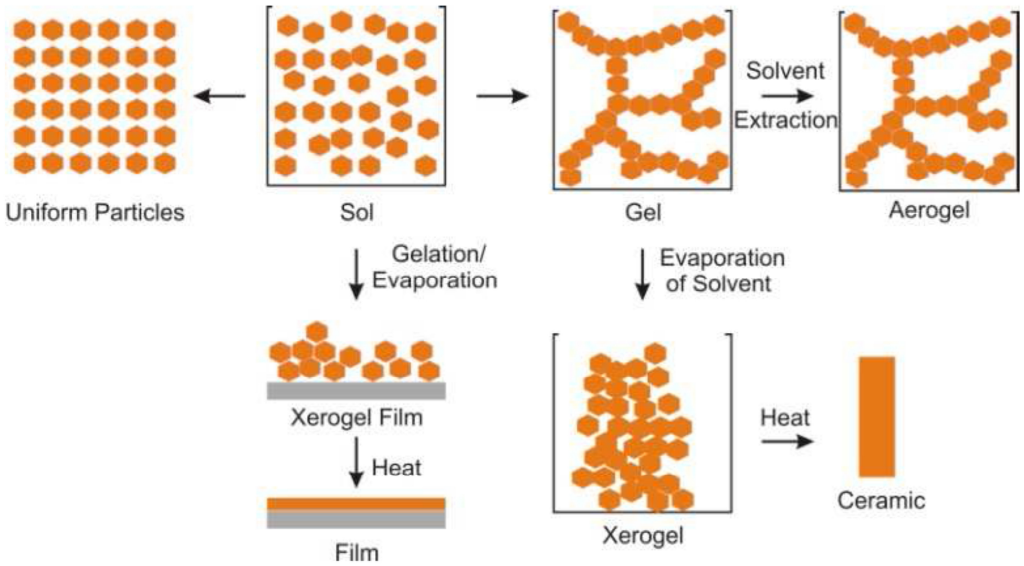

Figure 2: Overview of the sol-gel process illustrating the differences between xerogels and aerogels taken from reference 77.

Sol-gel materials offer several advantages for the fluorescence optical gas sensing application including optical transparency from the ultraviolet to infrared wavelengths, process versatility that facilitates tailoring of the film properties (e.g. porosity, refractive index, polarity, elasticity etc.) as well as chemical and thermal stability.[8,16,81-88] Another benefit of the sol-gel process is the possibility of simple chemical doping of the material by adding the desired dye molecules to the precursor sol solution. Upon polymerization of the precursors, the dyes are immobilized into the silica matrix. Ormosil based sol-gels offer several advantages for optical gas sensing compared to purely inorganic sol-gels. The enhanced hydrophobicity[89-91] improves the sensitivity of the sensor[89,92-96] and reduces the cross-sensitivity of the gas sensor towards water vapour, as the latter species is repelled by the hydrophobic matrix. Furthermore, the more rigid networks (due to the lower degree of cross-linking) of ormosil xerogels are reported to positively impact the photodegradation of the dye molecules resulting in less photobleaching of the dyes.[97,98] Regarding these advantages of the sol-gel technology it is not surprising that a number of ammonia sensors based on dye-doped sol-gel matrices have been developed.[40-42,46,48,49,52,53,55-58] The kind and content of ormosil precursors have been found to significantly affect the response to ammonia because of varying ammonia permeability and xerogel polarity.[55,89,96,99]

1.5 Mesoporous Silica in Optical Sensing

The mesoporous materials used in this project were Santa Barbara Amorphous number 15 (SBA-15) and Mobil Composition of Matter number 41 (MCM-41). The synthesis of mesoporous silica requires cationic alkylammonium surfactants such as CTAB (hexadecyl-trimethyl-ammonium bromide) or Pluronic 123 in amounts above their critical micelle concentrations. They cooperatively assemble with the inorganic precursors (e.g. TEOS) to form the silica matrix. The surfactants can be removed by calcination or Soxhlet extraction.[77,100] The resulting materials exhibit narrow pore size distribution and highly ordered mesostructures. Both, MCM-41 and SBA-15, have a two-dimensional hexagonal alignment of mesoporous channels whereas SBA-15 often features micropores that can lead to interconnect pore channels.[77,100] The materials can be functionalized with organic functional groups by either (1.) the post-grafting method, (2.) the direct co-condensation or a method (3.) that leads to periodic

mesoporous organosilicas as illustrated in Figure 3.[100,101] The preparation of periodic mesoporous silicas leads to homogenously distributed organic units incorporated into the three-dimensional network structure of the silica matrix. These materials exhibit high thermal stability but usually have completely disordered pore systems and broad pore size distributions.[100] They are promising for technical applications such as for catalysis, adsorption, chromatography and for active release systems. However, for gas sensor applications it is important that the matrix material provides accessibility to the incorporated analyte sensing organic groups. The accessibility in periodically mesoporous silica is limited since the groups are integral parts of the pore walls.[100] Additionally, the synthesis of bisylated organic materials with a free functional group for analyte sensing is complicated. As a consequence, this material is less attractive for sensor applications and the focus is on functionalized materials obtained by the co-condensation or post-grafting approach.

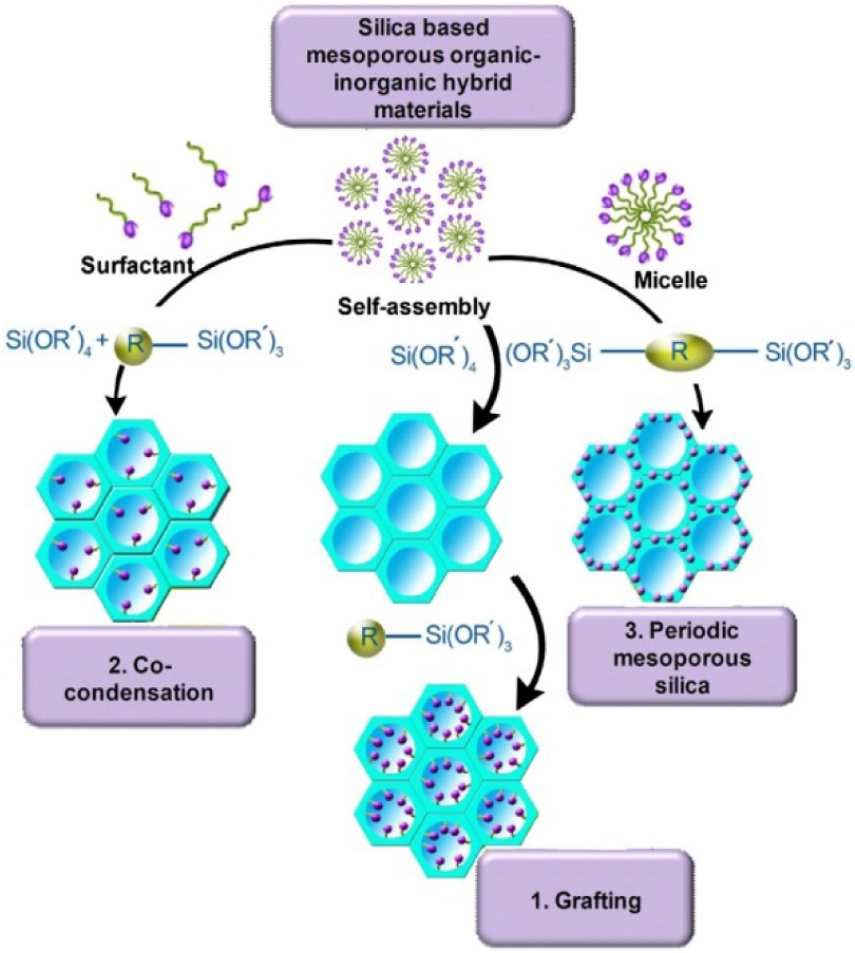

Figure 3: Different methods for the synthesis of organic-inorganic hybrid mesoporous silica: 1. grafting, 2. co-condensation or in situ grafting and 3. periodic mesoporous silica. This scheme is taken from reference 100.

Post-synthetic functionalization is favored over co-condensation if the groups to be integrated are not sufficiently stable under the harsh conditions of mesoporous silica synthesis, or if more regular silicates with a narrower pore size distribution (PSD) are desired.[100] One drawback of grafting is that the entire surface may not be accessible, which then leads to an inhomogeneous distribution with more grafted groups on the external surface and near the pore entrances.[100,102-104] The solvent in which the post-synthetic functionalization is performed, as well as the type of organosilane used, contributes to the final functional group distribution on the mesoporous material.[104-106] A preferential coupling to the pore openings during the initial stage of the grafting procedure prevents the diffusion of further organosilanes into the centre of the pores and can lead to a lower degree of functionalization.[100,105] In contrast, co-condensation does not have the issue of inhomogeneous functional group distribution. Since organic groups are introduced during the synthesis of the material they tend to be distributed evenly throughout the entire framework. Moreover, pore blocking is not a problem, since the organic functionalities are integral components of the silica matrix.[100] However, the organic moiety to be incorporated must withstand the synthesis conditions and high concentrations of organic groups can have negative effects on the formation of the material (mesoscopic order, PSD, particle shape and size).[100,102,103,107-109]

The possibility of organic functionalization of mesoporous silica by the co-condensation and post-grafting method allows this versatile material to be used in many applications, in particular the separation and adsorption of gaseous species. Recently, the potential of mesoporous silica in the field of luminescence sensing has been demonstrated.[77,110-128] The sensing properties of the materials were achieved by functionalizing the silica with dyes or metal complexes, whereas dyes have been primarily immobilized to detect pH,[124-126] hydrogen or metal ions[114-116,121-123] and metal complexes to sense oxygen.[110-113,120] Optical ammonia sensing of these materials is achieved by functionalizing the silica with a pH-indicator dye that changes absorption with increasing ammonia concentration.[129-131] For an optical sensing application, dye modified silica particles can be easily immobilized into sol-gel matrices.[77,132,133] Beside the functionalization versatility, the high surface area and controlled pore size are beneficial for sensing applications making these materials promising for sensor developments.[77]

1.6 Dyes and Fluorescence

Luminescence is the emission of light from any substance and includes both fluorescence and phosphorescence, depending on the nature of the excited state.[134] The molecular processes that occur between absorption and emission of light are usually explained by means of a Jablonsky diagram which is shown in Figure 4. Upon excitation of the fluorophore, an electron from the ground state (S_0) is raised to a higher energy level excited state (S_1). By a process called internal conversion that is non-radiative and happens within 10^{-12} s,[134] the molecule relaxes to the lowest vibrational level of S_1. In the excited singlet state the electron in the excited-state orbital is paired by opposite spin to the second electron in the ground-state orbital. The return to the ground state is spin allowed and thus happens rapidly by emission of a photon.[134] The emission rates of fluorescence are typically 10^8 s^{-1}, so that a typical fluorescence lifetime is near 10 ns.[134]

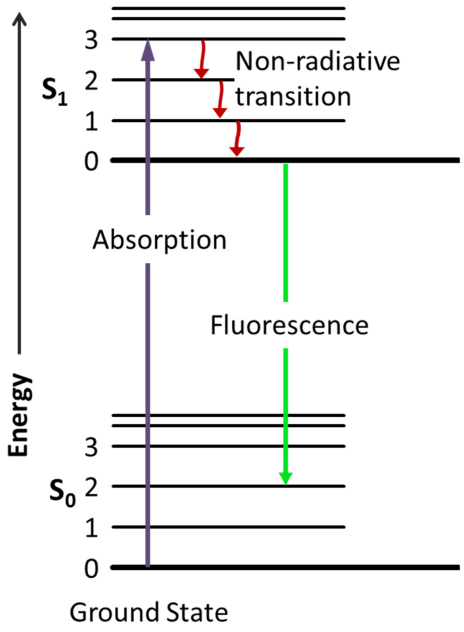

Figure 4: One form of a Jablonsky diagram taken from reference 135.

Fluorescence typically occurs from aromatic molecules. Widely used fluorophores are xanthene dyes like fluorescein and rhodamine. The emission spectra are dependent on the chemical structure of the fluorophore and the chemical environment in which it is dissolved or immobilized.[134] By looking at the Jablonsky diagram in more detail one can see that the energy of the emission

is less than that of absorption. Consequently, the fluorescence emission band is shifted to longer wavelengths in comparison to the absorption band. The difference in the band maxima positions of absorption and emission spectra is known as Stokes shift.[134] Regarding the optical sensing application, large Stokes shifts are advantageous since excitation and emission wavelengths can be fully separated which allows the detection of only the emission intensity without interference with the excitation source intensity.

Other specific characteristics of a fluorophore are lifetime and quantum yield. Quantum yield is the number of emitted photons relative to the number of absorbed photons.[134] Molecules like rhodamines have large quantum yields and thus display bright emissions.[134] The fluorescence lifetime refers to the average time the fluorophore stays in its excited state before emitting a photon. It determines the time available for the molecule to interact with its environment and hence the information to read out from its emission.[134]

1.7 FRET in Molecular Systems

Resonance energy transfer (RET) can occur in the excited state of a fluorophore. This process takes place if the emission spectrum of a fluorophore, called the donor, overlaps with the absorption spectra of another molecule, called the acceptor. The acceptor does not need to be fluorescent. In RET, the donor and acceptor are coupled by a dipole-dipole interaction and hence is not the result of donor emission being absorbed by the acceptor.[136,137] Therefore, the process does not involve the appearance of an intermediate photon (Figure 5). For this reason, to avoid misinterpretation, the term RET is preferred over the term fluorescence resonance energy transfer.[137] The extent of energy transfer is dependent on different parameters such as the distance between donor and acceptor, the extent of spectral overlap and on the relative orientation of the donor emission dipole moment as well as on the acceptor absorption dipole moment.[137,138]

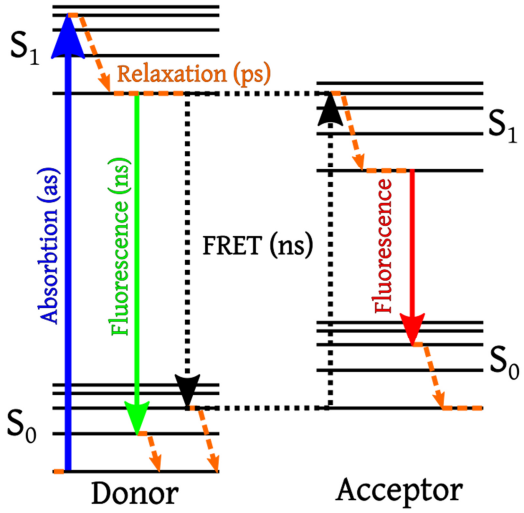

Figure 5: Jablonski diagram of FRET with typical timescales taken from reference 139.

The rate of energy transfer $k_\tau(r)$ is given by:[137]

$$k_\tau(r) = \frac{1}{\tau_D}\left(\frac{R_0}{r}\right)^6 \quad (1)$$

Where r is the distance of the donor and acceptor and τ_D is the lifetime of the donor in the absence of energy transfer. R_0 is the Förster distance where the resonance energy transfer efficiency is 50%. The efficiency E of the energy transfer is given by:[137]

$$E = \frac{R_0^6}{R_0^6 + r^6} \quad (2)$$

The energy transfer efficiency can be experimentally calculated by measuring the relative fluorescence intensity of the donor (D), in the absence (F_D) and presence (F_{DA}) of the acceptor (A): [137]

$$E = 1 - \frac{F_{DA}}{F_D} \quad (3)$$

The transfer efficiency can also be calculated from the lifetimes (τ_D and τ_{DA} respectively):[137]

$$E = 1 - \frac{\tau_{DA}}{\tau_D} \quad (4)$$

The Förster distance R_0 is expressed by:[138]

$$R_0^6 = \frac{9000 Q_0 (ln10) \kappa^2 J}{128 \pi^5 n^4 N_A} \quad (5)$$

Q_0 describes the fluorescence quantum yield of the donor in absence of the acceptor and n is the refractive index of the solvent or matrix material. The dipole orientation factor κ is 2/3 if a random rotational distribution of the dyes is assumed. J designates the spectral overlap.

Equations 1–5 can be applied for the calculation of the RET parameters if the donor-acceptor pairs are separated by a fixed distance.[137] Furthermore, the amount of donor and acceptor labelling in the sample should be complete and in the same amount, otherwise, the extent of fractional labelling of the acceptor has to be considered.[137]

1.8 Fluorescence based Optical Chemical Sensors

Compared to colorimetric absorption-based optical sensors, optical sensors based on fluorescence have a larger number of experimental parameters (absorption and emission wavelength, lifetime, quantum yield, energy transfer, etc.) available for manipulation compared to the absorption measurements which is beneficial for the achievement of good sensitivities and selectivities.[140] For the fluorescent optical chemical sensing of gases, pH and ions, fluorescent indicator dyes have been incorporated into various matrices such as organic polymers, sol-gels, xerogels, hydrogels and particles.[16,140,141] Fluorescent optical ammonia sensing is achieved by immobilizing fluorescent pH-sensitive dyes such as fluorescein and fluorescein derivatives (aminofluorescein, dichlorofluorescein, fluorescein isothiocyanate and eosin) into various polymers such as acrylic esters, celluloses and ormosil sol-gels.[51,53-55] The change in fluorescence intensity due to ammonia exposure can be measured by direct fluorescence spectroscopy or light sensitive optoelectronic devices like phototransistors or photodiodes. Large Stokes shifts are beneficial for the detection of emission wavelengths and are obtained by an appropriate choice of dyes or by implementing a RET dye pair. The principles and applications of RET sensors have been divided in *emission intensity*, *lifetime* and *ratiometric* measurement and are described in the following subchapters.

1.8.1 Emission intensity measurement

Fluorescent ammonia sensors based on the resonance energy transfer have been reported.[53,66,68] Changes in the energy transfer occur due to ammonia dependent changes in the absorption spectrum of an ammonia sensitive dye leading to an altered spectral overlap between donor emission and acceptor absorption. A significant advantage of RET-based sensing is that it can simplify the design of the sensor since donor and acceptor can be separate molecules. In this way, not only one molecule has to fulfil all desired sensing properties at one time: One molecule can be sensitive to ammonia and the other molecule can exhibit the desired fluorescence spectral properties.[142] If both dyes involved are fluorescent, an irrelevant emission band can be filtered off by suitable optical filters.[53,66] In such systems the sensor benefits from a large shift between excitation and emission wavelength.

1.8.2 Lifetime measurement

As indicated earlier, the disadvantage of fluorescence intensity detection is the susceptibility to signal fluctuations due to changes in excitation source intensity and photobleaching of the luminescent pH-indicator dye.[8] Lifetime measurements have been implemented to overcome this problem. Since the excited state has a lifetime, the fluorescence occurs delayed with respect to the excitation signal and the lifetime can be determined from the time dependent phase shift. The recent dual life time referencing method makes use of simultaneous excitation of the fluorescent indicator and a luminescent reference dye measuring the overall phase shift.[66,68] For successful lifetime referencing sensing, following criteria have to be fulfilled: (a) the reference dye and the indicator dye exhibit large different decay times whereas the reference dye should have a long decay time for an accurate measurement, (b) the reference dye shows no-sensitivity towards ammonia or other substances that can be involved, (c) the fluorescent indicator changes its emission intensity as a function of the analyte concentration and (d) the reference dye has equal excitation and emission wavelengths as the sensing chemistry.[66,68] The change in the phase angle obtained from the lifetime measurements upon excitation of reference luminophore and indicator fluorophore results from the changes in the ratio of their emission intensities in the sensing system due to the presence of

the analyte molecules.[66,68] This principle can be applied for a single fluorescent ammonia sensitive dye but also for RET systems.

1.8.3 Ratiometric measurement

Another referencing method is based on the ratiometric measurement of two different intensities recorded at two different bands of wavelengths.[68] For this method, donor and acceptor in the RET system have to be fluorescent and one of them is sensitive to ammonia by changing its absorption spectrum. An altered absorption of a RET-partner due to ammonia leads to a different spectral overlap of donor emission and acceptor absorption band leading to a change in energy transfer efficiency. Both emission bands are affected from this process. The intensities of the two emission bands can be continuously compared by ratiometric fluorescence measurements. There is also the possibility to interconnect a non-fluorescent pH-indicator dye where the protonated form overlaps with the donor emission and the deprotonated form overlaps with the acceptor emission as shown in Figure 6.[68] With increasing ammonia concentration the donor emission intensity increases due to less spectral overlapping with deprotonated indicator molecules whereas the acceptor emission intensity decreases due to an enhanced spectral overlap. A ratiometric referencing approach also offers the possibility for fluorescence imaging methods.[68]

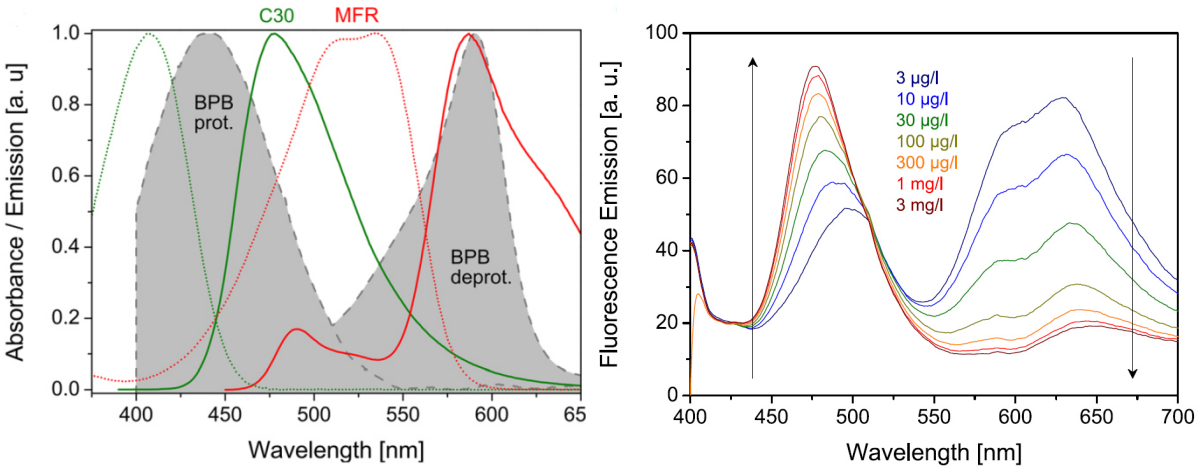

Figure 6: Left: shows the two wavelength referencing system reported in reference 68: absorbance (dotted line) and emission (solid line) spectra of the donor Coumarin 30 (green), acceptor Macrolex Fluorescent Red as well as the absorbance spectra for the protonated and deprotonated forms of pH-indicator bromophenol blue (BPB, grey areas). Right: fluorescence emission spectra of the RET system at different ammonia concentrations.

1.9 Optical Sensor Platforms for Fluorescence Sensing

Planar and fibre optic waveguides have been intensively discussed for the application as sensor platforms in optical sensors since they provide the opportunity to combine the light delivery by multiple internal reflection and light collection with intrinsic sensing functionality. Therefore, both sensor platforms are well suited for fluorescence sensors providing the interaction between the evanescent light and the dye molecules.[8,18,26] Traditional and well-investigated organic polymer film coating techniques such as plate-spreading, dip- and spin-coating can be easily adapted for the deposition of thin sol-gel films on the desired fibre or planar substrate.[81] In the following subchapters *fibre optic* and *planar waveguide* sensor platforms are described separately in more details.

1.9.1 Optical fibre waveguide sensor platforms

The chemical as well as optical principles in optical gas sensing have not changed substantially over the years, but many new ideas came up regarding the sensor platforms.[8,9] A number of fibre optical chemical sensors (FOCS) have been reported and the most of these sensors can be categorized in configurations illustrated in Figure 7: Tip based, bifurcated, declad as well as unmodified fibres. Further configurations such as U-bend fibres and fibre bundles have also been reported. Optical sensors can be divided in two subgroups: active and passive. Active and passive configurations are explained by means of fibre-optic sensors in the following.

Passive FOCS

The fibre is passive if the sensor response is not connected to an intrinsic change in the optical properties of the fibre.[8] Therefore, the fibre only transports the optical signal to and from the sensing environment. Passive FOCS are commonly used to develop fibre-coupled spectrometers.[8] For the implementation of colorimetric, absorption and fluorescence-based passive FOCS the reflectance-based configuration is of great interest. The analyte sensitive material is typically deposited on a planar support and a fibre bundle can be used to deliver the light (e.g. excitation source) to this material and collect the reflected light. The light normally is delivered via the central fibre in the bundle and the reflected light is collected by the outer fibres.[8] For

fluorescence detection, bifurcated fibres have been used extensively to deliver excitation light with one fibre and collect the fluorescence with the second.[8]

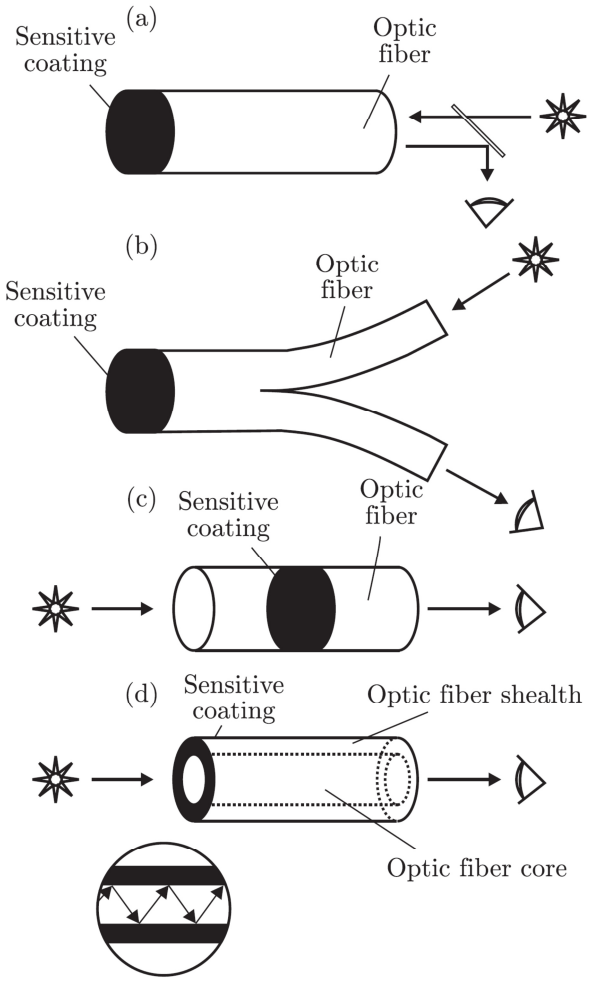

Figure 7: Optical fibre waveguide sensors configurations: the sensitive coating can be placed on the tip of the fibre (a, b and c) or on the side (d) by removal of the cladding. This figure is taken from reference 9.

Active FOCS

Active FOCS consist of fibres that have been modified so that intrinsic analyte sensitivity is achieved. In this way, the optical properties of the fibre are changed by the presence of the analyte. Such fibres can be produced by replacing the cladding of the fibre with an analyte sensitive layer that contains the fluorescent indicator dyes. The dyes immobilized into the new functionalized fibre cladding material are excited by the evanescent field of the fibre. An electromagnetic wave that is guided through a dielectric fibre decays exponentially away from the core cladding boundary.[8] The evanescent tail is an integral part of the guided wave and its characteristics are determined by the

guiding parameters of the wave. Therefore modification of the evanescent field by analyte sensitive molecules modifies the guided wave without touching the core of the waveguide.[143] The degree of evanescent-wave interaction is dependent on the refractive index of the cladding material.[143] Another possibility to produces active FOCS is to dope the fibre with fluorescent materials during the fibre fabrication process. However, this approach can have an adverse effect on the guiding properties of the fibre.

1.9.2 Planar waveguide sensor platforms

Planar waveguide chemical sensors (PWCS) are a relatively recent innovation in the field of optical chemical sensors. As for the fibre-optic sensors, their operation principle is based on internal reflection of light and the interaction of a sensitive layer with the evanescent field. Typical configurations of plane waveguide optical chemical sensors are shown in Figure 8.[9] In the case of two-layer plane waveguides one layer is the sensitive layer, which is deposited on the other layer which represents the optic carrier and waveguide. The three-layer structure is reported to be more effective. In this configuration, the waveguide layer is located on the surface of an optic base and the sensing layer is deposited on the former.

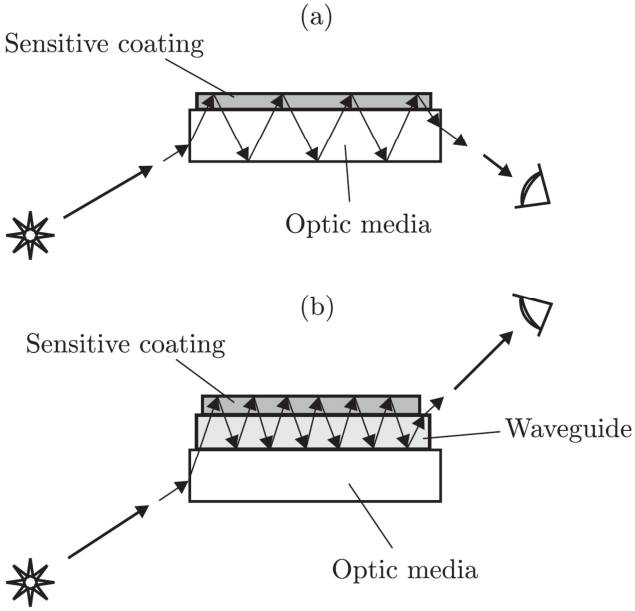

Figure 8: Basic designs of planar waveguide sensors: the sensitive coating can be directly deposited on the optic carrier that acts as the waveguide by internal reflection of the light (a). An example of a three layer structure where the waveguide is deposited between optic media and sensitive coating (b). This figure is taken from reference 9.

An advantage of PWCS over FOCS is the compatibility of the planar geometry with a range of miniaturization technologies such as lab-on-a-chip systems. Thus, they offer the possibility for new designs and integration of multiple functionalities into a single sensor chip.[8]

1.10 About the Project

The aim of this project was to engineer a fluorescence-based optical sensor for the detection of gaseous ammonia. The focus of the group "medical textiles" is on functionalizing textiles which suggests that a polymer optical fibre based sensing platform was aimed. Optical fibres resemble textile fibres and can be integrated into clothing by common manufacturing processes. In this way, the desired functionality can be easily included into a fabric. Wearable real-time sensors are comfortable and would facilitate working in a contaminated area.

The idea was to coat a declad or naked fibre with an ammonia sensitive cladding as illustrated in Figure 9. The exposure to ammonia leads to a change in fluorescence intensity or a shift in fluorescence wavelength of the cladding which affects the evanescent field and guided wave in the optical fibre. The change in the guided fluorescence (light) intensity can be detected by light sensitive detectors such as photodiodes or phototransistors at the end of the fibre. A polymer optical fibre (POF) made of poly(methyl methacrylate) (PMMA) was favoured over an optical glass fibre because the latter is mechanically less claimable and therefore less suited to be incorporated into textiles. Since a POF is a flexible substrate, flexibility is also desired for the sensitive cladding.

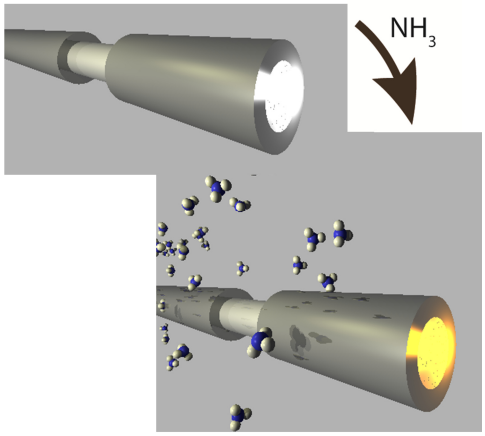

Figure 9: A polymer optical fibre with an NH_3 sensitive cladding before (top) and after NH_3 exposure (bottom). The exposure to NH_3 leads to a change in fluorescence intensity or a shift in fluorescence wavelengths of the cladding which affects the evanescent field and guided wave of the optical fibre.

The sol-gel approach offers excellent possibilities for the development of a tailored cladding that resists mechanical stresses on the one hand and tolerates the exposure to ammonia which is a corrosive gas on the other hand. A master student made valuable prestudies and demonstrated the proof of concept of a fluorescent based ammonia sensor using sol-gel as the matrix substance. These first, more superficial evaluations on the sol-gel precursors, drying process, transparency, dyes, ammonia response and fibre adhesion of the resulting films accelerated and facilitated the choice of dyes and ormosil precursors used in this project. In prospect of a referenced and flexible sensor system, a RET-based sensor system was aspired. The large Stokes shifts provided by the RET mechanism and the use of dyes with excitation wavelengths in the visible range allow the insertion of inexpensive light emitting diodes (LED) and detectors. The first sensor prototype developed in this project is based on a planar waveguide PMMA substrate with an ammonia sensitive coating on the top. The planar substrate has the advantage of a simpler handling in respect of the coating procedure, storage and spectrophotometric measurements. Optimizations were performed on this sensor platform and the findings were transferred on a fibre-optic waveguide sensor prototype.

1.11 References

1 B. Timmer, W. Olthuis and A. v. d. Berg, *Sens. Actuators*, *B*, 2005, **107**, 666-677.

2 R. A. Michaels, *Environ. Health Persp.*, 1999, **107**, 617-627.

3 Suva, Bereich Arbeitsmedizin, *Grenzwerte am Arbeitsplatz 2015*, Luzern, 2015.

4 S. W. M. O. Damink, N. E. P. Deutz, C. H. C. Dejong, P. B. Soeter and R. Jalan, *Neurochem. Int.*, 2002, **41**, 177-188.

5 B. I. Cohen, *Med. Hyphotheses*, 2002, **59**, 757-758.

6 T. Hibbard and A. J. Killard, *Crit. Rev. Anal. Chem.*, 2011, **41**, 21-35.

7 A. Hierlemann, *Chem. Rev.*, 2008, **108**, 563-613.

8 C. McDonagh, C. S. Burke and B. D. MacCraith, *Chem. Rev.*, 2008, **108**, 400-422.

9 S. G. Sazhin, E. I. Soborover and S. V. Tokarev, *Russ. J. Nondestruct.*, 2003, **10**, 791-806.

10 B. Adhikari and S. Majumdar, *Prog. Polym. Sci.*, 2004, **29**, 699-766.

11 L. Xiong and R. G. Compton, *Int. J. Electrochem. Sci.*, 2014, **9**, 7152-7181.
12 C. K. Ho, M. T. Itamura, M. Kelley and R. C. Hughes, *Review of Chemical Sensors for In-Situ Monitoring of Volatile Contaminants*, Sandia Report SAND2001-0643, New Mexico, 2001.
13 http://www.siemens.com/innovation/de/publikationen/zeitschriften_pictures_of_the_future/pof_herbst_2004/sensortechnik/gassensoren.htm, accessed March 2015.
14 D. Wencel, T. Abel and C. McDonagh, *Anal. Chem.*, 2014, **86**, 15-29.
15 D. M. Wilson, S. Hoyt, J. Janata, K. Booksh and L. Obando, *IEEE Sens. J.*, 2001, **1**, 256-274
16 N. V. Kostesha, T. S. Alstrøm, C. Johnsen, K. A. Nielsen, J. O. Jeppesen, J. Larsen, M. H. Jakobsen and A. Boisen, Proceedings of SPIE on Advanced Environmental, Chemical, and Biological Sensing Technologies VII, 2010.
17 J. R. Askim, M. Mahmoudi and S. Suslick, *Chem Soc. Rev.*, 2013, **42**, 8649-8682.
18 J. Hodgkinson and R. P. Tatam, *Meas. Sci. Technol.*, 2013, **24**, 1-59.
19 http://www.intlsensor.com/pdf/catalyticbead.pdf, accessed April 2015.
20 http://www.intlsensor.com/pdf/photoionization.pdf, accessed April 2015.
21 http://www.intlsensor.com/pdf/infrared.pdf, accessed April 2015.
22 http://www.intlsensor.com/pdf/solidstate.pdf, accessed April 2015.
23 http://www.intlsensor.com/pdf/electrochemical.pdf, accessed April 2015.
24 X. Ji, C. E. Banks, D. S. Silvester, L. Aldous, C. Hardacre and R. G. Compton, *Electroanal.*, 2007, **21**, 2194-2201.
25 R. Henderson, *AWE International Magazine*, 2009, **20**.
26 P. C. A. Jerónimo, A. N. Araújo and M. Conceição B.S.M. Montenegro, *Talanta*, 2007, **72**, 13-27.
27 X.-D. Wang and O. S. Wolfbeis, *Anal. Chem.*, 2012, **85**, 487-508.
28 X. Wang, N. Miura and N. Yamazoe, *Sens. Actuators, B*, 2000, **66**, 74-76.
29 C. N. Xu, N. Miura, Y. Ishida, K. Matuda, N. Yamazoe, *Sens. Actuators, B*, 2000, **65**, 163-165.
30 W. Goepel and K. D. Schierbaum, *Sens. Actuators, B*, 1995, **26-27**, 1-12.
31 Y.-D. Wang, X-H. Wu, Q. Su, Y-F. Li and Z-L. Zhou, *Solid-State Electron.*, 2001, **45**, 347-350.
32 M. Aslam, V. A. Chaudhary, I. S. Mulla, S. R. Sainkar, A. B. Mandale, A. A. Belhekaar and K. Vijayamohanan, *Sens. Actuators, A*, 1999, **75**, 162-167.
33 B. T. Marquis and J. F. Vetelino, *Sens. Actuators, B*, 2001, **1-2**, 100-110.
34 I. Lähdesmäki, A. Lewenstam and A. Ivaska, *Talanta*, 1996, **43**, 125-134.

35 A. L. Kukla, Y. M. Shirshov and S. A. Piletsky, *Sens. Actuators, B*, 1996, **37**, 135-140.
36 K. Crowley, A. Morrin, A. Hernandez, E. O'Malley, P. G. Whitten, G. G. Wallace, M. R. Smyth and A. J. Killard, *Talanta*, 2008, **77**, 710-717.
37 A. Spetz, M. Armgath, I. Lundström, *J. Appl. Phys*., 1988, **64**, 1274-1283.
38 P. T. Moseley, *Meas. Sci. Technol*., 1997, **8**, 223-237.
39 P. Heiduschka, M. Preschel, M. Rösch and W. Goepel, *Biosens. Bioelectron*., 1997, **12**, 1227-1231.
40 S. Tao, L. Xu and J. C. Fanguy, *Sens. Actuators, B*, 2006, **115**, 158-163.
41 W. Cao and Y. Duan, *Sens. Actuator, B*, 2005, **110**, 252-259.
42 A. Persad, K.-F. Chow, W. Wang, E. Wang, A. Okafor, N. Jespersen, J. Mann and A. Bocarsly, *Sens. Actuators, B*, 2008, **129**, 359-363.
43 Y. Huang and S. Tao, *J. Sensor Technol.*, 2011, **1**, 29-35.
44 C. Tyszkiewicz, P. Karasiński and R. Rogoziński, *Acta Phys. Pol. A*, 2012, **122**, 915-920.
45 A. Yimit, K. Itoh and M. Maruabayashi, *Sens. Actuators, B*, 2003, **88**, 239-245.
46 E. Scorsone, S. Christie, K.C. Persaud, P. Šimon and F. Kvasnik, *Sens. Actuators, B*, 2003, **90**, 37-45.
47 H. Manap, G. Dooly, S. O'Keeffe and E. Lewis, *Sens. Actuators, B*, 2011, **154**, 226-231.
48 R. Klein and E. Voges, *Sens. Actuators, B*, 1993, **11**, 221-225.
49 V. Chernyak, R. Reisfeld, R. Givshi and D. Venezky, *Sens. Mater*., 1990, **2**, 117-126.
50 T. Grady, T. Butler, B. D. MacCraith, D. Diamond and M. A. McKervey, *Analyst*, 1997, **122**, 803-806.
51 L. Peng, X. Yang, L. Yuan, L. Wang, E. Zhao, F. Tian and Y. Liu, *Opt. Commun.*, 2011, **284**, 4810-4814.
52 F. Galindo, J. C. Lima, S. V. Luis, M. J. Melo, A. J. Parola and F. Pina, *J. Mater. Chem.*, 2005, **15**, 2840-2847.
53 S. Widmer, M. Dorrestijn, A. Camerlo, S. K. Urek, A. Lobnik, C. E. Housecroft, E. C. Constable and L. J. Scherer, *Analyst*, 2014, **139**, 4335-4342.
54 Y. Takagai, Y. Nojiri, T. Takase, W. L. Hinze, M. Butsugan and S. Igarashi, *Analyst*, 2010, **135**, 1417-1425.
55 X. Chen, Y. Dai, Z. Li, Z. Zhang and X. Wang, *J. Anal. Chem*., 2001, **370**, 1048-1051.
56 K. Waich, T. Mayr and I. Klimant, *Talanta*, 2008, **77**, 66-72.

57 G. J. Mohr, S. Draxler, K. Trznadel, F. Lehmann and M. E. Lippitsch, *Anal. Chim. Acta*, 1998, **360**, 119-128.
58 X. Chen, L. Lin, P. Li, Y. Dai and X. Wang, *Anal. Chim. Acta*, 2004, **506**, 9-15.
59 H. S. Mader and O. S. Wolfbeis, *Anal. Chem.*, 2010, **82**, 5002-5004.
60 G. G. Pérez-Sánchez, E. F. Pinzón-Escobar, G. E. Sandoval-Romero and J. A. Álvarez Chávez, *J. Phys. Conf. Ser.* **582**, 2015.
61 B. Renganathan, D. Sastikumar, G. Gobi, N. R. Yogamalar and A. C. Bose, *Opt. Laser Technol.*, 2011, **43**, 1398-1404.
62 S. Korposh, W. Batty, S. Kodaira, S.-W. Lee, S. W. James, S. M. Topliss and R. P. Tatam, Proceedings of SPIE in Fourth European Workshop on Optical Fibre Sensors, 2010.
63 A. S. Kuchyanov, P. A. Chubakov, H. Spisser and A. I. Plekhanov, 2013, arXiv:1308.5086 [physics.optics].
64 L. L. Tan, M. Ahmad and Y. H. Lee, *Sens. Actuators, B*, 2012, **171-172**, 994-1000.
65 Z. Gu and P. Liang, *Opt. Laser Technol.*, 2004, **36**, 211-217.
66 Á. Markovics, G. Nagy and B. Kovács, *Sens. Actuators, B*, 2009, **139**, 252-257.
67 Q. Chang, J. Sipior, J. R. Lakowicz and G. Rao, *Anal. Biochem.*, 1995, **232**, 92-97.
68 K. Waich, S. Borisov, T. Mayr and I. Klimant, *Sens. Actuators, B*, 2009, **139**, 132-138.
69 US Pat., 20110236986 A1, 2011.
70 T. Abel, B. Ungerböck, I. Klimant and T. Mayr, *Chem. Cent. J.*, 2012, **6**, 124-133.
71 M. Preuss and F. Bechstedt, *Phys. Rev. B*, 2006, **73**, 155413-155420.
72 P. Chambers, W. B. Lyons, T. Sun and K. T. V. Grattan, *J. Phys. Conf. Ser.* **85**, 2007.
73 R. G. Dickinson, R. T. Dillon and F. Rasetti, *Phys. Rev.*, **34**, 1929, 582-589.
74 C. J. Brinker and G. W. Scherer in Sol-Gel Science, *J. Non Cryst. Solids*, 1985, **70**, 301-322.
75 H. Schmidt, *J. Non Cryst. Solids*, 1985, **73**, 681-651.
76 H. Schmidt, *J. Non Cryst. Solids*, 1988, **100**, 51-64.
77 B. J. Melde, B. J. Johnson and P. T. Charles, *Sensors*, 2008, **8**, 5202-5228.
78 R. Gupta, S. Mozumdar and N. K. Chaudhury, *Biosens. Bioelectron.*, 2005, **20**, 1358-1365.

79 C. J. Brinker, A. J. Hurd, G. C. Frye, K. J. Ward and C. S. Ashley, *J. of Non-Cryst. Soilds*, 1990, **121**, 294-302.
80 C. McDonagh, F. Sheridan, T. Butler and B. D. MacCraith, *J. Non-Cryst. Solids*, 1996, **194**, 72-77.
81 O. Lev, M. Tsionsky, L. Rabinovich, V. Glezer, S. Sampath, I. Pankratov and J. Gun, *Anal. Chem.*, 1995, **67**, 22A-30A.
82 D. Avnir, *Acc. Chem. Res.*, 1995, **28**, 328-334.
83 B. D. MacCraith and C. McDonagh, *J. of Fluoresc.*, 2002, **12**, 333-342.
84 B. D. MacCraith, C. McDonagh, A. K. McEvoy, T. Butler, G. O'Keefe and V. Murphy, *J. Sol-Gel Sci. Technol.*, 1997, **8**, 1053-1061.
85 R. Zusman, C. Rottmann, M. Ottolenghi and D. Avnir, *J. Non-Cryst. Solids*, 1990, **122**, 107-109.
86 J. Lin and C. W. Brown, *Trends Anal. Chem.*, 1997, **16**, 200-211.
87 C. Sanchez, B. Julián, P. Belleville and M. Popall, *J. Mater. Chem.*, 2005, **15**, 3559-3592.
88 L. Basabe-Desmonts, D. N. Reinhoudt and M. Crego-Calama, *Chem. Soc. Rev.*, 2007, **36**, 993-1017.
89 C. Malins, T. M. Butler and B. D. MacCraith, *Thin Solid Films*, 2000, **368**, 105-110.
90 V. G. Parale, D. B. Mahadik, M. S. Kavale, S. A. Mahadik, A. Venkateswara Rao and S. Mullens, *J. Porous Mater.*, 2013, **20**, 733-739.
91 B. J. Privett, J. Youn, S. A. Hong, J. Lee, J. Han, J. H. Shin and M. H. Schoenfisch, *J. Am. Chem. Soc.*, 2011, **27**, 9597-9601.
92 C. McDonagh, B. D. MacCraith and A. K. McEvoy, *Anal. Chem.*, 1998, **70**, 45-50.
93 R. M. Bukowski, R. Ciriminna, M. Pagliaro and F. V. Bright, *Anal. Chem.*, 2005, **77**, 2670-2672.
94 C.-S. Chu and Y.-L. Lo, *Sens. Actuators*, *B*, 2008, **129**, 120-125.
95 C.-S. Chu and Y.-L. Lo, *Sens. Actuators*, *B*, 2007, **124**, 376-382.
96 C. Preininger, M. Ludwig and G. J. Mohr, *J. Fluoresc.*, 1998, **8**, 199-205.
97 R. Pardo, M. Zayat and D. Levy, *J. Photochem. Photobiol., A*, 2008, **198**, 232-236.
98 A. Lobnik, I. Oehme, I. Murkovic and O. S. Wolfbeis, *Anal. Chim. Acta*, 1998, **367**, 159-165.
99 A. Lobnik and O. S. Wolfbeis, *Sens. Actuators, B*, 1998, **51**, 203-207.
100 F. Hoffmann, M. Cornelius, J. Morell and M. Fröba, *Angew. Chem. Int. Ed.*, 2006, **45**, 3216-3251.
101 B. Samiey, C.-H. Chen and J. Wu, *Materials*, 2014, **7**, 673-726.

102 T. Yokoi, H. Yoshitake and T. Tatsumi, *J. Mater. Chem.*, 2004, **14**, 951-957.
103 H. H. Lim and A. Stein, *Chem. Mater.*, 1999, **11**, 3285-3295.
104 D. Brühwiler, *Nanoscale*, *2010,* **2**, 887-892.
105 N. Gartmann and D. Brühwiler, *Angew. Chem. Int. Ed.*, 2009, **48**, 6354-6356.
106 N. Gartmann, C. Schütze, H. Ritter and D. Brühwiler, *J. Phys. Chem. Lett.*, 2010, **1**, 379-382.
107 S. Huh, J. W. Wiench, B. G. Trewyn, S. Song, M. Pruski and V. S.-Y. Lin, *Chem. Commun.*, 2003, 2364-2365.
108 K. Möller, J. Kobler and T. Bein, *J. Mater. Chem.*, 2006, **17**, 624-631.
109 F. O. M. Gaslain, C. Delacôte, A. Walcarius and B. Lebeau, *J. Sol-Gel Sci. Technol*., 2009, **49**, 112-124.
110 B. Lei, H. Zhang, S. Lu, Z. Zheng, W. Li and Y. Wang, *Adv. Funct. Mater.*, 2006, **16**, 1883-1891.
111 H. Zhang, Y. Sun, K. Ye, P. Zhang and Y. Wang, *J. Mater. Chem.,* 2005, **15**, 3181-3186.
112 X. Xu and H. Xiao, *J. Lumin.,* 2012, **132**, 2251-2258.
113 X. Wu, L. Song, B. Li and Y. Liu, *J. Lumin.*, 2010, **130**, 374-379.
114 L.-L. Li, H. Sun, C.-J. Fang, J. Xu, J.-Y. Jin and C.-H. Yan, *J. Mater. Chem.*, 2007, **17**, 4492-4498.
115 R. Métivier, I. Leray, B. Lebeau and B. Valeur, *J. Mater. Chem*., 2005, **15**, 2965-2973.
116 K. Kledzik, M. Orlowska, D. Patralska, M. Gwiazda, J. Jezierska, S. Pikus, R. Ostaszewski and A. M. Klonkowski, *Appl. Surf. Sci.*, 2007, **2**, 441-451.
117 L. Gao, Y. Wang, J. Wang, L. Huang, L. Shi, X. Fan, Z. Zou, T. Yu, M. Zhu and Z. Li, *Inorg. Chem.*, 2006, **45**, 6844-6850.
118 B. Xiao, J. Zhao, X. Liu, P. Wang and Q. Yang, *Micropor. Mesopor. Mat.*, 2014, **199**, 1-6.
119 W. Jingxia, *J. Lumin.*, 2014, **151**, 41-46.
120 B. Wang, L. Zhang, B. Li, Y. Li, Y. Shi and T. Shi, *Sens. Actuators, B*, 2014, **190**, 93-100.
121 Z. Dong, X. Tian, Y. Chen, J. Hou and J. Ma, *RSC Adv.,* 2013, **3**, 2227-2233.
122 M. H. Lee, S. J. Lee, J. H. Jung. H. Lim and J. S. Kim, *Tetrahedron*, 2007, 12087-12092.
123 H. Zhang, P. Zhang, K. Ye, Y. Sun, S. Jiang, Y. Wang and W. Pang, *J. Lumin.*, 2006, **117**, 68-74.

124 G. Wirnsberger, P. Yang, B. J. Scott, B. F. Chmelka and G. D. Stucky, *Spectrochim. Acta A*, 2001, **57**, 2049-2060.
125 G. Wirnsberger, P. Yang, B. J. and G. D. Stucky, *Chem. Commun.*, 2001, 119-120.
126 O. B. Miled, D. Grosso, C. Sanchez and J. Livage, *J. Phys. Chem. Solids*, 2004, **65**, 1751-1755.
127 T. Asefa, C. T. Duncan and K. K. Sharma, *Analyst*, 2009, **134**, 1980-1990.
128 B. J. Scott, G. Wirnsberger and G. D. Stucky, *Chem. Mater.*, 2001, **13**, 3140-3150.
129 Y.-C. Chang, H. Bai, H.-S. Chiang, M. Karthik, S.-N. Li, J.-N. Hsu and H.Y. Shih, *J. Air Waste Manage.*, 2012, **62**, 838-845.
130 S. Fiorill, B. Onida, D. Macquarrie and E. Garrone, *Sens. Actuators, B*, 2004, **100**, 103-106.
131 Y-C. Chang, H. Bai, S.-N. Li and C.-N. Kuo, *Sensors*, 2011, **11**, 4060-4072.
132 C.-S. Chu, *Key Eng. Mater.*, 2012, **516**, 612-617.
133 C.-S. Chu, Y.-L. Lo and T.W. Sung, *Talanta*, 2010, **82**, 1044-1051.
134 J. R. Lakowicz, in *Principles of Fluorescence Spectroscopy,* , Chapter 1: Introduction to Fluorescence, Springer, New York, 3rd edn., 2010, pp. 1-10.
135 http://en.wikipedia.org/wiki/Fluorescence, accessed March 2015.
136 J. R. Lakowicz, in *Principles of Fluorescence Spectroscopy*, Chapter 1: Introduction to Fluorescence, Springer, New York, 3rd edn., 2010, p. 13.
137 J. R. Lakowicz, in *Principles of Fluorescence Spectroscopy,* Chapter 13: Energy Transfer, Springer, New York, 3rd edn., 2010, pp. 443-453.
138 R. M. Clegg, in *Laboratory Techniques in Biochemistry and Molecular Biology*, vol. 33, *FRET and FLIM Techniques*, ed. T. W. J. Gadella, Elsevier, Burlington, 2009, pp. 1-57.
139 http://en.wikipedia.org/wiki/F%C3%B6rster_resonance_energy_transfer, accessed March 2015.
140 O. S. Wolfbeis, *J. Mater. Chem.*, 2005, **15**, 2657-2669.
141 M. Schäferling, *Angew. Chem. Int. Ed.*, 2012, **51**, 2-25.
142 J. R. Lakowicz, in *Principles of Fluorescence Spectroscopy*, Chapter 19: Fluorescence Sensing, Springer, New York, 3rd edn., 2010, p. 633.
143 B. D. MacCraith, C. M. Mc Donagh, G. O'Keeffe, A. K. McEvoy, T. Butler and F. R. Sheridan, *Sens. Actuators, B*, 1995, **29**, 51-57.

Chapter 2

Coumarin meets Fluorescein: A FRET enhanced Optical Ammonia Gas Sensor

2.1 Introduction

This chapter focuses on the development of an optical ammonia gas sensor, the sensing mechanism of which is based on Förster resonance energy transfer (FRET) between two well-known dyes concerning this scope: coumarin and fluorescein. Few FRET-based optical chemosensors for the detection of ammonia have been reported[1-4] and the advantages have been highlighted in Section 1.8. They can generate dual or multiple emissions under a single wavelength excitation, resulting in more effective ratiometric detection in comparison to those that need two separate excitation wavelengths.[5] For this preliminary study, fluorescein was chosen as the ammonia sensitive acceptor dye to allow comparisons with established benchmarks.[6,7] The dyes were immobilized into an organically modified silicate matrix during polymerization of methyltriethoxysilane with trifluoropropyltrimethoxysilane on a poly(methyl methacrylate) (PMMA) substrate. The resulting dye-doped xerogel films were exposed to different concentrations of gaseous ammonia and their fluorescence spectra were measured and compared. The coumarin/fluorescein composition was optimized in order to obtain the best ammonia sensitivity. The best dye composition was tested in the flow cell gas sensor setup which was built in house. Most of the content of this chapter was published in Analyst in 2014.[8]

2.2 Experimental

2.2.1 Chemical reagents and materials

Fluorescein (F), 7-diethylamino-4-methylcoumarin (C or coumarin), 3,3,3-trifluoropropyltri-methoxysilane, methyltriethoxysilane, triethylamine (99% in water), methylamine (40% in water) and hydrochloric acid (37%) were purchased from Sigma Aldrich. Ethanol in HPLC grade, $MgCl_2$ and NaCl were obtained from Fluka. All chemicals were used without further purification. Custom mixed gases 96.2 ppm ± 2% rel. NH_3 in N_2 (≥ 99.8%), 0.101 ± 1% rel. NH_3 in N_2 and pure N_2 gas were acquired from Carbogas. PMMA microscope

slides (25 mm × 75 mm × 1 mm) and a 0.5 mm thick PMMA foil were purchased from microfluidic ChipShop.

2.2.2 Sol preparation

Coumarin/fluorescein (C/F) sols were prepared by dissolving the desired amount (6.25, 12.5, 25, 37.5, 50, 62.5 and 75 µmol) of the dyes in 5 mL of ethanol. After sonication (UltrasonicCleaner from VWR, 45 kHz, 80 W) of the solution for 10 min at room temperature (RT), methyltriethoxysilane (1.793 mL, 9 mmol) and 3,3,3-trifluoropropyltrimethoxysilane (0.576 mL, 3 mmol) were added. After a further 10 min of sonication, 0.1 M HCl (0.08 mL) and water (0.64 mL) were added to the solution. The sol was sonicated for another 20 min and then aged for 24 h at RT ("aged sol"). Figure 1a illustrates the sol preparation pathway.

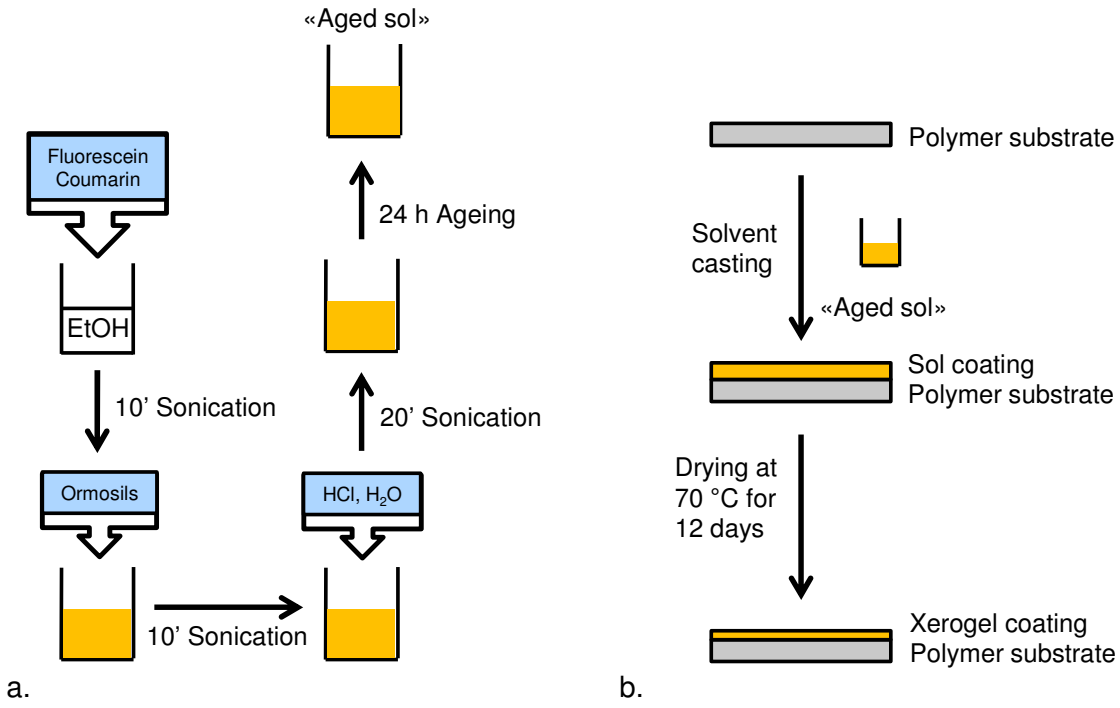

Figure 1: a.: Sol preparation pathway; b.: xerogel film preparation pathway.

2.2.3 Xerogel preparation

Fluorescence and UV-visible spectroscopy measurements. 5 µL of aged sols were solvent cast on PMMA foils (4.5 mm × 4.5 mm × 0.5 mm) with a micropipette. The sol-coated PMMA substrates were dried in an oven at 70 °C

for 12 days to ensure stable gel composition. The scheme in Figure 1b depicts the xerogel film preparation pathway.

Gas sensor measurements. Different amounts (20, 40 and 60 µL) of aged sols were solvent cast onto PMMA plates (15 mm × 15 mm × 1 mm) with a micropipette. The sol was homogenously distributed over the substrate with the micropipette tip. After 10 min drying in air, the sol-coated PMMA substrates were dried in an oven at 70 °C for 12 days.

2.2.4 Characterization methods

ATR-IR, UV-visible and fluorescence spectroscopy. ATR-IR spectra were obtained using a FT-IR Biorad spectrophotometer equipped with a Specac Golden Gate bridge. Spectra of the sol solution, sol-gel and pestled xerogel were recorded.

Fluorescence spectra were recorded in the range of 385–650 nm on a Biorad Fluorescence spectrophotometer. Both the excitation and emission slit were set to 10 nm and the detector voltage was set to low. The small xerogel-coated PMMA plates were horizontally pinched into the wells of a microtitre wellplate at the same height. The plates were exposed to ammonia gas by adding 20 µL of the desired aqueous ammonia solutions to the well bottom by a microsyringe. The well plate was then covered by the corresponding lid and enwrapped with parafilm. By adding the same amount of 1 M HCl, $MeNH_2$, NEt_3 and H_2O to the wells, the xerogels were exposed to HCl, $MeNH_2$, NEt_3 and H_2O vapour respectively. Before each fluorescence measurement, the loaded wellplate was stored in a conditioned room (21 °C, 50% rel. air humidity) for 30 min to ensure same measurement conditions. The NH_3 and $MeNH_2$ vapour concentrations within the wells were calculated based on the reported partial vapour pressure of NH_3 and $MeNH_2$ in solution.[9-11]

UV-visible absorption spectra were measured between 300 and 800 nm on a Biorad spectrophotometer with a slit width of 1.0 nm. The experimental procedure was similar to the fluorescence experiments.

Refractive index measurements. Refractive index measurements on the sols were performed on an instrument from Atago equipped with an illuminator. The

refractive index of an undoped solid xerogel was determined using certified refractive index liquids made by Cargille labs.

Contact angle measurements. The measurements were performed on a Krüss G10 instrument. A droplet of nanopure water (3 µL) was deposited on the xerogel film. The measurement was repeated five times and had an accuracy of ± 2°.

Rheometry measurements. Viscosity measurements were performed on a plate rheometer from Anton Paar (Physica MCR 301). The change in viscosity of the sol upon heating was measured by placing a vial containing a 24 h aged sol in a preheated oven at 70 °C. The shrinking and gelling sol, due to solvent evaporation and heat, was measured every 30 min.

Profilometry measurements. Profilometry experiments were performed with a Vecco Dektak 150 device to determine the xerogel film thickness. Before solvent-casting, two opposite corners of the corresponding PMMA substrates were covered with tape. The sol was then solvent cast and homogenously distributed over the whole substrate with the micropipette tip. After drying for 12 days, the tapes were carefully removed to obtain a smooth xerogel borderline. The stylus was placed on one xerogel corner and moved over the coated area towards the uncoated opposite corner. For evaluation of the thickness, the profile average with standard deviation was calculated. The given xerogel thicknesses were calculated from the average of 5 measured plates.

Porosity measurements. Nitrogen adsorption isotherms were measured at -196 °C using a NOVA 3000e Surface Area and Pore Size Analyzer from Quantachrome instruments. The samples were obtained by drying the sols in a petri dish. After 12 days of drying at 70 °C, the xerogel was scrapped out and the powder was degassed at RT for 16 h.

Atomic force microscopy (AFM) measurements. AFM images were recorded with a Dimension 3100 equipped with a Nanoscope V Controller from Bruker. The tapping mode technique with following properties was used: force constant 42 N/m, resonant frequency 330 kHz, the nominal tip radius of curvature < 7

nm, the cantilever (Nanoandmore) length 125 μm. Topography and phase images were obtained simultaneously. Samples were scanned at ambient temperature.

Solid-state NMR spectroscopy. Solid-state ^{13}C and ^{29}Si NMR spectra were recorded on a Bruker AV400 NMR spectrometer at frequencies of 100.6 MHz for ^{13}C CP/MAS NMR and 79.5 for ^{29}Si CP/MAS NMR. The MAS spin rate was 4,000 Hz, and the relaxation time was 4 s with 3 ms contact time.

Lifetime measurements. Lifetime measurements were performed on a Quantaurus-Tau compact fluorescence lifetime spectrometer from Hamamatsu. The xerogel was excited at 365 nm and the fluorescence emission was recorded at 428 nm. The xerogel film on PMMA was exposed for 20 min to NH_3 (100, 400, 1,000 and 2,000 ppm) outside the instrument in a closable plastic box and were then rapidly deposited in the device for the lifetime measurement. The lifetime was obtained by first order fitting of the fluorescence decay curve. The chi-squared (χ^2) test was performed automatically by the appropriate software.

2.2.5 Gas sensor measurements

Laboratory set-up for testing the ammonia sensing probes. Xerogel-coated plates were placed in a flow cell as shown in Figure 2. The plates were illuminated from the top by a 0.4 W UV-LED of peak wavelength 385 nm (FWHM bandwidth 10 nm) purchased from Thorlabs. To measure fluorescence emission, the photodetector (a photodiode from Thorlabs) was placed orthogonal to the incoming radiation, the PMMA sample plate acting as a waveguide. Additionally, an optical band-pass filter was placed in front of the detector, which had a 90% transmission band of 415–455 nm provided by Semrock (FF02-435/40-25). The inside of the flow cell was painted black to reduce reflections of the direct light. Electronic readout was based on a photodiode circuit and a LabView-controlled digital multimeter. The time-dependent voltage signal, which was proportional to the emitted light intensity, was post-processed in LabView using a low-pass filter and baseline correction. The flow cell was connected to gas supplies as depicted in Figure 3. The gas flow could be switched between NH_3/N_2 mixture and nitrogen using manual valves (3). During the experiments, the flow rate (800 ml ± 50 mL/min), the

temperature (20 ± 2 °C), and the humidity (< 2%) were monitored in the line using a CMOSens EM1 (Sensirion) and an MSR 145 (Sensirion) respectively.

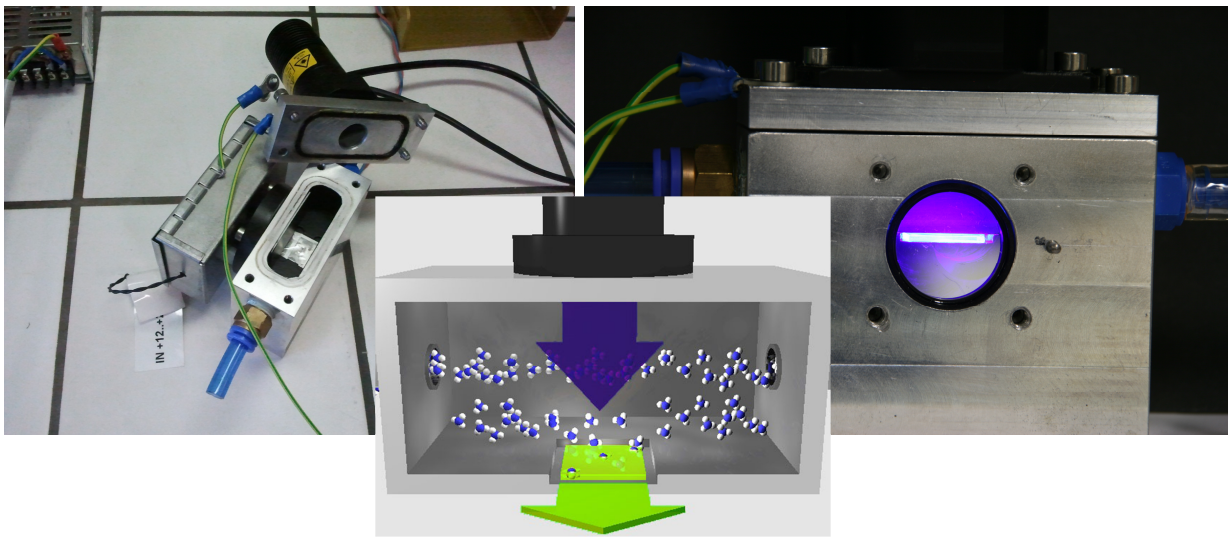

Figure 2: Left: photograph of the gas sensor. The photodetector and electronics was placed on the side of the flow cell. Right: the photograph was taken from the detector's side. The sensing plate was deposited in the flow cell. NH_3 gas enters the flow cell from one side and leaves it over the opposite side. The plate is illuminated from the top by a UV-LED through a UV-transparent window. Passing radiation is measured through an opening in the front of the cell. The upstreamed filter filters the irrelevant radiations. Middle: schematic illustration of the flow cell gas sensor.

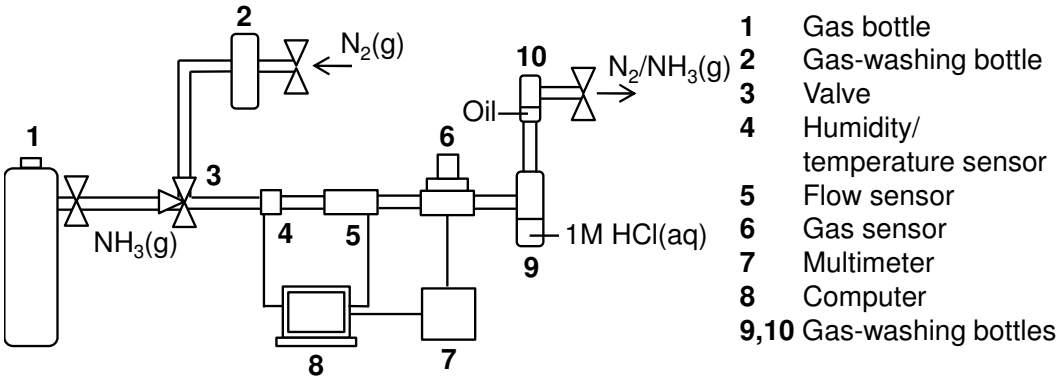

Figure 3: Schematic of the experimental setup.

Measurement and measurement evaluation. Before each measurement, the system was flushed with N_2 gas for 5 min. An experiment always started with a 600–900 s N_2 gas flush followed by flush of a NH_3 gas mixture. Normally, at least five cycles with NH_3 response and N_2 recovery were measured to ensure system stabilisation and repeatability of the experiments. Response and recovery times were kept constant at 35 min. The amplification of the electronic was constant for each measurement. The LED light intensity was minimally adjusted

to achieve the same starting voltage (light intensity) for each coating (thin films were less fluorescent than thick films). Since the photodiode exhibits a linear output current versus light intensity,[12] the NH_3 signals still can be compared among one another. The drift was corrected by fitting a double exponential equation to the turning point of each cycle (highest point of the signal recovery with N_2 gas). The signal noise was reduced by using a fifth order Butterworth low-pass filter with 3 mHz cut-off frequency.

Humidity responses to 33 ± 4% and 75 ± 3% were obtained by installing a second N_2-line with a gas washing bottle filled with the corresponding saturated salt solution ($MgCl_2$ and NaCl).

2.3 Results and Discussion

2.3.1 Sensing film preparation

Sol-gels and xerogels were prepared using standard hydrolytic methods. Fluorinated ormosil precursors are widely used for reducing the absorption of ormosil derived matrices[13] which leads to more efficient guiding and transmission of light through the sensing silica matrix. The further advantages of sol-gel derived films based on ormosils were already highlighted in Section 1.4. The formation of the sol-gel as a result of hydrolysis and condensation results in an increase in viscosity. Rheometry measurements showed that the viscosity of the prepared sols remained constant at room temperature even at longer ageing times, indicating that the condensation reaction proceeds slowly. In general, at pH < 7 the rate of the condensation reaction is limited by the lack of available hydroxide anions.[14] The polymerization was finally induced by heating the sol to 70 °C. The condensation degree during curing at 70 °C was followed by rheometry measurements. The thermal polymerization resulted in an increase in viscosity as illustrated in Figure 4. The increase in viscosity is small for the first 100 min but significant between 120 and 170 min indicating that the main polymerization starts during this time range. After 170 min, the sol-gel was too rubbery to be accurately measured by a plate rheometer. Twelve days drying at 70 °C of solvent cast acid catalysed sol on the PMMA substrate resulted in fracture free homogenous xerogel films. Organofunctional alkoxysilanes are often used to reduce the degree of cross-linking of the material which often

leads to less capillary stress during solvent evaporation and results in crack-free and more flexible sol-gel films.[15-28]

AFM and nitrogen sorption experiments on the xerogel films revealed that the xerogels were not porous, which is certainly not beneficial to fast gas diffusion. However, it is known that the silicon-based layers are highly permeable for gases.[29]

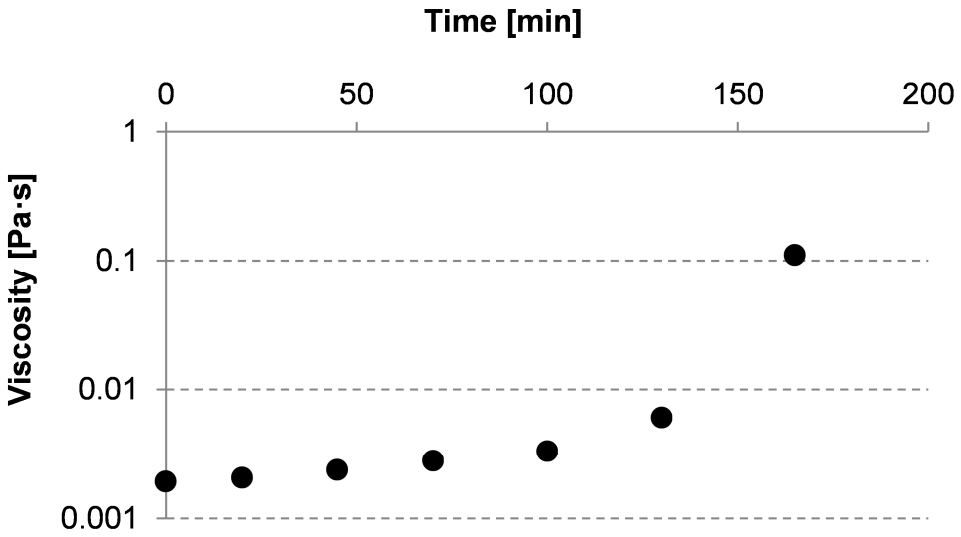

Figure 4: Plot showing the increase in viscosity due to condensation at 70 °C.

Coumarin/fluorescein(C/F)-doped xerogels showed an increase in fluorescence emission at 442 nm and a decrease in fluorescence emission at 500–540 nm during the first 8 to 10 days of drying when excited at 375 nm. In order to achieve constant fluorescence emission, a curing time of 12 days was necessary. The water contact angle of dye doped and undoped xerogel was 90 ± 2°. Exposure of the film to NH_3 gas did not lead to a change in contact angle. The hydrophobic character of these xerogels could be demonstrated by a short leaching in water experiment, where a C/F doped xerogel was glued inside of a cuvette without being touched by the laser of the spectrophotometer. The cuvette was filled with water and the spectra was taken each 30 min for 24 h. The absence of an absorption band at 380 (coumarin) and 480 nm (fluorescein) showed clearly, that the dye did not leach from the dense xerogel network.

ATR-infrared and NMR spectroscopy is commonly used to monitor different stages of sol-gel processing of silica gels and is an elegant method to verify the formation of siloxane bridges upon polymerization.[30,31] The main change in ATR-IR spectra upon thermal sol to xerogel evolution is based on the ethanol and ormosil consumption and the formation of Si–O–Si bonds.[30] This was

detected by the disappearance of the ethanol and ormosil related bands at 3330, 2970, and 1380 cm^{-1} and by the simultaneous formation and intensification of the siloxane (Si–O–Si, Si–O) related bands at 1000, 900 and 770 cm^{-1} after 12 days curing time as illustrated in Figure 5.

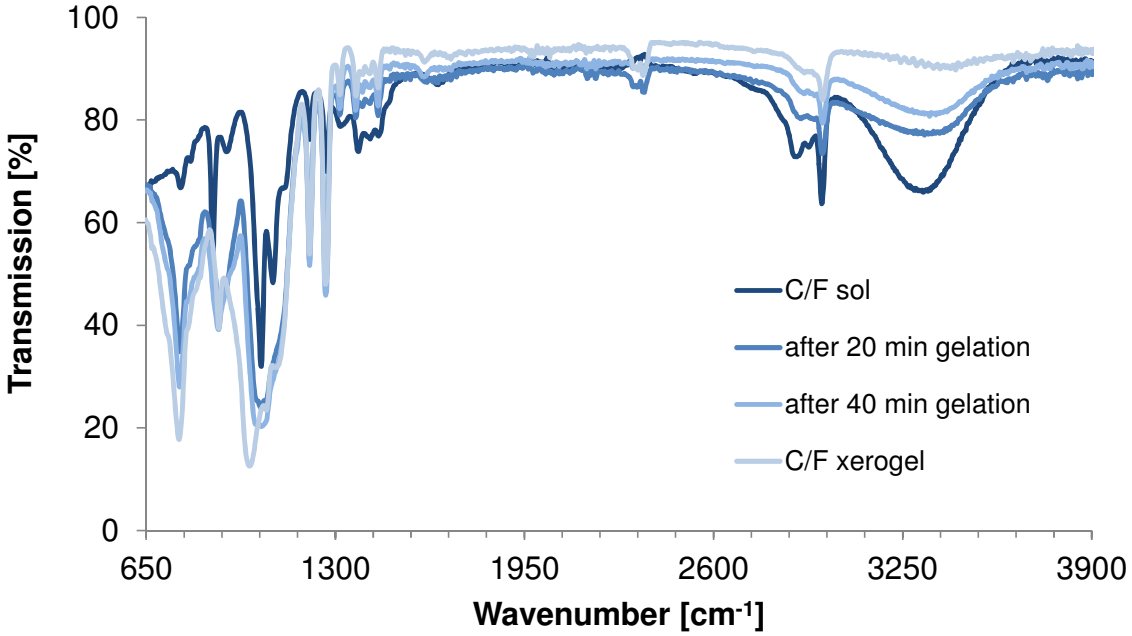

Figure 5: Change in IR spectra upon gelation of the sol at 70 °C.

The solid state ^{29}Si NMR spectrum gives information about the connectivity of the siloxane bonds. Upon condensation one, two or three siloxane bridges can be formed. Two intensive signals at δ –56.2 and –65.5 ppm indicated the formation of two and three siloxane bridges.[31] The signals exhibited the same intensity revealing that their ratio is about the same. The absence of the signal for no or only one siloxane bridge demonstrates an extensive and rigid organic network in the final film. The spectra of an undoped and C/F doped xerogel were identical.

2.3.2 Choice of the dyes and sensing mechanism

Fluorescein derivatives have been used as sensing species displaying linear dependency over wide ranges of ammonia concentrations.[6,7,32] Depending on the ambient pH value, fluorescein exists in cationic, neutral, monoanionic or dianionic forms or as a mixture of them.[33] The acidity constants in solution reported for fluorescein are in the range of $pK_{cationic}$ = 2.00–2.25, $pK_{neutral}$ = 4.23–4.4 and $pK_{monoanionic}$ = 6.31–6.7,[33-35] depending on the specific conditions and measurement techniques. Absorption as well as emission spectra are dependent

on the pH of the environment due to the presence of species in different protonation states.[33] Absorption spectra of the fluorescein doped xerogels after production showed that fluorescein existed in a mixture of neutral (absorption shoulder at 435 and side maximum about 483 nm) and monoanionic forms (absorption peak at 457 and about 483 nm). The fluorescence emission of these claddings occurred between 500 and 600 nm. The two main emission peaks of the xerogel in the absence of ammonia are at 515 and 542 nm (Figure 6). The quantum yields and molar absorptivities of neutral and monoanionic fluorescein ($\Phi F_{neutral}$ = 0.3, $\Phi F_{monoanionic}$ = 0.37)[33] are reported to be small resulting in moderate fluorescence emission, which is in accordance to the findings (Figures 6 and 7).

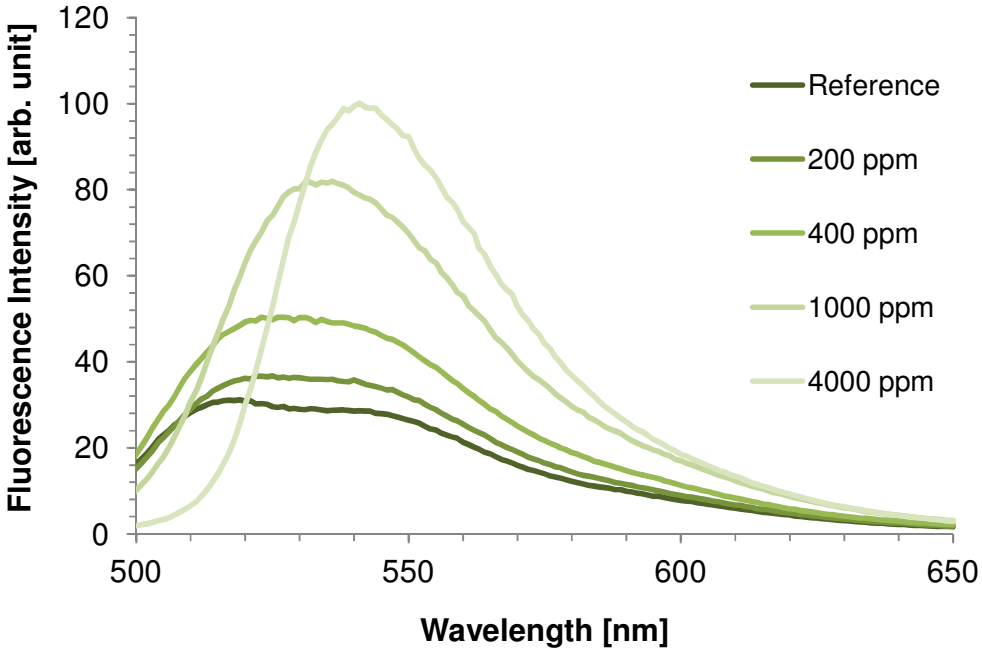

Figure 6: Change in fluorescence emission spectra for a fluorescein doped xerogel (sol composed of 25 µmol fluorescein) upon ammonia exposure (ex: 481 nm).

Ammonia treated xerogels exhibited a much stronger absorption band at 492 nm with a shoulder at 455 nm and an emission band at 542 nm (Figures 6 and 7). The main fluorescein emission band of the monoanions disappeared, indicating that another fluorescein species, the dianionic, became the dominant species. Ammonia (pK_b = 4.74)[36] is detected by deprotonation of the fluorescein dye resulting in a fluorescence enhancement between 500–600 nm when excited at 481 nm (Figure 6), because the resulting deprotonated dianionic molecule is fully conjugated. The high intensity of the emission is in correspondence with

the high reported quantum yield ($\Phi F_{dianionic}$ = 0.93)[33] and the high molar absorptivity of the dianionic fluorescein form. The strong overlap of the decreasing fluorescence band of the monoanionic form with the increasing fluorescence band of the dianionic form made quantitative NH_3 analysis difficult (Figure 6).

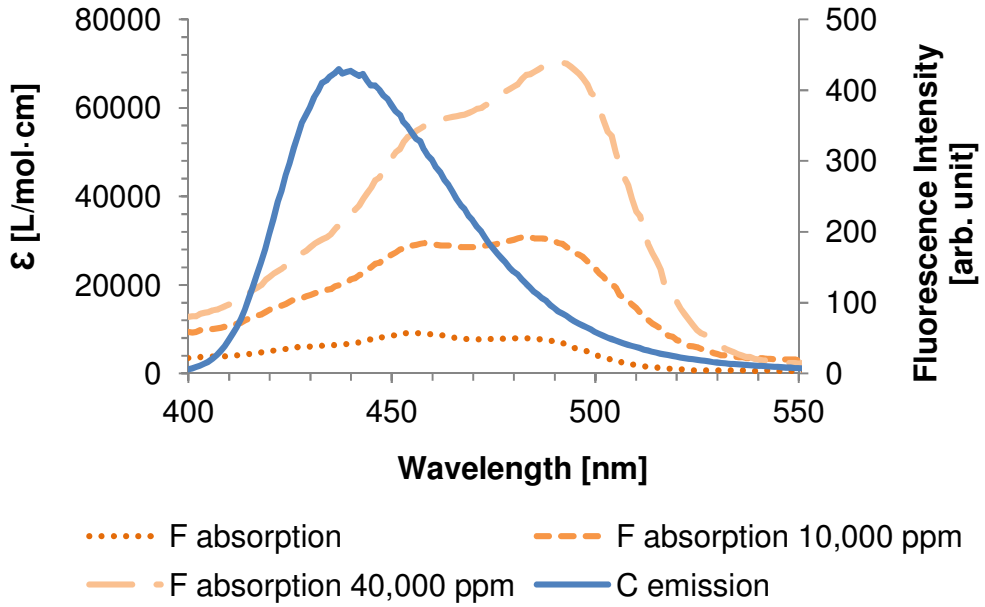

Figure 7: Increasing spectral overlap of C emission and F (mono- and dianion) absorption due to exposure to different ammonia gas concentrations given in ppm. The spectra were obtained from xerogels whose sols were doped with 25 µmol C (ex: 375 nm) or 12.5 µmol F (ex: 481 nm).

Furthermore, the spectral evaluation revealed that the increase in fluorescein fluorescence intensity was not logarithmic when excited at 481 nm. Due to these unsatisfying sensor characteristics of fluorescein xerogels, a FRET sensing mechanism was designed (Figure 8).

As previously discussed in Section 1.7, FRET describes the transfer of the excited state energy from an initially excited donor (D) to an acceptor (A). This process occurs if the emission spectrum of D overlaps with the absorption spectrum of A. The emission wavelength of the newly incorporated second dye, coumarin, overlaps strongly with the absorption wavelength of fluorescein (Figure 7) and FRET between these two dyes is anticipated.

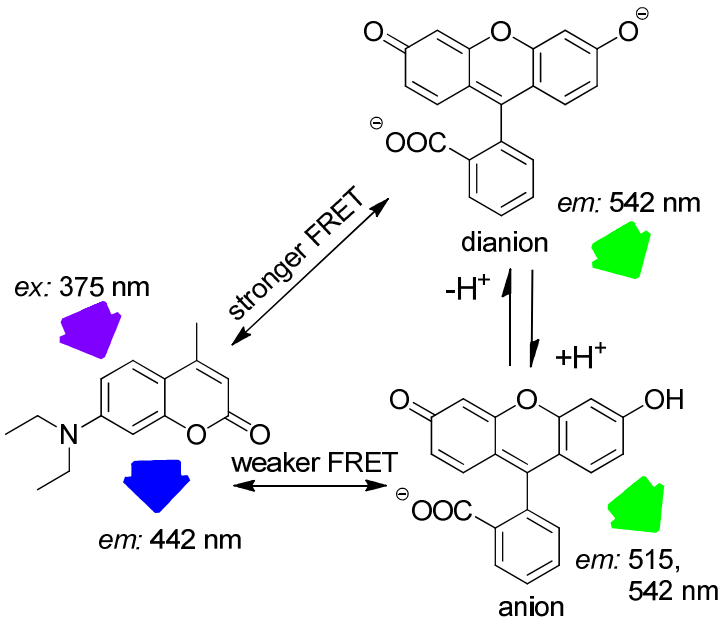

Figure 8: Schematic of the FRET sensing mechanism between coumarin and fluorescein.

The efficiency of the energy transfer in FRET depends on the distance between the donor (coumarin) and the acceptor (fluorescein), as well as on the relative orientation of the donor emission dipole moment and the acceptor absorption dipole moment.[37] Furthermore, the Förster distance R_0 depends on the overlap of the donor emission spectrum with the acceptor absorption spectrum and their mutual molecular orientation as expressed by the following equation:[37]

$$R_0^6 = \frac{9000 Q_0 (ln10) \kappa^2 J}{128 \pi^5 n^4 N_A}$$

Q_0 describes the fluorescence quantum yield of the donor (coumarin) in absence of the acceptor (fluorescein) which was not quantified. The refractive index n of an undoped xerogel (n = 1.404) and the dipole orientation factor κ are constant. The only variable factor in this system is the spectral overlap J. The spectral overlap of coumarin emission and fluorescein absorption bands varied with the ammonia concentration as a consequence of deprotonation of the fluorescein. Upon excitation at 375 nm, coumarin/fluorescein xerogels featured two main emission bands: one between 400–500 nm with main emission peak at 442 nm and a shoulder at 462 nm which correspond to the two mesomeric states of coumarin[38] and the second between 500–600 nm which corresponds to fluorescein with the same emission maxima as observed for pure fluorescein xerogels. The exposure of these xerogels to NH_3 led to the same behaviour in

the fluorescein emission band as illustrated in Figure 6 and to a clear decrease in the coumarin emission intensity. This is a result of a more efficient FRET, since the spectral overlap increased as the fluorescein dianion is formed (Figure 7). The enhanced FRET efficiency resulted in less overall coumarin emission between 400–500 nm, as more energy (photons) is transferred for the dipole-dipole interaction with fluorescein. The signal at 442 nm was much better suited for detection purposes than the fluorescein emission between 500–600 nm since it was much more sensitive to changes of the ammonia concentration and a clear decrease in intensity was observed with increasing ammonia concentration (Figures 9 and 10). This trend was observed for the entire ammonia concentration studied.

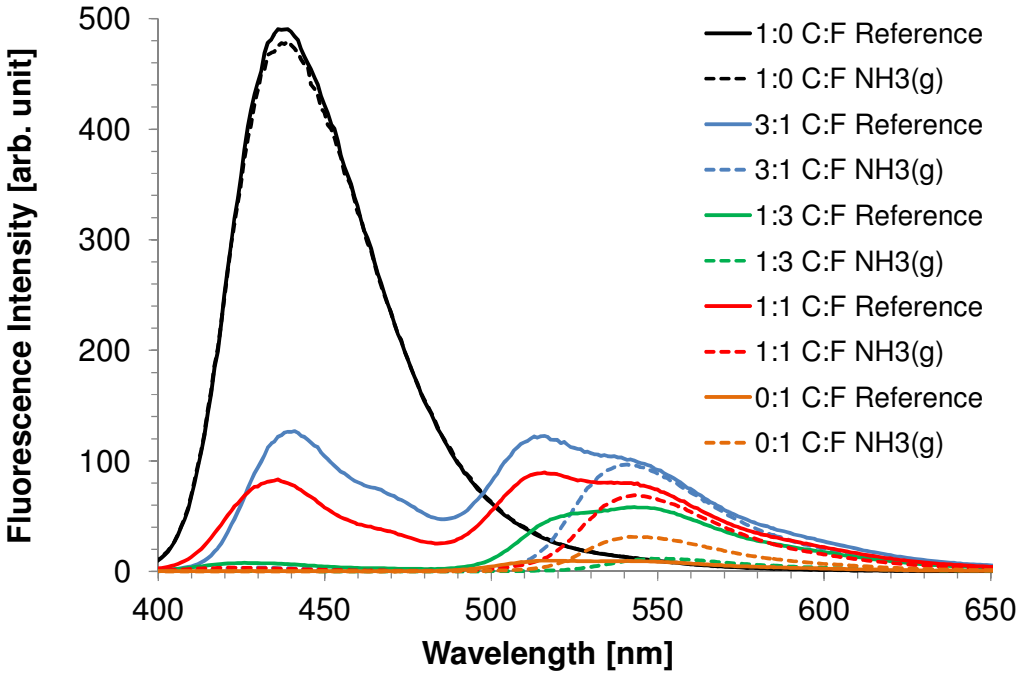

Figure 9: Fluorescence spectra of xerogels with different C/F ratios and their response to 40,000 ppm NH_3 (5% aq. NH_3 solution)(ex: 375 nm). Ratio 1:0 C/F corresponds to a xerogel doped with 25 µmol C and 0 µmol F).

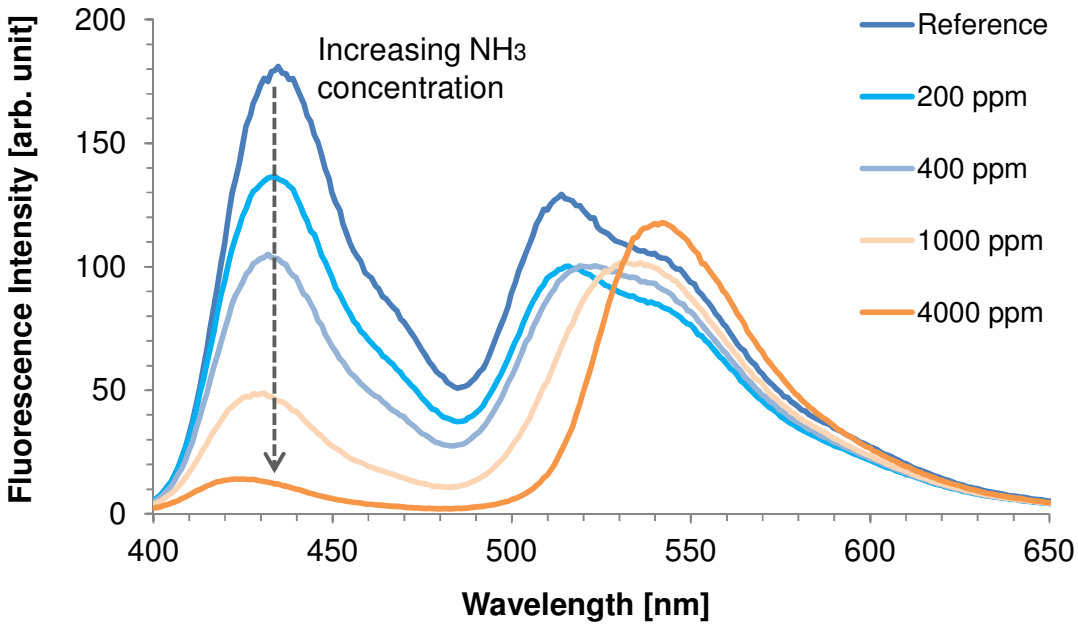

Figure 10: Fluorescence emission spectra observed of a 1:1 coumarin/fluorescein xerogel (sol composed of 25 µmol C and 25 µmol F) upon exposure to different amounts of NH_3 (ex: 375 nm).

The change in fluorescence spectra could also be followed by eye, as the xerogel films changed colour upon ammonia exposure (Figure 11). The fluorescein greenish emission intensified upon exposure to ammonia, whereas the coumarin bluish emission decreased.

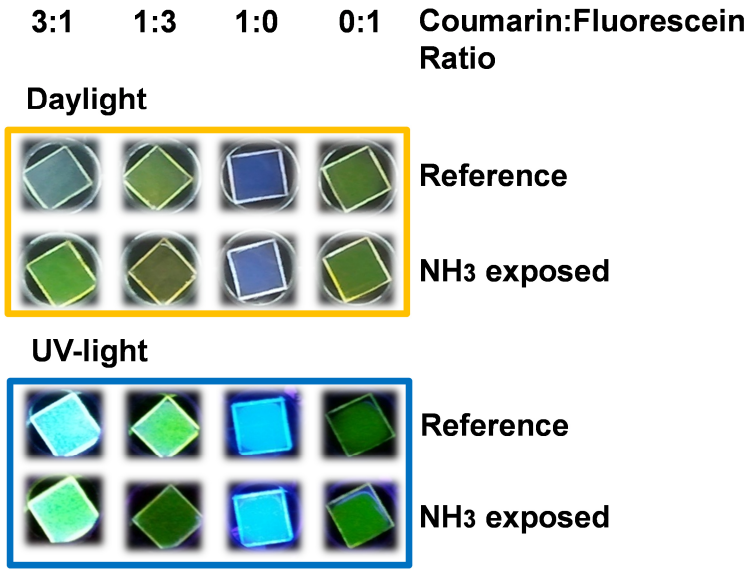

Figure 11: Daylight or UV-light irradiated C and F doped xerogel films on a PMMA substrate changing colour (changing emission wavelength) upon NH_3 exposure.

In order to optimize the response towards ammonia, different coumarin/fluorescein dye ratios were investigated. The decrease of the emission signal at 442 nm upon exposure to ammonia was followed by fluorescence spectroscopy. Figure 12 shows the absolute decrease of the emission signal of different coumarin/fluorescein ratios at 442 nm when exposed to 10,000 ppm ammonia upon excitation at 375 nm. Since fluorescein is not excited at 375 nm, no change in fluorescein emission from 500 to 600 nm due to ammonia exposure was observed in gels containing only fluorescein. Only coumarin doped xerogels showed an intense emission at 442 nm, but the change in emission intensity due to ammonia exposure was relatively low and not quantitative for different ammonia concentrations, even at higher coumarin concentrations. The dye mixtures exhibited different responses to ammonia. At constant coumarin concentration, it is observed that at low fluorescein content an increasing fluorescein concentration has a positive influence on the ammonia sensitivity. However, greater amounts of fluorescein (more than 20 µmol in the initial sol solution) lead to an overall reduced FRET as the spectral overlap becomes too dominant. On the other hand, a higher coumarin concentration did not result in a signal benefit due to self-quenching.

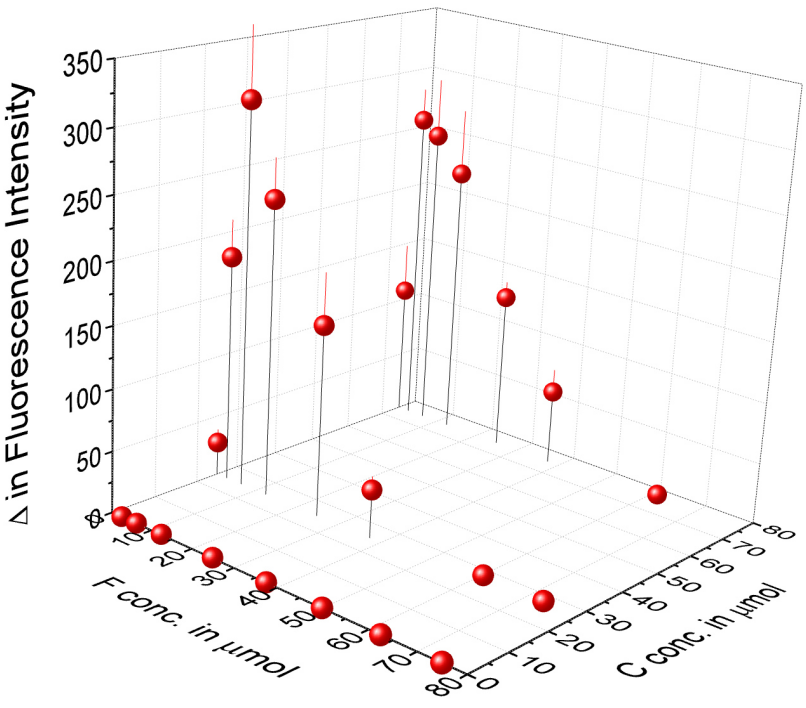

Figure 12: 3D plot illustrating the loss of fluorescence for different C/F ratios upon NH_3 exposure (10,000 ppm). The given concentrations refer to the concentrations in the starting sol solution. The samples were excited at 375 nm, and the emission measured at 442 nm.

The most sensitive xerogel, defined by the largest change in fluorescence emission intensity at 442 nm upon exposure to 10,000 ppm NH_3, resulted from the sol that was composed of 25 µmol coumarin and 6.25 µmol fluorescein. No rational explanation was found for this correlation. From now on, this xerogel is referred as xerogel C/F. Figure 13 shows that the coumarin fluorescence emission of xerogel C/F decreased logarithmically at 442 nm over the entire region from the lowest ppm concentration (40 ppm) to the highest ammonia concentration measured (40,000 ppm).

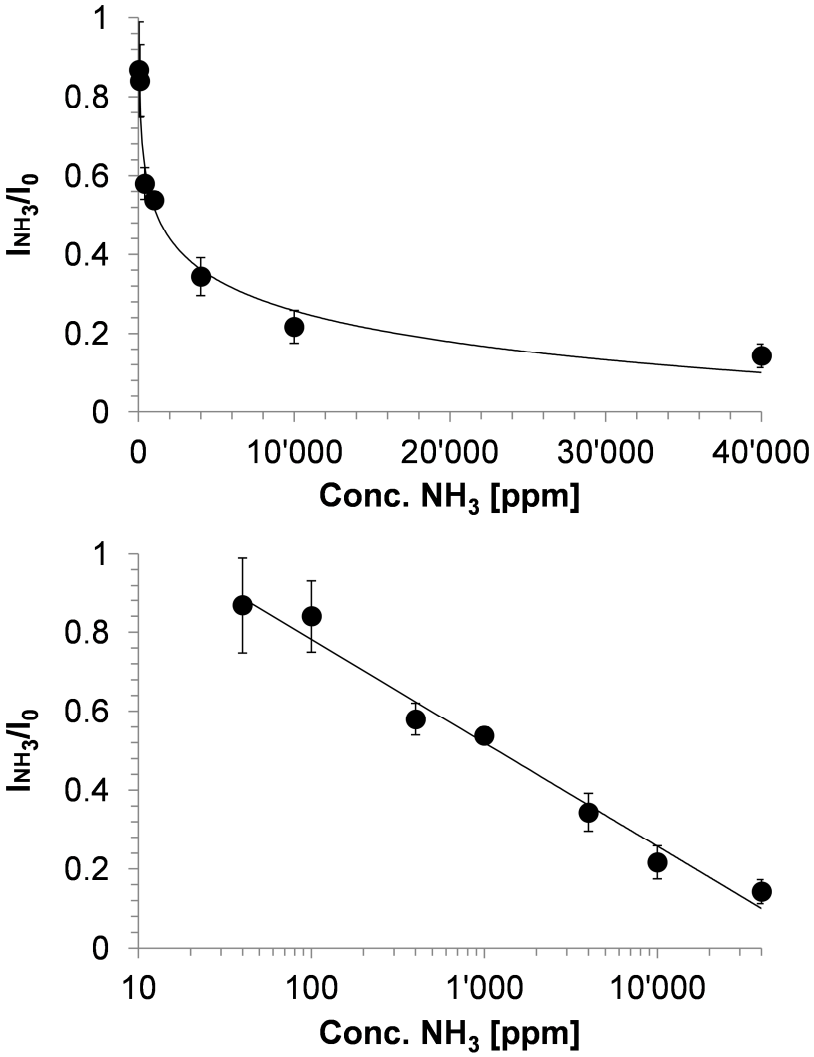

Figure 13: Top: plot showing the loss of fluorescence intensity at 442 nm of the most sensitive xerogel C/F (sol composed of 25 µmol C and 6.25 µmol F) when exposed to different gaseous ammonia concentrations and excited at 375 nm; bottom: semi-log plot showing the linear trend (Econ. $R^2 = 0.98$). I_{NH_3} corresponds to the C emission intensity after NH_3 exposure and I_0 is the reference emission (0 ppm NH_3).

2.3.3 Stability and cross-sensitivity

The fluorescence spectra of the dye-doped xerogel films were measured over 6 months during which no significant change in ammonia sensitivity was observed. Since the sensing films were exposed to not only ammonia vapour but also to water vapour, the influence of water vapour after 30 min (which was the experimental exposure time before measuring the spectra) and 120 min was investigated. Only coumarin doped xerogels responded with a low decrease in fluorescence intensity similar to the previous observation when exposed to ammonia gas (Figure 14). The influence of water vapour on the coumarin fluorescence at 442 nm was neglegible for all coumarin/fluorescein xerogels.

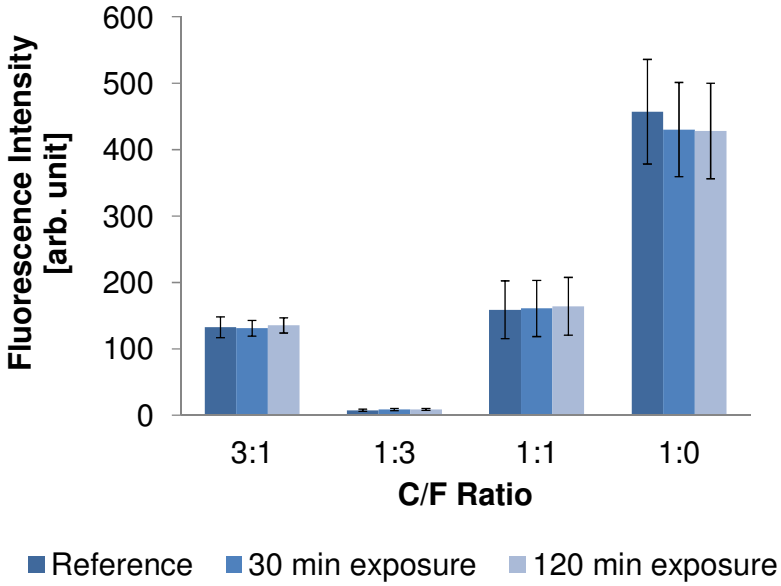

Figure 14: Fluorescence response to water vapour after 30 min and 120 min exposure time at 442 nm. The xerogel films were excited at 375 nm.

Response to HCl

The response of the dye doped xerogel films to HCl is of interest since it would allow an accelerated regeneration of the sensor. The exposure of NH_3 untreated xerogels to HCl gas had no effect on the fluorescence spectra. Furthermore, a kinetic measurement recorded at 442 nm with NH_3 pre-treated xerogels showed no obvious faster regeneration using HCl gas exposure. The regeneration with gaseous HCl was not considered in depth, since the reproducibility with air or heat is more practical in sensor applications and less complex.

Response to $MeNH_2$

Since fluorescein is a universal pH-indicator the response to other amine bases was investigated in order to get an idea on the selectivity of this sensor system. $MeNH_2$ is a colourless gas and has a pK_b value of 3.3[36] which makes it a stronger base than NH_3. Due to its higher deprotonating power, the loss of 85% fluorescence intensity at 442 nm of the xerogel C/F occurred already with 330 ppm $MeNH_2$, whereas the same loss in fluorescence intensity when exposed to NH_3 was observed with 10,000 ppm of NH_3 (Figures 13 and 15).

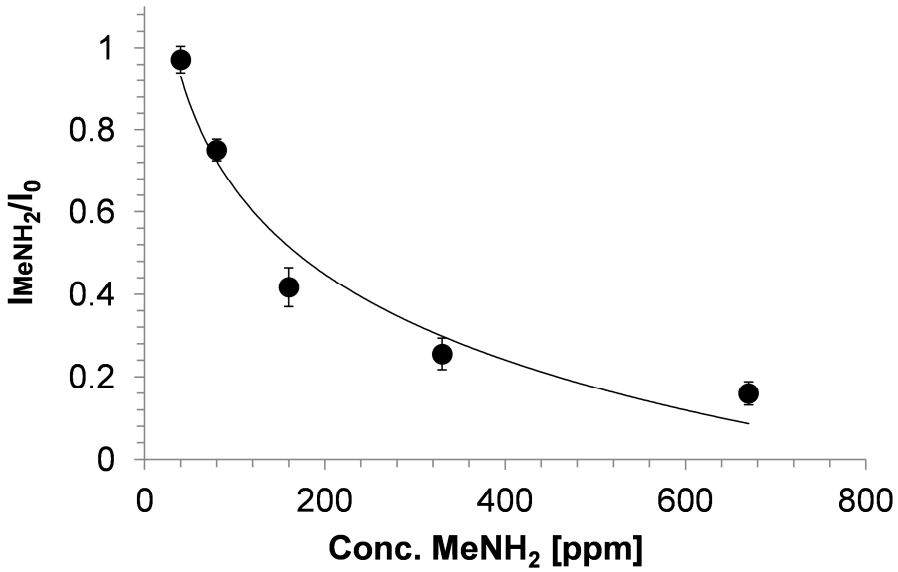

Figure 15: Loss in fluorescence intensity of xerogel C/F when exposed to different concentrations of $MeNH_2$ with an integrated logarithmic trend line (Econ. R^2 = 0.96). I_{MeNH_2} corresponds to the C emission intensity after $MeNH_2$ exposure and I_0 is the reference emission (0 ppm $MeNH_2$).

Response to NEt_3

The response of xerogel C/F to NEt_3, which is a volatile corlourless liquid with a pK_b = 3.25,[39] did not reveal a clear trend which is probably due to the lower critical solution temperature (LCST) of 18.4 °C.[40] NEt_3 molecules cannot form hydrogen bonds with each other but can form N...H–O hydrogen bonds with water molecules. They associate with water molecules with a loss of entropy. The miscibility in all proportions which occurs below the LCST is due not to entropy but to the enthalpy of formation of the hydrogen bonds.[41] Since the measurements were performed at 21 °C, it cannot be excluded that only partial miscibility with water occurred which did not allow to make concentration studies from an aqueous NEt_3 solution.

2.3.4 FRET efficiency

With equation (3) discussed in Section 1.7,[42] the efficiency of the resonance energy transfer of a xerogel containing C and F a in 1:1 ratio was calculated by measuring the fluorescence intensity of the donor (D), in the absence (F_D) and presence (F_{DA}) of the acceptor (A) (Table 1). This evaluation was performed in absence and presence of ammonia to proof the enhanced FRET efficiency due to the enhanced energy transfer.

$$E = 1 - \frac{F_{DA}}{F_D} \quad (3)$$

A fixed distance of the dyes was assumed which postulates a uniform distribution of the dyes in the xerogel.

Table 1: FRET efficiency and Förster distance

NH_3 conc. [ppm]	F_D [arb. unit][a]	F_{DA} [arb. unit][b]	FRET efficiency [%]	R_0 [nm]
0	460 ± 71	159 ± 44	65 ± 15	2.7 ± 0.4
40	408 ± 59	132 ± 34	68 ± 16	2.8 ± 0.4
400	425 ± 62	91 ± 27	79 ± 11	3.0 ± 0.3
1,000	400 ± 58	42 ± 14	90 ± 5	3.5 ± 0.2

[a] F_D: C emission in absence of F (measurement of a xerogel containing C/F in 1:0 ratio) at the corresponding NH_3 measurement). [b] F_{DA}: C emission in presence of F (xerogel containing the dyes in 1:1 ratio) at the corresponding NH_3 concentration. R_0 was calculated with r = 2.4 nm.

The distance of donor C to acceptor F was calculated on the basis of the xerogel film thickness (on the 4.5 × 4.5 × 0.55 mm^3 PMMA substrates) of 12 ± 3 µm, which was determined using profilometry. Knowing the volume of the xerogel film, the average distance between the FRET dye pair was calculated assuming an ideal distribution of the dyes. The distance r between C and F obtained from this calculation was 2.4 ± 0.3 nm. The Förster distance is typically in the range of 2 to 6 nm.[42] The Förster distance R_0, where the FRET efficiency is 50%, was calculated by rearranging equation (2) described in Section 1.7 in equation (6).

$$R_0 = \sqrt[6]{\frac{Er^6}{1-E}} \quad (6)$$

2.3.5 Lifetime measurements

Lifetime measurements were performed in order to get an impression on the applicability of this FRET system for the lifetime sensor technology. The lifetime of C was measured for the xerogel C/F at five different NH_3 concentrations (Table 2).

Table 2: Lifetime of xerogel C/F in presence and absence of NH_3

NH_3 conc. [ppm]	Lifetime τ [ns]	Chi-squared (χ^2)
0	3.61	0.9
100	3.60	1.2
400	3.58	1.1
1,000	3.50	1.1
2,000	3.49	1.2
4,000	3.39	1.1

The lifetimes were shorter the more NH_3 was present which is consistent with the enhanced energy transfer. According to equation (4) in Section 1.7, shorter lifetimes of the donor in presence of the acceptor leads to higher FRET efficiencies.

2.3.6 Gas sensor measurements

The setup

In order to investigate the response behaviour, reproducibility, reversibility and sensitivity of the sol-based optical sensor to ammonia gas in a flow system, experiments were performed using the device shown in Figures 2 and 3. The gas flow was switched between an ammonia/nitrogen mixture and pure nitrogen. When the ammonia gas was introduced for 35 min, the ammonia diffused into the xerogel film where deprotonation of the fluorescein dyes occurred, leading to a decrease in emission intensity at 442 nm. The dyes in the xerogel were excited at 385 nm from the top of the gas sensor (Figure 2). The PMMA substrate acted as a waveguide and the fluorescence intensity was thus monitored at the edge perpendicular to the irradiation. The band pass filter only allowed light of wavelengths between 415–455 nm to pass to the photodetector. Thus, the change in fluorescence from 500–600 nm upon fluorescein

deprotonation-protonation was not monitored. The emission was restored by flushing the system with pure nitrogen for 35 min to remove ammonia.

Ammonia response

Figure 16 shows the sensor response obtained from the online monitoring of the NH_3 response of xerogel C/F films without data processing. An undoped xerogel was measured as a reference and showed no decrease or increase in voltage when exposed to gaseous ammonia. Five observations on the NH_3 response of the xerogel C/F are important:

1) The thicker the xerogel film, the higher the sensor response or the loss in fluorescence intensity respectively
2) The higher the NH_3 concentration, the higher the sensor response
3) The higher the NH_3 concentration, the slower is the response to NH_3
4) The recovery time was generally longer than the response time
5) For all film thicknesses, the first signal always was the most significant

Observation (1) is consistent with the increasing absolute amount of dye immobilized in the films. Observation (2) is in accordance with the results obtained from the fluorescence spectral investigations. If the NH_3 concentration is higher, more fluorescein dianions are formed which leads to an increased spectral overlap and thus to an enhanced energy transfer between the coumarin and fluorescein dyes. As a consequence, the loss in coumarin fluorescence intensity is higher for higher NH_3 concentrations. Observation (3) suggests that the diffusion process of the NH_3 molecules into the sensing film is the response time determining step. The Fick's second law or diffusion equation postulates that the flux of matter is proportional to the concentration gradient.[43] In this case the flux of matter correlates to the migration of the NH_3 gas molecules through the xerogel film. A higher concentration gradient is obtained with higher NH_3 concentrations that should lead to an increase in flux in the same proportion. However, if the flux is smaller than assumed by the concentration gradient, probably caused by the non-porosity of the film, it takes a longer time to reach the gas concentration equilibrium (even distribution, no net flux anymore) in the film. The longer recovery times mentioned in observation (4) can be explained by the fact that the NH_3 molecules were removed only by flushing with the

recovering N_2 gas. It can be noted that it is surprising that this system could be recovered at all, which must be due to very close pK_a of the protonated ammonia and the protonated fluorescein molecules. Three main processes probably contribute to the recovery time: 1) the diffusion of the N_2 gas into the film, 2) the removal of NH_3 from the fluorescein functional groups (protonation) and 3) the complete flushing out of NH_3. According to this approach, the response time with NH_3 is based on two main processes: 1) the diffusion of NH_3 into the film and 2) the fluorescein deprotonation process. The recovery was faster when higher recovery gas flow was applied. Observation (5) leads to the assumption that a certain amount of NH_3 molecules stay irreversibly into the xerogel film and that the first response cycle is needed to achieve a steady state. However, this confirms the diffusion of the ammonia into the film.

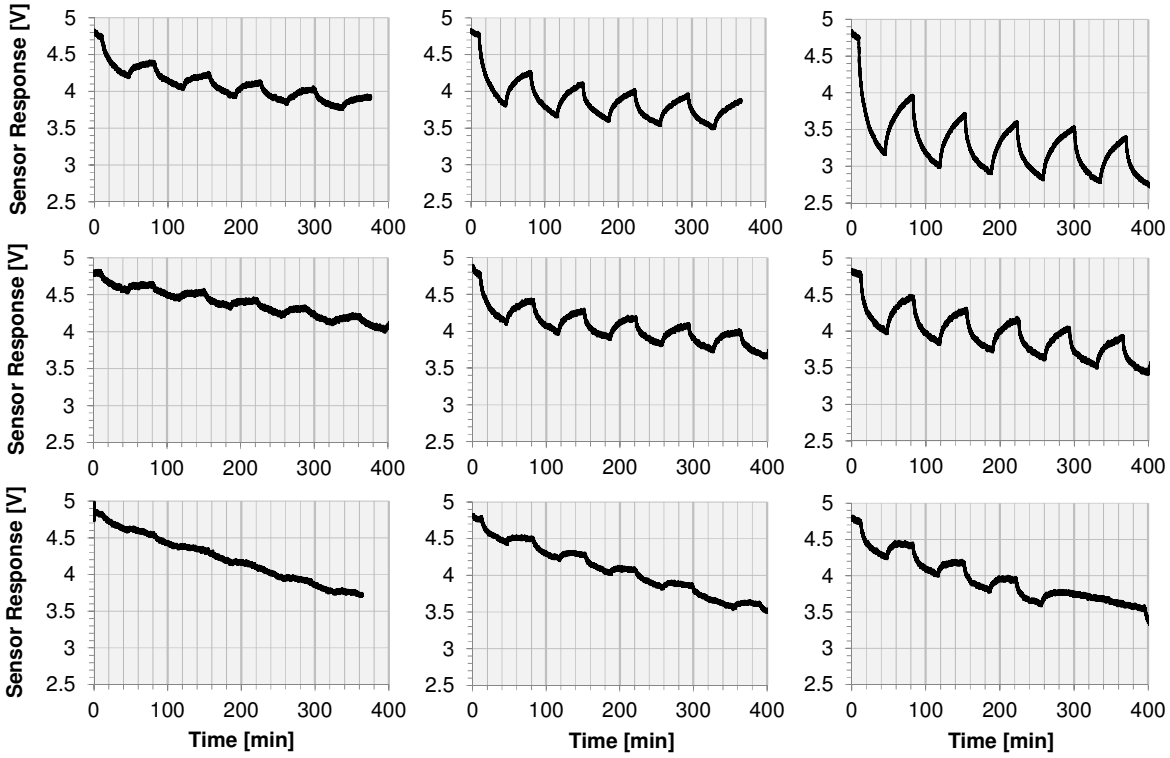

Figure 16: Sensor response of different thick xerogels C/F (13, 9 and 6 µm, from top to bottom) towards 100, 500 and 1,000 ppm NH_3 (from left to right) without baseline correction and data filtering.

Several test measurements (varying temperature of the sensor, dark current measurements, hood ventilation on and off etc.) support the supposition that the sensor drifting is a result of warming up the electronics, the high temperature dependency of the photodiode[44] and a temperature dependency of the xerogel film fluorescence. The fluorescence of fluorescein and coumarin derivatives

have been found to be temperature dependent in solution by exhibiting a shift in emission wavelength or by changing the fluorescence intensity.[45-47] The temperature dependence of fluorescein or coumarin doped xerogels has been less investigated due to the lack of corresponding literature. The permanent LED illumination led to a measurable increase in the temperature inside of the flow cell (from ca. 20 °C to ca. 22.5 °C). After a while, this temperature varied by a small and unpredictable extent (± ca. 0.5 °C) during the measurement. The introduction of a constant N_2 gas flow into the system, this gas being cooler than the inside of the flow cell, probably led to a cooling effect. The simultaneous warming and cooling of the flow cell possibly affect the xerogel film fluorescence and the dark current of the photodiode which is reflected in the continuous downstream drifting of the sensor response. Detailed temperature studies on the xerogel C/F fluorescence intensity were not performed. Furthermore, it is not known to what extent the xerogel film fluorescence and photodiode dark current could account for the downstream drifting. Also a photobleaching process could not be fully excluded. However, if the same measurement was repeated the next day, nearly the same starting fluorescence intensity (sensor response) was achieved which would not be the case if a severe photobleaching occurred.

Figure 17a displays the response behaviour of 13.2 ± 2.9 µm 9.4 ± 1 µm and 6.3 ± 1.1 µm thick xerogel C/F films towards 100 ppm ammonia. The responses shown were baseline corrected. Besides the first cycle, the following cycles have symmetrical reversibility by exhibiting the same loss and recovery in signal intensity in each cycle except for the thickest 13 µm film, where a low continuous decrease in signal intensity was detected. This observation suggests that a certain amount of ammonia remained adsorbed by the xerogel in each cycle even though the system was flushed with N_2 for 35 min, which for the thickest film was not enough. The same trend was observed for this xerogel film with higher ammonia gas concentrations (Figure 16). Figure 17b shows that the rate of recovery time slowed down with time, indicating that the main recovery (removal of largest NH_3 portion) took place during the first half of the recovery process. A measurement to determine the response time was performed for each xerogel thickness with 100 ppm NH_3. The response time (defined as the time required to achieve 95% of the maximum fluorescence signal decrease upon exposure to ammonia[7]) was 18 ± 2 min for the ≈ 6 µm xerogel film, 72 ± 7 min

for the ≈ 9 µm xerogel film and 143 ± 12 min for the ≈ 13 µm xerogel film. This shows that the response time relates linearly to the film thickness. Preliminary studies showed that by using 13 µm xerogel layers 10 ppm ammonia can be detected with this experimental gas sensor setup.

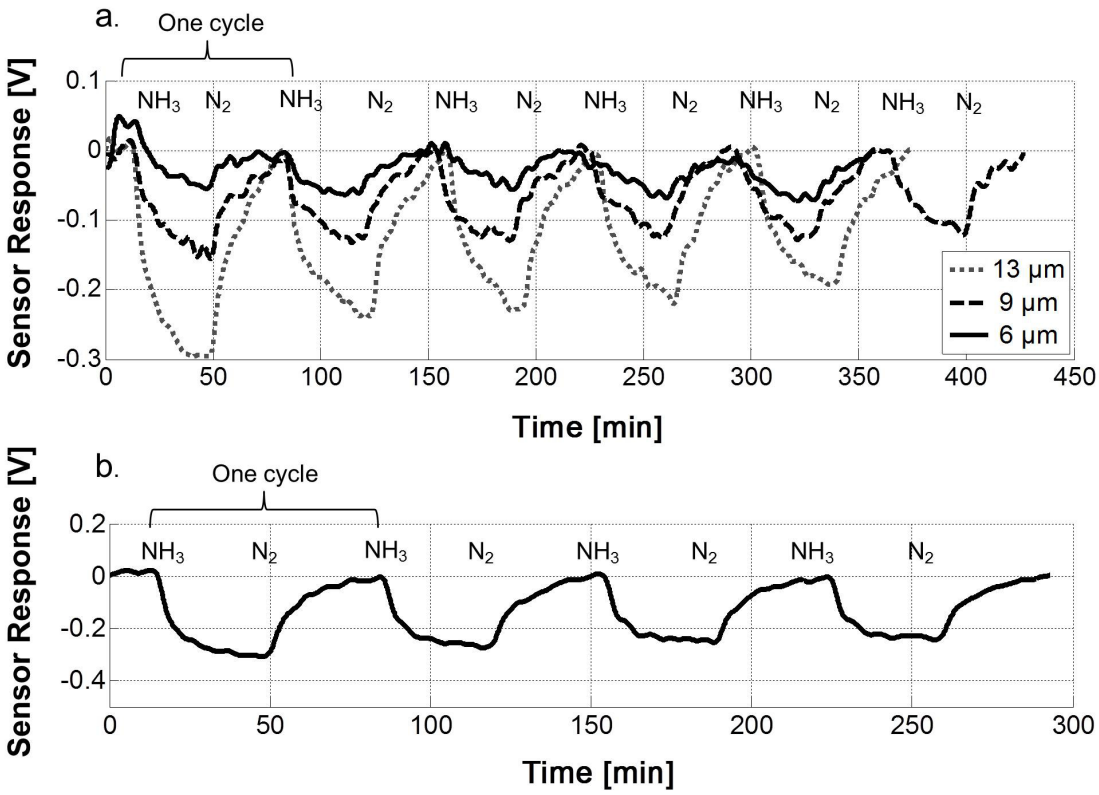

Figure 17: a.: Sensor response and reversibility of the most sensitive (sol composed of 25 µmol coumarin and 6.25 µmol fluorescein) xerogel towards 100 ppm ammonia gas depending on xerogel thickness; b.: response and reversibility of a 6 µm xerogel to 1,000 ppm NH_3 gas.

Humidity response

In order to examine the humidity response of the xerogel C/F, the NH_3-gas-line was removed and replaced by a second N_2-gas-line. In this gas-line, a gas-washing bottle was installed which was filled with the corresponding saturated salt solution to adjust the relative humidity ($MgCl_2$ or NaCl solution) or pure water. Cycle measurements were performed according to the NH_3 measurements to investigate the reproducibility of the responses. In few experiments, the gas washing bottles were exchanged during a measurement to compare the humidity response to lower and higher relative air humidities in the same measurement. From the previous spectral investigation on water vapour response only small humidity responses were expected. The measurements revealed that the signals

from the different relative air humidities were not reproducible during one measurement. A possible explanation for the observed non-reproducibility is the cooling of the whole sensor device through condensation and subsequent vaporization of the water molecules. This assumption is strengthened by two observations: 1) the much faster humidity response and recovery times (e.g. within 3 to 10 min for the ≈ 13 µm xerogel film) in comparison to the NH_3 response times which suggest that the water molecules were not diffusing into the xerogel film and 2) the inverse response that is in accordance with the condensation theory since this process produces heat possibly leading to a change in fluorescence intensity of the xerogel C/F or an increase in dark current of the photodiode.

2.4 Conclusions

The combination of two dyes can help to overcome problems regarding the non-linear response or sensitivity, which occur in sensor systems with only one fluorescent dye. In the presented system, the fluorescein acted as the ammonia trap, while the coumarin's emission signal was used to monitor the change of the ammonia concentration. This was only possible since coumarin and fluorescein form an energy transfer system. The much more pronounced decrease of the signal intensity made the FRET system highly advantageous for the quantitative analysis of a wide range of ammonia gas concentration. The reversibility and practicability of the system was demonstrated with gas sensing experiments. The cross-sensitivity to water cannot be fully excluded since the sensor setup was susceptible to cooling and heating processes. However, the spectral investigation suggests that because of the hydrophobic properties of the sensor film only minimal water vapour responses can be expected. The pK_a values of the dyes determine the dynamic range of the sensor. Dyes with lower pK_a possibly lead to more sensitive sensor coatings. More porous films are aspired for faster ammonia diffusion into the film leading to faster response and recovery times.

2.5 References

1 T. Abel, B. Ungerbock, I. Klimant and T. Mayr, *Chem. Cent. J.*, 2012, DOI:10.1186/1752-153X-6-124.

2 C. Preininger, M. Ludwig and G. J. Mohr, *J. Fluoresc.*, 1998, **8**, 199-205.

3 Q. Chang, J. Sipior, J. R. Lokowicz and G. Rao, *Anal. Biochem.*, 1995, **232**, 92-97.
4 K. Waich, S. Borisov, T. Mayr and I. Klimant, *Sens. Actuators*, *B*, 2009, **139**, 132-138.
5 J. Lei, L. Wang and J. Zhang, *Chem. Commun.*, 2010, **46**, 8445-8447.
6 A. Persad, K.-F. Chow, W. Wang, E. Wang, A. Okafor, N. Jespersen, J. Mann and A. Bocarsly, *Sens. Actuators, B*, 2008, **129**, 359-363.
7 Y. Takagai, Y. Nojiri, T. Takase, W. L. Hinze, M. Butsugan and S. Igarashi, *Analyst*, 2010, **135**, 1417-1425.
8 S. Widmer, M. Dorrestijn, A. Camerlo, S. K. Urek, A. Lobnik, C. E. Housecroft, E. C. Constable and L. J. Scherer, *Analyst*, 2014, **139**, 4335-4342.
9 E. P. Perman, *J. Chem. Soc.*, 1901, **79**, 718-725.
10 E. P. Perman, *J. Chem. Soc.*, 1903, **83**, 1168-1184.
11 W. A. Felsing and B. A. Phillips, *J. Am. Chem. Soc.*, 1936, **58**, 1973-1975.
12 http://www.hofoo.com.cn/uploadfiles/phototransistorired%20data%20-book.pdf, accessed December 2014.
13 G. R. Atkins and R. B. Charters, *J. Sol-Gel Sci. Technol.*, 2003, 26, 919-923.
14 E. M. Rabinovich, in *Sol-Gel Optics: Processing and Applications*, Chapter 1: Sol Gel Processing-General Principles, ed. L. C. Klein, Kluwer, Boston, 1994, p. 7.
15 O. Lev, M. Tsionsky, L. Rabinovich, V. Glezer, S. Sampath, I. Pankratov and J. Gun, *Anal. Chem.*, 1995, **67**, 22A-30A.
16 V. G. Parale, D. B. Mahadik, M. S. Kavale, S. A. Mahadik, A. Venkateswara Rao and S. Mullens, *J. Porous Mater.*, 2013, **20**, 733-739.
17 B. J. Privett, J. Youn, S. A. Hong, J. Lee, J. Han, J. H. Shin and M. H. Schoenfisch, *J. Am. Chem. Soc.*, 2011, **27**, 9597-9601.
18 R. M. Bukowski, R. Ciriminna, M. Pagliaro and F. V. Bright, *Anal. Chem.*, 2005, **77**, 2670-2672.
19 C.-S. Chu and Y.-L. Lo, *Sens. Actuators*, *B*, 2008, **129**, 120-125.
20 C.-S. Chu and Y.-L. Lo, *Sens. Actuators*, *B*, 2007, **124**, 376-382.
21 R. Pardo, M. Zayat and D. Levy, *J. Photochem. Photobiol., A*, 2008, **198**, 232-236.
22 A. Lobnik, I. Oehme, I. Murkovic and O. S. Wolfbeis, *Anal. Chim. Acta*, 1998, **367**, 159-165.
23 A. Lobnik and O. S. Wolfbeis, *Sens. Actuators*, *B*, 1998, **51**, 203-207.
24 X. Chen, L. Lin, P. Li, Y. Dai and X. Wang, *Anal. Chim. Acta*, 2004, **506**, 9-15.

25 H. Kozuka, in *Handbook of Sol-Gel Science and Technology: Processing, Characterization and Applications*, vol. 1, *Sol-Gel Processing*, ed. S. Sakka, Kluwer, Boston, 2005, p. 338.
26 G. Palmisano, E. Le Bourhis, R. Ciriminna, D. Tranchida and M. Pagliaro, *Langmuir*, 2006, **22**, 11158-11162.
27 M. Pagliaro, G. Palmisano, E. Le Bourhis, R. Ciriminna, L. M. Ilharco and A. Fidalgo, *J. Nanomater.*, 2008, **2008**, Article ID 964046
28 J. D. Mackenzie, Q. Huang and T. Iwamoto, *J. Sol-Gel Sci. Technol.*, 1996, **7**, 151-161.
29 K. Tadanaga and T. Minami, in *Handbook of sol-gel science and technology: Processing, Characterization, and Applications*, vol. 2, *Characterization and properties of sol-gel materials and products*, ed. S. Sakka, Kluwer, Boston, 2005, pp. 204-208.
30 R. M. Almeida, in *Handbook of Sol-Gel Science and Technology: Processing, Characterization and Applications*, vol. 2, *Characterization and properties of sol-gel materials and products*, ed. S. Sakka, Kluwer, Boston, 2005, pp. 68-77.
31 D. Wencel, M. Barczak, P. Borowski and C. McDonagh, *J. Mater. Chem.*, 2012, **22**, 11720-11729.
32 L. Peng, X. Yang, L. Yuan, L. Wang, E. Zhao, F. Tian and Y. Liu, *Opt. Commun.*, 2011, **284**, 4810-4814.
33 R. Sjöback, J. Nygren and M. Kubista, *Spectrochim. Acta, Part A,* 1995, **51**, L7-L21.
34 M. M. Martin and L. Lindqvist, *J. Lumin.*, 1975, **10**, 381-390.
35 H. Leonhardt, L. Gordon and R. Livingston, *J. Phys. Chem.*, 1971, **75**, 245-249.
36 K. W. Whitten, R. E. Davis, M. Larry Peck and G. G. Stanley, in *Chemistry*, Chapter 18: Ionic Equlibria I: Acids and Bases, Thomson, Belmont, 8th edn., 2007, p. 720.
37 R. M. Clegg, in *Laboratory Techniques in Biochemistry and Molecular Biology*, vol. 33, *FRET and FLIM Techniques*, ed. T. W. J. Gadella, Elsevier, Burlington, 2009, pp. 1-57.
38 K. H. Drexhage, in *Topics in Applied Physics*, vol. 1, *Laser Dyes*, ed. F. P. Schäfer, Springer, New York, 1973, pp. 161-163.
39 http://pubchem.ncbi.nlm.nih.gov/compound/triethylamine#section=Ionicity, accessed June 2015.
40 W. J. Green, *J. Chem. Eng. Data*, 1979, **24**, 92-93.
41 https://en.wikipedia.org/wiki/Lower_critical_solution_temperature, accessed June 2015.

42 J. R. Lakowicz, in *Principles of Fluorescence Spectroscopy*, Chapter 13: Energy Transfer, Springer, New York, 3rd edn., 2010, pp. 443-453.
43 P. Atkins and J. de Paula, in *Atkins' Physical Chemistry*, Chapter 21: Molecules in Motion, Oxford, New York, 8th edn., 2006, pp. 757-780.
44 http://www.osioptoelectronics.com/application-notes/AN-Photodiode-Parameters-Characteristics.pdf, accessed April 2015.
45 J. Coppeta and C. Rogers, *Experiments in Fluids*, 1998, **25**, 1-15.
46 K. Dobek, *J. Fluoresc.*, 2011, **21**, 1547-1557.
47 B. G. Evale, *Indian J. appl. Res.*, 2014, **4**, 9-12.

Chapter 3

Incorporation of a FRET Dye Pair into Mesoporous Materials: A Comparison of Fluorescence Spectra, FRET Activity and Dye Accessibility

3.1 Introduction

Chapter 2 concluded that optimizations regarding the issues of sensitivity, response and recovery have to be performed. Furthermore, a FRET system with a positive response to ammonia was anticipated. A gain in fluorescence intensity is a clear sign that ammonia is present in the environment whereas a loss in fluorescence intensity can be due to other effects such as photobleaching, cooling (drifting) and the presence of dust particles. This chapter deals with the incorporation of silica particles into the xerogel coating in order to improve the porosity of the final film which ideally leads to faster response and recovery times of the sensor. Different dye combinations on MCM-41 (Mobile Composition of Maters No. 41) were studied aspiring to a gain in fluorescence intensity upon NH_3 exposure. This preliminary study revealed the fluorescein/rhodamine B FRET dye pair to be best suited for the aimed optical sensor application. In a further and profounder study, fluorescein and rhodamine B modified mesoporous SBA-15 (Santa Barbara Amorphous No. 15) silica particles were synthesized by post-grafting and co-condensation approaches. The materials were characterized by nitrogen sorption, scanning electron microscopy and fluorescence spectroscopy. The Förster resonance energy transfer between the selected dye pair was explored for the different materials by exposure to various concentrations of gaseous ammonia. The dye accessibility by ammonia gas in the silica framework of mesoporous materials was evaluated by using the same flow cell gas sensor setup. Response to ammonia gas and recovery with nitrogen gas are explained by comparing the structure properties and dye loading of the materials. Most of the content of this chapter was published in Analyst in 2015.[1]

3.2 Experimental

3.2.1 Labelling of MCM-41

Functionalization with 3-aminopropyltriethoxysilane (APTES). MCM-41 particles were provided by the Brühwiler group from the University of applied sciences in Wädenswil (CH) and were functionalized according to the literature.[2] The glassware was dried before the experiment (16 h, 90 °C). Calcined predried (16 h, 80 °C) MCM-41 particles (100 mg) were dispersed in dry toluene (5 mL; AcrosOrganics, 99.85%, < 0.003% H_2O) and APTES (10 µmol; Aldrich) was added. After the reaction mixture has been stirred for 10 min under N_2 at room temperature (RT), the functionalized mesoporous silica was recovered by centrifugation (7,000 rpm for 5 min). The supernatant liquid was decanted and the residual pellet was re-dispersed in toluene and centrifuged 3 times. The powder (MCM-APTES) was cured in an oven at 80 °C for 16 h.

Labelling of MCM-APTES. Labelling with dyes (all purchased from Aldrich and used without further purification) was performed following a literature method[3] by dispersing MCM-APTES in dry ethanol (AcrosOrganics, 99.5%, < 0.005% H_2O) and vigorous stirring for 5 h under N_2 at RT. 1-Ethyl-3-(3-dimethylaminopropyl)-carbodiimide hydrochloride (Aldrich) was added in 1.5-fold excess if a dye with a carboxylic acid functional group was involved. The amounts of the different reaction components used for the syntheses are given in Table 1. The dye denominations and excitation as well as main emission wavelengths when the dye modified MCMs were immobilized into a xerogel are shown in Table 2.

Table 1: Synthesis conditions for the dye-labelling of MCM-41

Sample	Dyes	Dye concentration [µmol]	MCM-APTES [mg]	Ethanol [mL]	
MCM-F	F	8	80	8	Single dyes
MCM-DCF	F_{Cl}	8	80	8	
MCM-EoY	EoY	10	100	10	
MCM-C_{CA}	C_{CA}	8	80	8	
MCM-C_{AcH}	C_{AcH}	8	80	8	
MCM-R	R	5	50	5	
MCM-Tr	Tr	2	20	2	
MCM-FC_{CA}	F	4	80	8	FRET dye pair F main sensing species
	C_{CA}	4			
MCM-FC_{AcH}	F	4	80	8	
	C_{AcH}	4			
MCM-F/R	F	2.5	50	5	
	R	2.5			
MCM-FTr	F	2	40	4	
	Tr	2			
MCM-DCFC_{CA}	F_{Cl}	2.5	50	5	FRET dye pair DCF main sensing species
	C_{CA}	2.5			
MCM-DCFC_{AcH}	F_{Cl}	2.5	50	5	
	C_{AcH}	2.5			
MCM-DCF/R	F_{Cl}	2.5	50	5	
	R	2.5			
MCM-DCFTr	F_{Cl}	2.5	50	5	
	Tr	2.5			
MCM-EoYR	EoY	5	100	10	FRET dye pair EoY main sensing species
	R	5			
MCM-EoYTr	EoY	2	40	4	
	Tr	2			

Table 2: Dye abbreviations used throughout this chapter

Dye abbreviation	Dye	Ex [nm][a]	Em [nm][b]
F or FITC[c]	Fluorescein-5-isothiocyanate isomer I	482	516
DCF	2',7'-Dichlorofluorescein	514	533
EoY	Eosin-5-isothiocyanate	535	557
C_{CA}	7-(Diethylamino)coumarin-3-carboxylic acid	424	464
C_{AcH}	7-Amino-4-methyl-3-coumarinylacetic acid	347	428
R or RBITC[c]	Rhodamine B isothiocyanate	553	579
Tr	Sulforhodamine 101 acid chloride (Texas red)	582	617

[a]Excitation wavelength of the dye grafted on the MCM-41. The labelled particles were immobilized into an unlabelled xerogel film on PMMA. [b]Main emission wavelength. [c]Fluorescein isothiocyanate is abbreviated F if grafted on the silica particles and FITC if immobilized in the xerogel. The same is applied for rhodamine B isothiocyanate.

3.2.2 Synthesis of fluorescein and rhodamine labelled SBA-15

Synthesis of SBA-15 particles (SBAs). Spherical SBAs were synthesized according to the literature[3-5] by adding a solution of hexadecyltrimethyl-ammonium bromide (0.465 g; Fluka) in deionized H_2O (20 mL) to a solution of Pluronic P123 (3.10 g; $EO_{20}PO_{70}EO_{20}$, M_{av} = 5,800, Aldrich) in 1.5 M aq. HCl (50 mL; Aldrich). After the addition of ethanol (7.8 mL; Aldrich), the mixture was stirred vigorously and tetraethoxysilane (10 mL; TEOS, Fluka) was added dropwise. After stirring for 2 h at RT, the mixture was transferred to a Teflon-lined autoclave and kept at 78 °C for 72 h. The product was collected by filtration, washed with deionized H_2O (50 mL), and dried at RT. Calcination was performed at 500 °C for 16 h with a heating rate of 1.2 °C min^{-1}.

Functionalization with 3-aminopropyltriethoxysilane (APTES). Amino-functionalization of SBA was carried out following a method similar to that reported in literature.[3] The mesoporous silica (400 mg) was dispersed in dry toluene (20 mL; AcrosOrganics, 99.85%, < 0.003% H_2O) and APTES (40 µmol; Aldrich) was added under N_2. For smaller batches 100 mg of SBA was dispersed in 5 mL of dry toluene and APTES (10, 20 or 40 µmol respectively) was added under N_2. After vigorous stirring under N_2 for 10 min, the dispersion was transferred to centrifuge tubes and centrifuged at 7,000 rpm for 5 min. The supernatant liquid was decanted and the residual pellet was re-dispersed in toluene and centrifuged 3 times. The amino-functionalized silicas, SBA-NH_2 1–4, were cured at 70 °C for 16 h. SBA-NH_2 1 corresponds to the amino-functionalized SBA obtained from the larger batch. SBA-NH_2 2–4 correspond to the 100 mg batches functionalized with 10 (SBA-NH_2 2), 20 (SBA-NH_2 3) or 40 µmol (SBA-NH_2 4) APTES respectively.

Labelling by the post-grafting (PG) method. Fluorescein-5-isothiocyanate (FITC isomer I, Aldrich) and rhodamine B isothiocyanate (RBITC, Aldrich) were coupled to amino-functionalized mesoporous silica (SBA-NH_2 1–4) following a literature[3] method by dispersing amino-functionalized silica (100 mg) in dry ethanol (5 mL; AcrosOrganics, 99.5%, < 0.005% H_2O) under N_2. An equal amount of ethanol was used to dissolve the corresponding dyes (total 10, 20 or 40 µmol respectively, for dye pairs half amount of each). The dye solution was added to the silica dispersion. After stirring for 5 h at RT under N_2, the

dispersion was transferred to centrifuge tubes and centrifuged at 7,000 rpm for 7 min. The supernatant liquid was decanted and the pellet re-dispersed in ethanol and centrifuged 10 times. The dye modified mesoporous silica, PG SBA F/R 1–4 and PG SBA F or R 1, was dried at 70 °C for 1 h. The numbers correspond to the initial SBA-NH_2 and were also used for the dye labelling products.

Synthesis of fluorescein/rhodamine labelled SBA by co-condensation. Co-condensed fluorescein and rhodamine modified SBA-15 particles were synthesized using procedures from references 4, 6 and 7 with minor optimization. FITC and RBITC were coupled to APTES by dissolving the dyes separately in ethanol. After addition of APTES to each dye solution, the mixture was stirred in the dark for 24 h. The amounts used for the coupling of APTES with the dye are shown in Table 3.

Table 3: Dye-APTES solutions prepared for the synthesis

Sample	FITC/RBITC [µmol]	APTES [mL]	EtOH [mL]
CoCo SBA F/R HD[a]	19/20	0.01	1
CoCo SBA F/R LD[a]	19/20	1	10

[a]Sample denomination: CoCo: co-condensed; SBA: mesoporous material; F: fluorescein; R: rhodamine; HD: high dye loading; LD: low dye loading

P123 and KCl (Fluka) were dissolved in deionized H_2O and HCl (32%; Aldrich). Then 1,3,5-trimethylbenzene (TMB, Aldrich) was added. After stirring for 2 h in ethanol, TEOS (Fluka) and the corresponding amount of APTES-dye in ethanol were added. The amounts of the different reaction components used for the syntheses are given in Table 4. The mixtures were stirred for 30 min before being transferred to a Teflon-lined autoclave and kept at 60 °C for 4 h. The products were collected by filtration, washed with deionized H_2O (50 mL), and dried at 120 °C for 20 min. The structure directing agent was removed by Soxhlet extraction in ethanol and co-condensed mesoporous materials, CoCo SBA F/R HD or LD, were obtained.

Table 4: Synthesis conditions for the synthesis of FITC/RBITC labelled co-condensed SBA

Sample	P123 [g]	KCl [g]	H_2O [mL]	HCl [g]	TMB [g]	TEOS [mL]	APTES-dye [µL]
CoCo SBA F/R HD	0.5	0.76	15	3.0	0.38	1.1	150
CoCo SBA F/R LD	1.0	1.5	30	5.9	0.76	2.3	250

3.2.3 Thin film preparation

General sol preparation. The sol preparation was performed according to Section 2.2.2 and reference 8. FITC/RBITC sols were prepared by dissolving the desired amount (2.5, 10, 20 µmol) of the dye in 5 mL of ethanol (Fluka). After sonication (UltrasonicCleaner from VWR, 45 kHz, 80 W) of the solution for 10 min at RT, methyltriethoxysilane (1.793 mL; Aldrich) and 3,3,3-trifluoropropyltrimethoxysilane (0.576 mL; Aldrich) were added. After a further 10 min of sonication, 0.1 M HCl (0.08 mL; Aldrich) and deionized H_2O (80 µL) was added to the solution. The sol was sonicated for another 20 min and aged for 24 h at RT. Sols without dyes (unlabelled) used for the immobilization of the particles were prepared the same way.

Xerogel film preparation for fluorescence measurements. 5 µL of the sol solution was solvent cast on PMMA substrates (4.5 × 4.5 × 0.5 mm^3; foil from microfluidic ChipShop) and dried in an oven at 70 °C for 12 days. Particles were immobilized in the xerogel coating by dispersing 1 mg of the corresponding MCM or SBA material in 80 µL of aged unlabelled sol solution. The solvent-casting procedure was the same for these sols as for sols without particles. Particle coatings were dried at 70 °C for 2 days.

Xerogel film preparation for gas sensor measurements. 20 µL of aged sol were solvent cast on cut PMMA substrates (1.5 × 1.5 × 0.1 cm^3; microscope slides from microfluidic ChipShop) and dried in an oven at 70 °C for 12 days. Particles were immobilized in the xerogel coating by dispersing 1.5 mg of the corresponding SBA material in 50 µL of aged unlabelled sol solution. The solvent-casting procedure was the same for these sols as for sols without particles. Particle coatings were dried at 70 °C for 2 days.

3.2.4 Characterization methods

Fluorescence measurements. Fluorescence measurements were performed according to Section 2.2.4 and reference 8. Fluorescence spectra were recorded in the range of 495–700 nm on a Biorad Fluorescence spectrophotometer. The small xerogel-coated PMMA plates were horizontally pinched into the wells of a microtitre wellplate at the same height. The plates were exposed to NH_3 gas by adding 20 µL of the desired aqueous NH_3 solutions to the well bottom by microsyringe. The well plate was then covered by a lid and wrapped with Parafilm. Before each fluorescence measurement, the loaded well plate was stored in a conditioned room (21 °C, 50% rel. air humidity) for 30 min to ensure the same measurement conditions. The NH_3 vapour concentrations within the wells were calculated based on the partial pressure of NH_3.[9,10] To compensate possible humidity response, the coatings were exposed three times to H_2O vapour by adding 20 µL of H_2O to the well bottom by a microsyringe. The average of the observed intensities was taken as the reference intensity for the NH_3 experiments.

Determination of dye content in SBAs. The amount of coupled FITC and RBITC was determined by dissolving the sample (usually 1–4 mg) in 0.2 M aq. NaOH and measuring the UV-visible spectra of the resulting clear solution on a Biotek spectrophotometer. The molar extinction coefficients for FITC (ε = 76,000 M^{-1} cm^{-1}) and RBITC (ε = 37,700 M^{-1} cm^{-1}) in 0.2 M NaOH were obtained with a standard deviation of 6% from four stock solutions prepared as follows: (1) FITC and RBITC were stirred separately in 0.2 M NaOH until complete dissolution. (2) FITC and RBITC were combined in a molar ratio of 1:1 in 0.2 M NaOH and stirred until complete dissolution. (3) FITC and RBITC were stirred separately in ethanol until complete dissolution. A corresponding amount of APTES was added and the reaction mixture was stirred for 16 h. After evaporation of the solvent, the residue was dissolved in 0.2 M NaOH. (4) FITC and RBITC were combined in a molar ratio of 1:1 in ethanol until complete dissolution. Subsequent treatment was as with (3). The addition of mesoporous silica to the dilution series showed no significant effect on the extinction coefficient.

Scanning electron microscopy (SEM). Cuts were obtained by solvent casting the sols on a silicon wafer and drying for 12 days. The wafer was broken in the middle over a sharp edge. The samples were Au/Pd sputtered with a device from Leica. The images were recorded on a Hitachi S4000 instrument.

Confocal laser scanning microscopy (CLSM). CLSM images were taken with an Olympus BX 60 microscope equipped with a FluoView detector. Optical slices of the center of the particles were obtained by exciting with lasers operating at 488 and 543.5 nm.

Optical microscopy. The images were recorded on the coatings prepared for the gas sensor measurements using an optical microscope from Keyence.

Porosity measurements. Nitrogen adsorption isotherms were measured at -196 °C using a NOVA 3000e Surface Area and Pore Size Analyzer (Quantachrome). Prior to measurement, the samples were vacuum degassed at 80 °C for 3 h. Pore size distributions (PSD) and total surface area (S_{BET}) were calculated from the NLDFT[11] and the BET[12] methods. External surface area (S_{ext}) was determined by the α_s method.[13] Total pore volume (V_{tot}) was calculated at a relative pressure of 0.95. The adsorption isotherm was used for all calculations.

Gaussian evaluation. The Gaussian evaluations were performed with the Origin software version 9.

Lifetime measurements. Lifetime measurements were performed on a Quantaurus-Tau compact fluorescence lifetime spectrometer from Hamamatsu. The xerogels were excited at 470 nm and the fluorescence emission was recorded at 520 nm. The xerogel film on PMMA was exposed for 20 min to NH_3 (100, 400, and 1,000 ppm) outside of the instrument in a closable plastic box and were then rapidly deposited in the device for the lifetime measurement. The lifetime was obtained by first order fitting of the fluorescence decay curve. The chi-square test was performed automatically by the appropriate software.

3.2.5 Gas sensor measurements

Laboratory set-up for testing the ammonia sensing probes. The gas sensor measurements were performed with an in-house built flow cell gas sensor illustrated in Section 2.2.5.[8] The plates were illuminated from the top (pulsed excitation, 10 Hz) by a 0.7 W LED of peak wavelength 470 nm (FWHM bandwidth 25 nm) purchased from Thorlabs. To measure fluorescence emission, the photodetector was placed orthogonal to the incoming radiation, therefore the PMMA sample plate acted as a waveguide of the emitted light to the detector. Additionally, an optical longpass filter was placed in front of the detector, which only allowed passage of light above 550 nm (FEL0550; Thorlabs) (Figure 1). The inside of the flow cell was painted black to reduce reflections of the direct light. Electronic readout was based on a phototransistor circuit and a LabView-controlled digital multimeter. The gas flow could be switched between the NH_3/N_2 mixture and N_2 using manual valves. During the experiments, the flow rate (800 mL ± 50 mL/min), the temperature (20 ± 2 °C), and the humidity (< 4%) were monitored in the line using a CMOSens EM1 (Sensirion) and an MSR 145 (Sensirion) respectively. Custom mixed gases 49.7 ppm ± 2% rel. NH_3, 99.6 ppm ± 2% rel. NH_3, 504.9 ppm ± 2% rel. NH_3, 0.101 ± 1% rel. NH_3 in N_2 (≥ 99.8%) and pure N_2 gas were acquired from Carbogas.

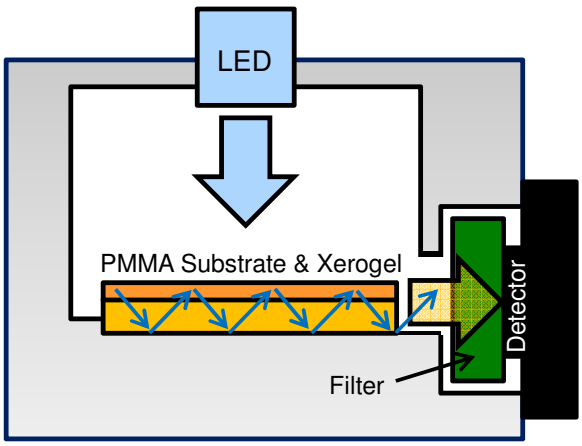

Figure 1: Schematic of the gas sensor box, where the coated PMMA substrate is deposited.

Measurement and measurement evaluation. Before each measurement, the system was flushed with N_2 gas for 5 min. An experiment always started with a 300–600 s N_2 gas flush followed by a flush with an NH_3 gas mixture. The amplification of the electronic and the LED light intensity was constant for each measurement. Raw data from the one cycle measurements were plotted in

Microsoft Excel. During the evaluation in Excel, the baselines (light/fluorescence intensity at the beginning of the measurement (0 ppm NH_3)) were set to the same value (0). This means that the signals obtained from different coatings cannot be directly compared beyond each other (each coating had a different starting light intensity or voltage respectively) since the gain in fluorescence intensity is always relative to the starting fluorescence intensity where the NH_3 concentration is 0 ppm. The thermal drift of the cycle measurement of PG SBA F/R 1 was corrected by fitting a double polynomial equation to the turning point of each cycle (valley, lowest point of N_2 recovery). The signal noise was reduced by using a fifth order Butterworth low-pass filter with 5 mHz cut-off frequency.

3.3 Results and Discussion

3.3.1 Ammonia response of dye-labelled MCM-41

Possible approaches for the dye modification of MCM-41 particles and xerogel, in which the particles were immobilized, are shown in Figure 2: 1) the FRET dye pair is grafted on the same particle and the particles finally are immobilized into an unlabelled xerogel; 2) the particles are modified separately with the acceptor and donor dye and finally immobilized together into an unlabelled xerogel; and 3) The particles are modified with the acceptor dye and the xerogel is doped with the donor dye or *vice versa*. It turned out that only approach (1) worked properly. The problem with approach (2) relied on the donor-acceptor distance being too high as a consequence on being attached on separate particles. The integration of a higher amount of particles into the sensing film did not lead to better results. Furthermore, the immobilization of a high amount of particles led to a non-transparent sensor film, which was not suitable for the final optical sensor application. Approach (3) yielded no information regarding the resonance energy transfer since only the much stronger fluorescence of the dye immobilized into the xerogel was detected. FRET between the dyes could only occur at the boundary surface where the particle is in direct contact with the xerogel.

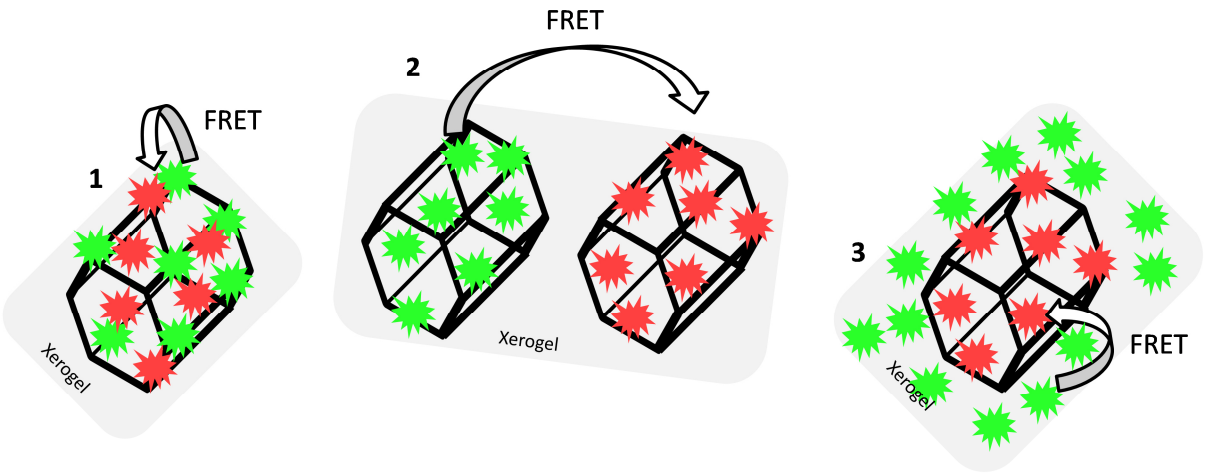

Figure 2: Different possibilities of dye-labelling the MCM-41 particles.

F, DCF and EoY modified MCM-41 responded to NH_3 with an increase in fluorescence emission intensity which is due to the deprotonation of the pH-sensitive dyes. The amount of increase of fluorescence intensity was expected to be dependent on the pK_a value of the corresponding dye being lowest for EoY (p$K_{dianionic}$ = 3.8)[14] followed by DCF (p$K_{dianionic}$ = 4.95)[15] and F (p$K_{dianionic}$ = 6.6)[16] (pK_a values of dyes were measured in aqueous solution). The dependence on pK_a was manifested by the response maxima (biggest fluorescence intensity change) being reached at lower NH_3 concentration for EoY, followed by DCF and F. Therefore, these fluorescein derivatives are promising NH_3 indicators in a certain concentration range. The dyes were combined with the possible FRET partners such as R and Tr. Only the FRET dye pair F/R showed an increase in the acceptor emission due to an enhanced energy transfer upon NH_3 (Table 5).

Table 5: The FRET systems and response behaviours

Donor (D)	Acceptor (A)	Ex [nm]	Em[a] [nm]	NH_3 indicating dye[b]	Response [pos./neg.][c]	Sensitivity [ppm]	Logarithmic response
C_{CA}	F	424	464	D	neg.	0–1,000	Yes
C_{AcH}	F	347	428	D	neg.	0–1,000	Yes
F	R	482	584	A	pos.	0–7,000	Yes
F	Tr	482	624	A	neg.	0–1,000	Yes
F_{Cl}	R	514	592	A	neg.	-	No
F_{Cl}	Tr	514	625	A	neg.	-	No
EoY	R	535	572	A	neg.	-	No
EoY	Tr	535	618	A	neg.	-	No

[a]Main emission wavelength. [b]The NH_3 indicating dye means the dye which emission is measured for the NH_3 monitoring. [c]Negative response: loss in fluorescence intensity of the NH_3 indicating dye; positive response: gain in fluorescence intensity of the NH_3 indicating dye.

To relate to the investigated coumarin/fluorescein FRET system in the xerogel (Chapter 2), F was combined with C_{CA} and C_{AcH}. A logarithmic loss in fluorescence intensity was observed and is in accordance with the results from Chapter 2. No further studies were performed in order to investigate the reason for the loss in fluorescence intensity for the other FRET systems.

3.3.2 Comparison in structure properties of SBAs

The morphology of the SBAs was examined using SEM (Figure 3). Purely siliceous SBA particles were spherical (Figure 3c) with a diameter in the range of 4–2 µm. The relatively narrow PSD is typical for SBA that has a small tail extending in to the microporous range (Figure 4).[17] The average pore size was 6 nm (Table 6). Labelling did not influence the morphology of the SBA (Figure 3d). The CoCo SBA F/R LD, synthesized with low APTES-dye concentrations, produced well-shaped spherical particles with similar diameters between 2 and 4 µm (Figure 3b). However, CoCo SBA F/R LD showed a broad PSD with a width at half maximum of about 9 nm and a pore size of about 10 nm (Figure 4). The increase and broadening in pore size results from the increased concentration of organics in the mother liquid. These organic molecules dissolve in the organic phase inside of the structure-directing agent leading to an expansion of the micelles. CoCo SBA F/R HD particles were irregular (Figure 3a). The PSD is also very broad and undefined, indicative of a poor long range ordering of the material. High concentrations of organics in the synthesis mixture, in this case TMB and higher amount APTES-dye, have a large effect on the particle morphology and PSD.[18] The initial material for all post-grafted materials was SBA with a pore size of around 6 nm (Table 6). The amount of grafted organic moieties increased from samples SBA-NH_2 1–4 to PG SBA F/R 1–4, but the pore sizes showed negligible changes, since the introduced amount of dye is in the nanomolar range per mg of silica and the distribution of the grafted APTES molecules is non-uniform.[19,20] The extent of organic modification is possibly too low for an unambiguous effect on the pore size, but sufficient enough to affect the pore volumes and BET surface areas, which show a decreasing trend with increasing amount of grafted molecules (Table 6).

Table 6: Properties of investigated SBA materials

Sample	d_{NLDFT} [nm][a]	S_{BET} [m^2/g]	V_{tot} [cm^3/g]
CoCo SBA F/R HD	7	228	0.39
CoCo SBA F/R LD	10	215	0.47
SBA-15	6	801	0.79
SBA-NH_2 1	6	755	0.79
SBA-NH_2 2	6	587	0.70
SBA-NH_2 3	6	505	0.61
SBA-NH_2 4	6	436	0.56
PG SBA F/R 1	6	753	0.77
PG SBA F/R 2	6	515	0.59
PG SBA F/R 3	6	329	0.42
PG SBA F/R 4	6	292	0.35

[a]Average pore diameter of the mesopores

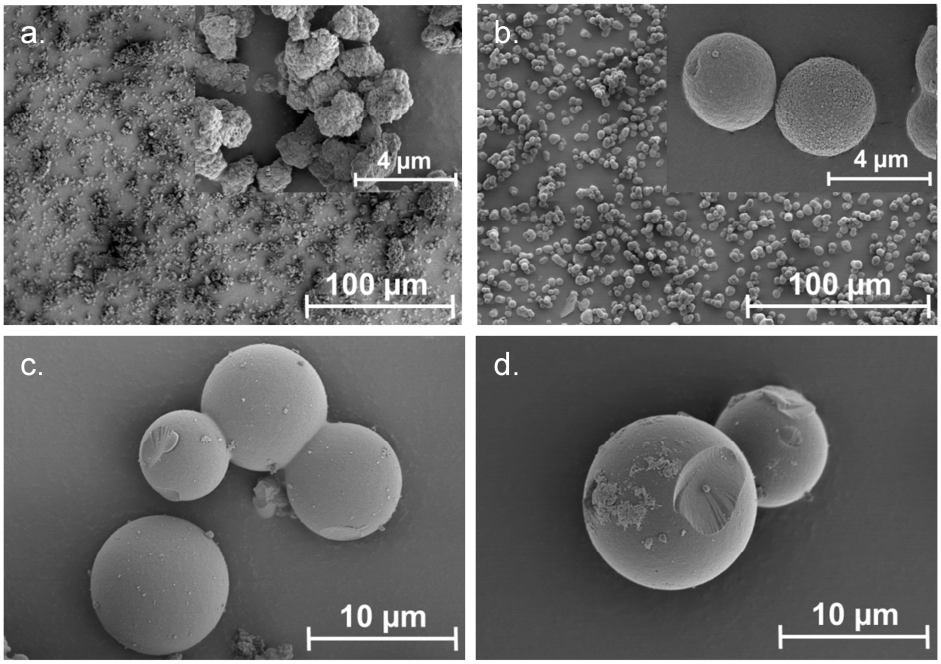

Figure 3: SEM illustrations of synthesized particles: a.: CoCo SBA F/R HD, b.: CoCo SBA F/R LD, c.: SBA, d.: PG SBA F/R 1.

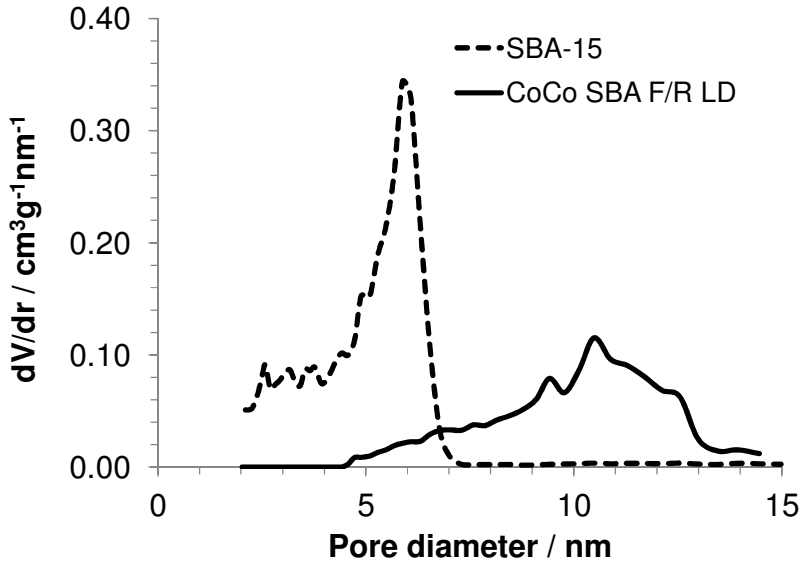

Figure 4: Pore size distribution of unmodified SBA and CoCo SBA F/R LD.

3.3.3 Comparison in dye content

Table 7 lists the amounts of dyes detected on the different SBA samples. The resulting dye ratios were similar in both CoCo materials, as well as in the PG materials, indicating same coupling behaviour. In all cases, FITC is more likely to be integrated into the material than RBITC. A possible explanation of this is the larger steric hindrance of RBITC due to its two additional ethyl groups on each site of the xanthene structure making the entry into the pores more difficult, especially if the pores are partially blocked by already coupled dyes. Furthermore, rhodamine B dyes are reported to preferentially form dimers and trimers in concentrated ethanol solutions[21] leading to an impeded diffusion of the dye aggregates into the mesopores and probably also to aggravated coupling to the amino groups because of the restricted dye mobility. A higher dye aggregation tendency can be expected in the reaction mixture for the dye labelling of PG SBA R 1, because of the high dye concentration and the fact that there is no other type of dye molecules disturbing the aggregation process. This can be the reason for the comparably lower RBITC coupling yield for PG SBA R 1. Another reason for the reduced RBITC coupling may be the ability to form hydrogen bonds with the hydroxyl-groups of the silica surface. By forming

hydrogen bonds with the silica surface, FITC is relatively fixed, promoting the reaction with surface bound amino groups. The given yields of coupled dyes for CoCo SBAs are related to the initial dye amount introduced into the synthesis (Table 4). The yields for PG SBAs correspond to the dye amount coupled assuming a 100% yield in post-synthetic amino-functionalization. For fluorescein and rhodamine modified PG SBAs, the coupling to 50% of the amino groups was considered as 100% yield for each dye. With exception of the FITC yield of CoCo SBA F/R HD, all yields were found to be below 20%. The low coupling yield for the CoCo material can be explained by only a fraction of APTES coupled to the dyes, resulting in less dye incorporation during the synthesis and some dye being washed out or degraded during Soxhlet extraction to remove the template.

Table 7: Amount of dye calculated per mg silica

Sample	FITC [nmol/mg][a]	RBITC [nmol/mg][a]	Ratio FITC/RBITC	Yield FITC [%]	Yield RBITC [%]
CoCo SBA F/R HD	5.9 ± 0.4	2.2 ± 0.1	1:0.4	46	16
CoCo SBA F/R LD	0.35 ± 0.03	0.17 ± 0.01	1:0.5	16	9
PG SBA F 1	4.6 ± 0.3			5	
PG SBA R 1		0.35 ± 0.02			0.4
PG SBA F/R 1	2.6 ± 0.2	1.9 ± 0.1	1:0.7	5	4
PG SBA F/R 2	8.0 ± 0.5	5.0 ± 0.3	1:0.7	16	11
PG SBA F/R 3	16 ± 1	9.1 ± 0.6	1:0.6	16	10
PG SBA F/R 4	28 ± 2	18 ± 2	1:0.6	14	8

[a]Values are given with 6% deviation (ε_{FITC}: 76,000 L mol^{-1} cm^{-1}, ε_{RBITC}: 37,700 L mol^{-1} cm^{-1}). The coupling yields are related to the initial dye amounts introduced during the synthesis.

Comparing CoCo SBA F/R HD and CoCo SBA F/R LD, the dye concentration was higher in CoCo SBA F/R HD which leads to a higher amount of FITC-APTES and RBITC-APTES during the SBA synthesis. Furthermore, the APTES concentration was higher in the CoCo SBA F/R LD synthesis which influences the co-condensation, since more free APTES is available. The free APTES possibly competes with dye-APTES during incorporation into the silica network, leading to the observed lower coupling yield in CoCo SBA F/R LD.

The post-synthetic amino-functionalization was most likely < 100% leading to underestimated coupling yields for the PG materials. Furthermore, pore blocking from already coupled dyes or the presence of micropores can reduce the accessibility of the amino groups.[22] More material was needed to synthesize

the PG SBA F/R and PG SBA F/R 1 samples, therefore SBA-NH_2 1 was made in a large batch to ensure that enough material was present for multiple reactions. In a larger batch the grafting procedure tended to produce less amino-functionalized SBAs as can be concluded by comparing PG SBA F/R 1, PG SBA F/R 1 and PG SBA F/R 2. For equal batches the amount of dye labelling could be measurably tuned by varying the amount of APTES during the synthesis as seen for the samples PG SBA F/R 2–4 (Table 7). Hence, the amount of dyes on the mesoporous silica can be tuned by increasing the APTES-dye concentration in the synthesis or by enhancing the post-synthetic amino-functionalization. CLSM measurements showed homogenous distributions for FITC as well as RBITC dyes in all SBAs (Figure 5).

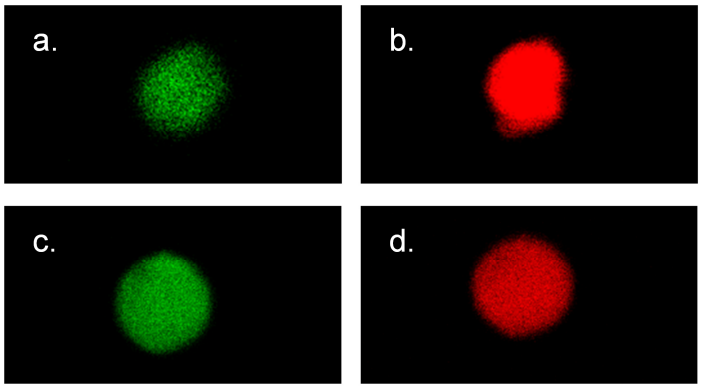

Figure 5: CLSM illustrations of dye modified SBAs. Top: CoCo SBA F/R HD, particle size ~3 µm. Bottom: PG SBA F/R 1, particle size ~5 µm. Left: sample was illuminated at 488 nm. Right: illumination at 544 nm.

3.3.4 FRET mechanism

Spectral investigation

As mentioned in the previous chapter, fluorescein derivatives have been used as sensing species displaying linear dependency over wide ranges of ammonia concentrations.[23-25] FRET-based optical chemosensors for the detection of ammonia have been reported[26-29] and one advantage has been highlighted as they can generate dual or multiple emissions under a single wavelength excitation, resulting in more effective ratiometric detection in comparison to those that need two separate excitation wavelengths.[30] Furthermore, their design can easily be modified by varying the FRET components.

Depending on the ambient pH value, fluorescein exists in cationic, neutral, monoanionic or dianionic forms or as a mixture thereof.[31] Absorption as well as emission spectra are dependent on the presence of species in different protonation states.[31] The acid dissociation constants in solution reported for fluorescein are in the range of $pK_{cationic}$ = 2.00–2.25, $pK_{neutral}$ = 4.23–4.4 and $pK_{monoanionic}$ = 6.31–6.7, depending on the specific conditions and measurement techniques.[31-33] Rhodamine B can be present in a few different species under extreme conditions[34] but only the cationic and zwitterionic forms are fluorescent. The pK_a of the cationic form in solution is in the range of 3.22–4.2, depending on the specific conditions and measurement techniques.[34-37] For spectral investigation of the SBAs, the particles were immobilized in a transparent organic modified xerogel film, the properties of which have already been reported in Section 2.3.1.[8] The emission spectrum of PG SBA F 1 shows an emission band at 515 nm and a shoulder at 542 nm, indicating the presence of at least two emittive species, which are assigned to the monoanionic and dianionic forms respectively (Figure 6).

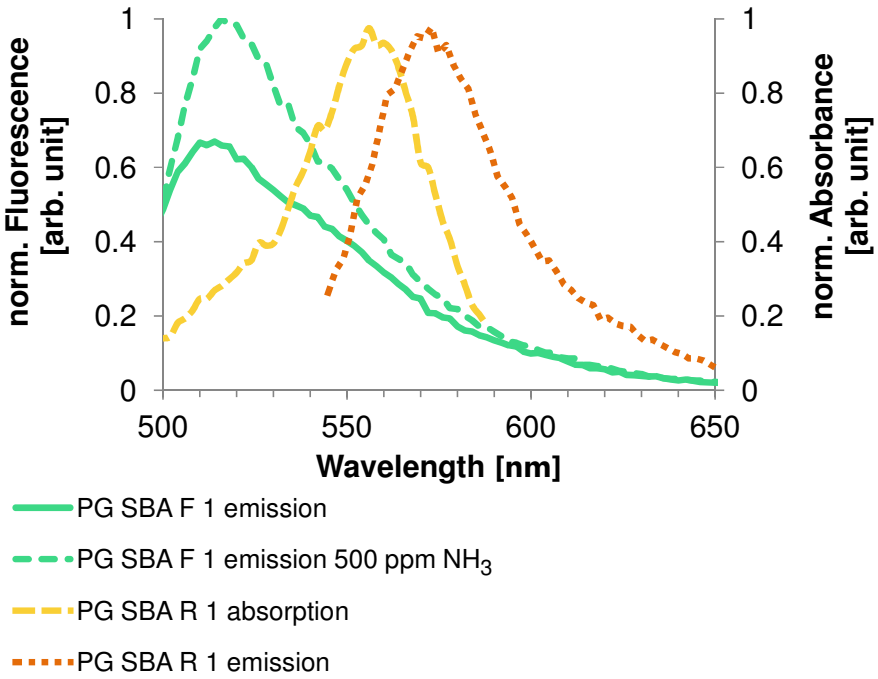

Figure 6: Emission and absorption spectra of investigated FRET dye pair on SBA particles immobilized in the unlabelled xerogel. The spectral overlap is increasing with increasing formation of fluorescein dianion. Excitation wavelengths: 484 nm (F) and 535 nm (R). The emission of rhodamine B (573 nm) is red-shifted when present in a FRET system to 595 nm (see Figure 7).

Exposure to NH_3 leads to deprotonation of the monoanionic species forming more dianionic species, which results in an enhancement of its fluorescence. The higher intensity of emission scales to an increase of the quantum yield (Φ = 0.93) and the high molar absorptivity of the dianionic fluorescein form.[31] The absorption spectrum of rhodamine has a peak at 553 nm and a shoulder around 535 nm, which suggests the presence of both fluorescent rhodamine species (Figure 6). The increase in fluorescein emission upon ammonia exposure leads to a larger overlap of fluorescein emission and rhodamine absorption that results in enhanced FRET efficiency and thus increased rhodamine emission (Figures 7 and 8).

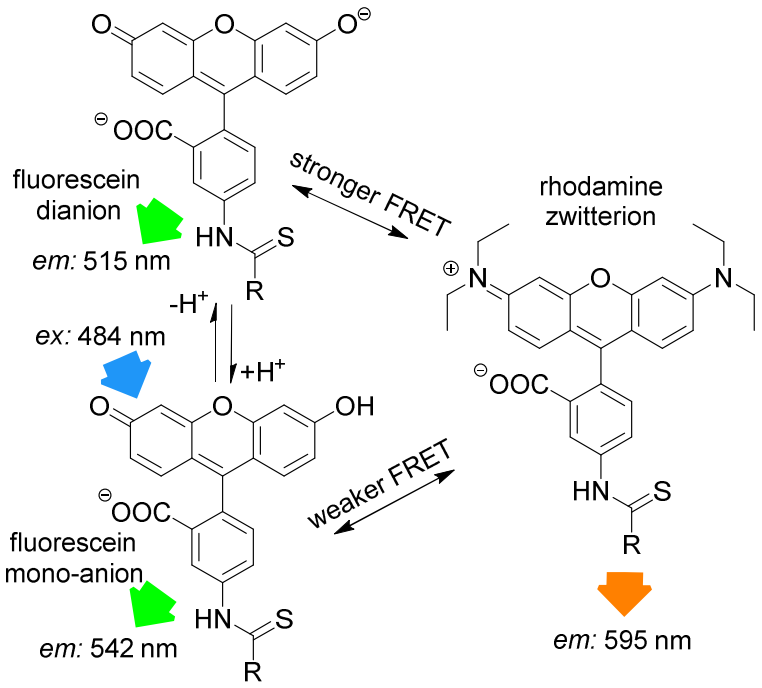

Figure 7: FRET mechanism between fluorescein and rhodamine. R = coupling to amino-functionalized silica.

The wavelength range of the emission bands is comparable for CoCo SBA F/R HD and PG SBA F/R 1 coatings (Figure 8a, c). Although, the PG material was found to have less dye content, the fluorescein emission intensity is similar to the CoCo material and rhodamine emission intensity even higher. This observation leads to the conclusion that the high dye loading in the co-condensed material leads to fluorescence quenching. The more intense rhodamine emission in the PG material is based on the determined fluorescein/rhodamine proportion in the materials, being higher for the PG

material. CoCo SBA F/R LD coatings exhibit comparable low rhodamine emission intensity due to less dye incorporation and the emission band is more blue-shifted in comparison to the SBA with higher dye loadings (Figure 8b). Figure 8d shows the emission spectra of a FITC and RBITC modified xerogel film. The fluorescence intensity (arb. unit) scale cannot be compared with a, b and c. Detector adjustments were carried out since the measurement under the identical set-up conditions resulted in an overflow of fluorescence intensity.

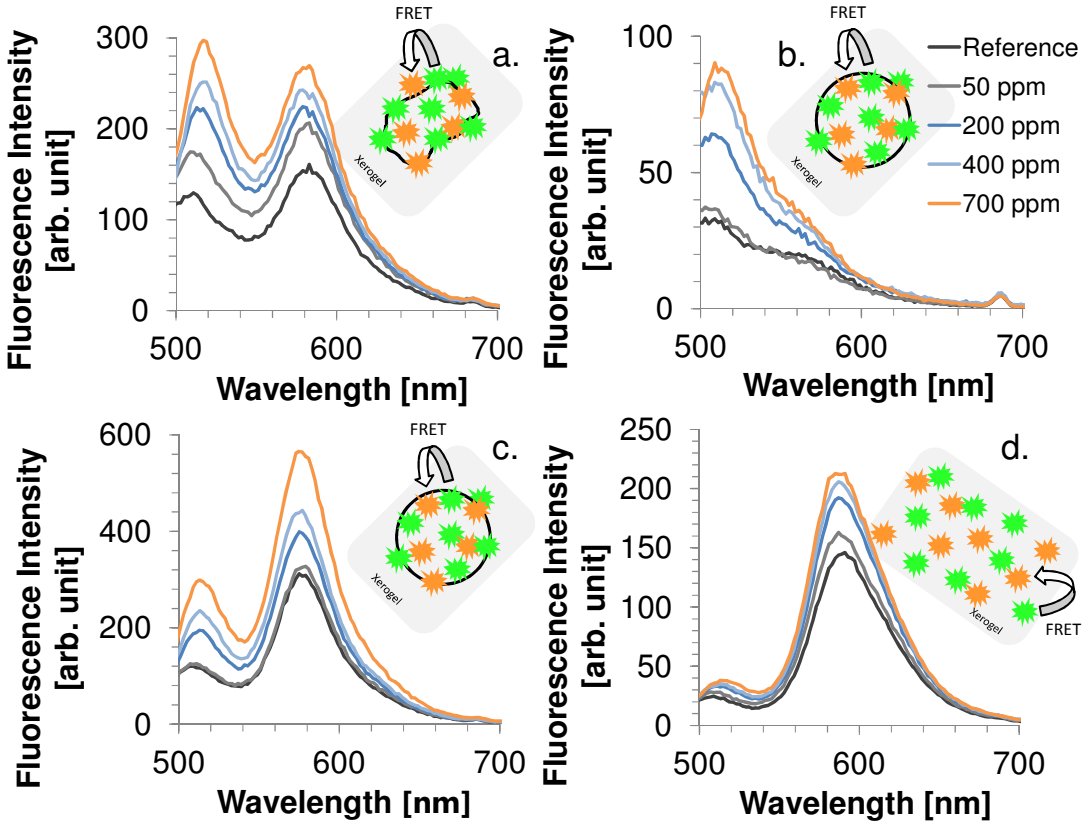

Figure 8: Spectral behavior upon NH_3 exposure. Coatings: a.: CoCo SBA F/R HD, b.: CoCo SBA F/R LD, c.: PG SBA F/R 1, d.: FITC/RBITC (ratio 4:1) modified xerogel film. Excitation wavelength was 484 nm.

Figure 9 illustrates the spectral response to NH_3 by the increase of rhodamine maximum fluorescence emission at ca. 580 nm which was similar for the CoCo SBA F/R HD and PG SBA F/R 1 coatings. The exposure to 1,000 ppm of gaseous NH_3 led to a ca. 1.5-fold increase of the rhodamine fluorescence intensity. PG SBA F/R 2–4 did not respond to NH_3 with an increase of rhodamine fluorescence emission. This observation indicates that higher dye amounts are not necessarily beneficial for this FRET system.

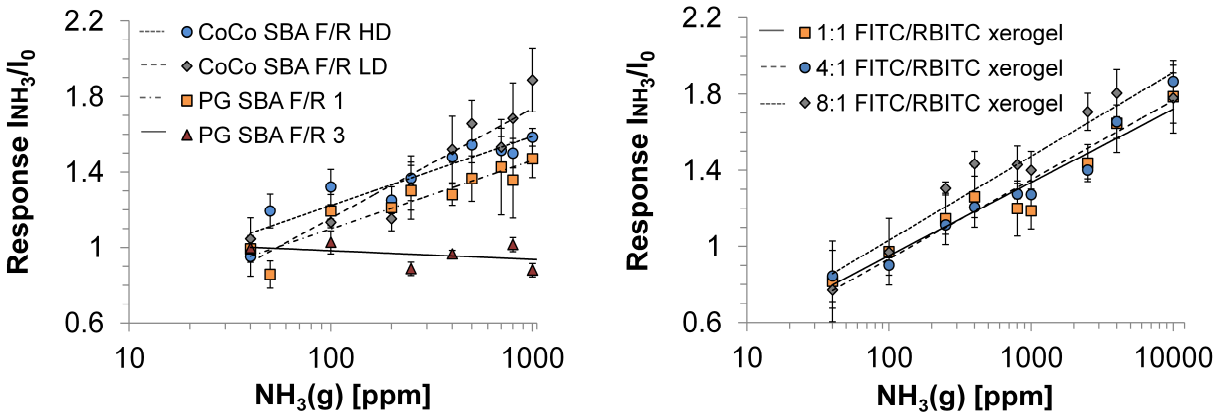

Figure 9: Logarithmic dependency of rhodamine fluorescence emission intensity change (relative change in emission intensity) on NH_3 concentration for the investigated coatings. I_0 = fluorescence intensity of the reference (water), I_{NH_3} = fluorescence intensity in presence of NH_3 (ex: 484 nm).

A closer look at the fluorescence spectra of the PG SBA F/R 3 coating reveals that the fluorescein emission intensity decreased and the rhodamine fluorescence emission intensity remained unchanged although the total dye amount was 5 times higher in comparison to PG SBA F/R 1. The larger dye amount probably led on one hand to an enhanced FRET activity because of the higher amount of dye pairs but on the other hand to more fluorescence quenching due to the high dye density on the particles as observed for the co-condensed material. The CoCo SBA F/R LD coating shows a better response towards ammonia for concentrations above 400 ppm. However, the rhodamine emission is low in comparison to the more intense fluorescein emission and in addition is close to the fluorescein emission band. Therefore, the increasing intensity of the fluorescein fluorescence emission tail may contribute to the increase of rhodamine fluorescence emission intensity and lead to overestimation of the ammonia response. The contribution of fluorescein fluorescence emission in PG SBA F/R 1 was evaluated by fitting Gaussians and is discussed later in this section. The relative response of the xerogel films with dye ratios of 1:1, 4:1 and 8:1 was similar and also comparable to the particle coatings within standard deviations. This data shows that a higher ratio of donor/acceptor did not lead to a higher FRET efficiency, so that the relative response was independent of the ratio. Since higher amount of dyes can be integrated into the xerogel films, the range of ammonia concentration, that can be sensed, is extended. Fluorescence quenching for particle coatings occurred at concentrations between 1,000–2,500 ppm and for xerogel films between

10,000–40,000 ppm. All coatings show logarithmic behavior in NH_3 response. Coatings with only rhodamine labelled particles (PG SBA R 1, excited at 535 nm) and RBITC modified xerogel responded to NH_3 with a slight decrease in fluorescence emission intensity which can be explained by either the continuous deprotonation of the cationic species forming more zwitterionic species which results in decreased fluorescence emission intensity at 576 nm (Figure 11c) or by reabsorption of rhodamine emission. This could also be another explanation for the decreasing intensity of rhodamine fluorescence emission for the PG SBA F/R 2–4 coatings. Coatings with only FITC labelled particles (PG SBA F 1) responded logarithmically between 0 and 1,000 ppm. A FITC modified xerogel responded linearly only from 200 to 1,000 ppm.

Taking the calculated BET surface from Table 6, the amount of dye in a defined FRET sphere, with a radius of 5 nm, can be determined (Table 8). According to these results, less than one dye molecule is present in the required FRET distance of 10 nm. Since energy transfer is taking place, it is suggested that the dye distribution is macroscopically homogenous as observed by CLSM. However, the dyes can be inhomogeneously distributed in a single hexagonal pore leading to irregular dye-dye distances and locally varying dye concentrations (Figure 10).

Table 8: Amount of dye in a FRET sphere with a radius of 5 nm calculated from the BET surface

Sample	FITC	RBITC
CoCo SBA F/R HD	1.23	0.46
CoCo SBA F/R LD	0.08	0.04
PG SBA F 1	0.4	
PG SBA R 1		0.04
PG SBA F/R 1	0.16	0.12
PG SBA F/R 2	0.74	0.46
PG SBA F/R 3	2.31	1.48
PG SBA F/R 4	4.56	2.93

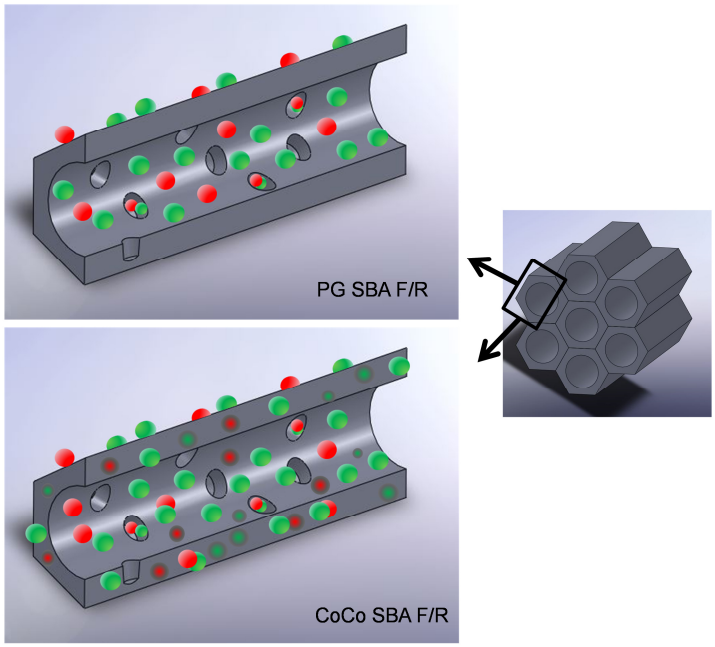

Figure 10: Suggested dye distribution on SBA.

Gaussian evaluation

The emission wavelengths of the FRET dye pair are not completely separated, leading to an overlap between fluorescein and rhodamine emission. Exposure to NH_3 leads to an increase in the emission intensities of both dye molecules (fluorescein and rhodamine), because of the enhanced emission of deprotonated fluorescein on the one hand and the resulting increased FRET on the other hand. Therefore, it is difficult to estimate if the main gain in rhodamine intensity is caused by the enhanced energy transfer. Gaussian fitting to photoluminescence spectra is a common procedure for identifying the involved species which contribute to the final entire emission band.[38-40] To evaluate the contribution of the increasing fluorescein emission upon NH_3 exposure, to the increasing rhodamine emission, Gaussian fitting for the PG SBA F/R 1 emission bands was performed. Only fluorescein and rhodamine labelled particles were fitted to find the peak wavelengths and fluorescence tail lengths of each species needed to account for the final spectra. As mentioned previously, the fluorescent species suggested for fluorescein are the monoanionic and dianionic forms and cationic and zwitterionic for rhodamine. Therefore, two Gaussians were fitted to each reference spectrum (Figure 11a, c). Since intensity and peak wavelength is changed for fluorescein emission as a consequence of changed monoanionic/dianionic dye proportion upon NH_3 exposure, two Gaussians were

fitted to a spectrum obtained upon exposure to 1,000 ppm NH_3 (Figure 11b). The values for peak wavelength and the full width at half maximum were set as initial values for the Gaussian fitting of the spectra obtained by fluorescein and rhodamine labelled PG particles (Figure 11d–f).

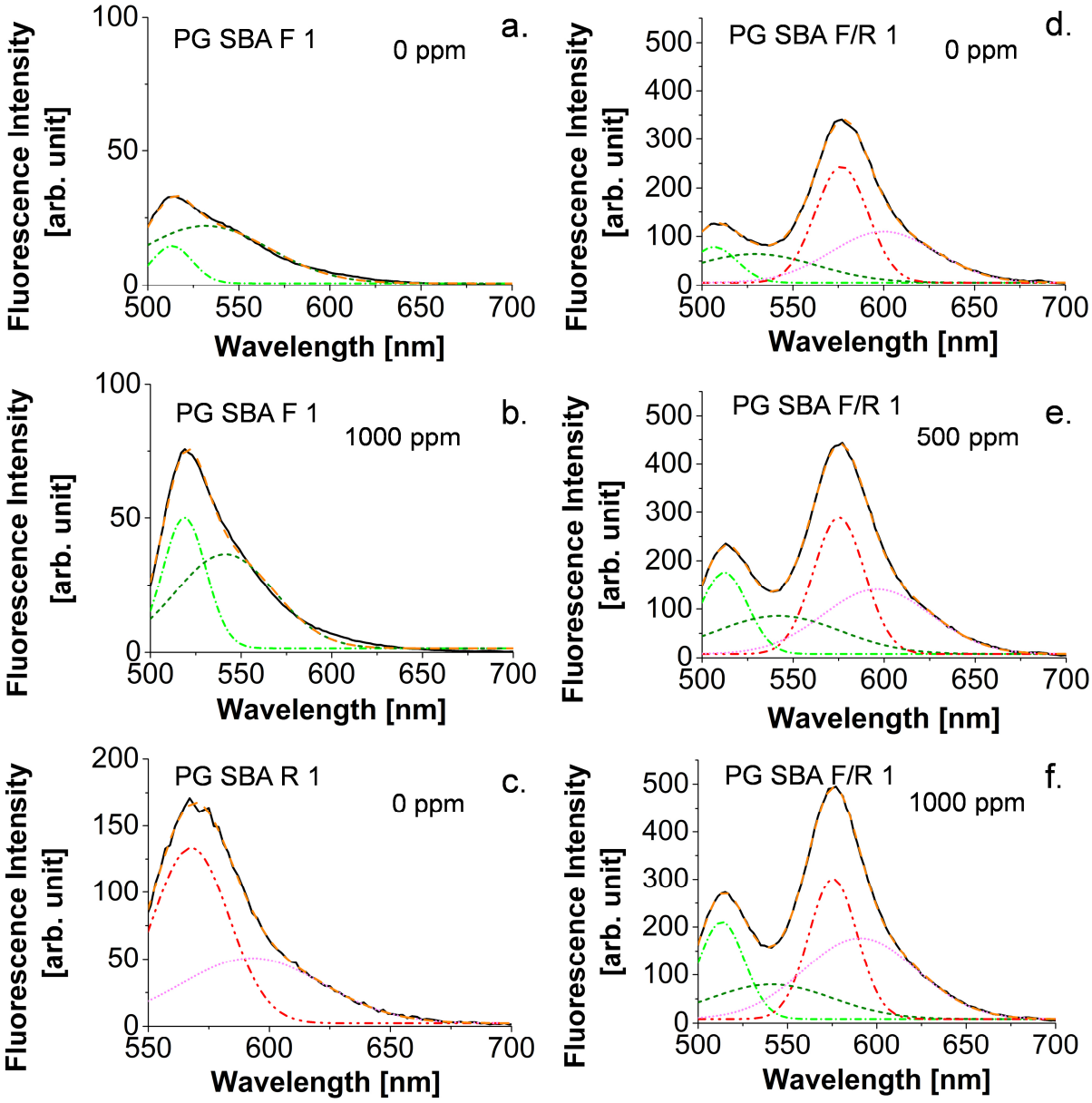

Figure 11: Gaussian evaluation on the fluorescence spectra of PG SBA F 1, PG SBA R 1, and PG SBA F/R 1. a.: PG SBA F 1 exposed to 0 ppm NH_3; b.: PG SBA F 1 exposed to 1,000 ppm NH_3; c.: PG SBA R 1 exposed to 0 ppm NH_3; d.: PG SBA F/R 1 exposed to 0 ppm NH_3; e.: PG SBA F/R 1 exposed to 500 ppm NH_3; f.: PG SBA F/R 1 exposed to 1,000 ppm NH_3. Gauss bands: light green: F dianion; dark green: F monoanion; red: R cation; pink: R zwitterion. The excitation wavelength was 484 nm.

Figure 12 illustrates the trend in peak surface area received from the Gaussian evaluation on the fluorescence spectra of PG SBA F/R 1 obtained upon exposure to 0, 250, 500, 1,000 and 2,000 ppm NH_3. With increasing NH_3 concentration, more fluorescein dianions are formed from further deprotonation of the fluorescein monoanions which is reflected in the increasing area of the corresponding Gaussian band located at ca. 512 nm. The maximum peak wavelength is red-shifted with higher NH_3 concentrations from 507 to 514 nm. The fluorescein monoanion band increases from 0–500 ppm and starts to decrease when exposed to concentrations above 500 ppm. This observation suggests the presence of neutral species, which are deprotonated forming more monoanionic species. At the same time, deprotonation of mono- to dianonic species occurs. Above 500 ppm, every neutral fluorescein species has been deprotonated in fluorescein monoanions. The deprotonation of the monoanions into dianions leads to the decrease in the peak surface area of the fluorescein monoanion species. The maximum peak wavelengths show a significant red-shift from 529 to 542 nm between 0 and 250 ppm NH_3. Subsequent increases in the NH_3 concentration do not lead to a further red-shift.

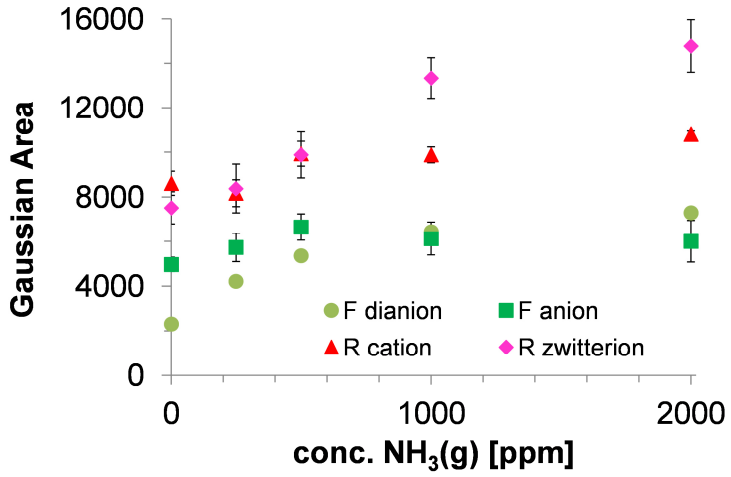

Figure 12: Evolution in peak surface area for the different fluorescein and rhodamine dye species.

Both the rhodamine cation band located at 576 nm and the rhodamine zwitterion band located at ca. 590 nm, increase with increasing NH_3 concentration. Interestingly, the increase of the zwitterionic band occurs in a much higher extent (1.78 times) in comparison to the cationic band (1.15 times) and the maximum peak wavelength exhibits a blue-shift of 10 nm. This indicates that

the energy transfer from fluorescein to the zwitterionic form of rhodamine is preferred, assuming that no significant amount of rhodamine cation is converted to zwitterion due to the NH_3 exposure. The increase of both cationic and zwitterionic emissions of the rhodamine Gaussians is consistent with the energy transfer. Furthermore, only the fluorescein monoanion fluorescence emission can contribute to the rhodamine emission intensity because of its long emission tail. The fact that the Gaussian area of the fluorescein monoanionic species is decreasing with increasing NH_3 concentration supports the energy transfer model.

3.3.5 Lifetime and FRET efficiency

The lifetime of F was measured for the particle coatings at four different NH_3 concentrations (Table 9).

Table 9: Lifetime of F[a] in CoCo and PG SBA F/R in presence and absence of NH_3

NH_3 conc. [ppm]	Lifetime τ CoCo SBA F/R HD [ns]/Chi-squared (χ^2)	Lifetime τ PG SBA F/R 1 [ns]/Chi-squared (χ^2)
0	2.84/0.96	2.84/0.88
100	2.69/0.86	2.77/1.06
400	2.58/0.93	2.72/0.86
1,000	2.48/1.04	2.54/0.89

[a]Mixture of anion and dianion lifetime

It has to be considered that the monoanionic and dianionic form contribute to the fluorescence decay but the main contribution probably comes from the F dianion (Figure 6 and Figure 11, d–f). A decrease in F lifetime was observed with increasing NH_3 concentration which gives raise of an enhanced energy transfer to R. The FRET efficiencies were not evaluated for these sensor coatings since the change in F fluorescence intensity in presence of NH_3 is not only due to an enhanced energy transfer but also due to the formation of more dianions leading to an increased fluorescence intensity (Figure 11, d–f). This leads in turn to an underestimated FRET efficiency. Furthermore, the distance for the FRET calculation should be a fixed value which requires a homogenous distribution of the dyes in the SBA. The values in Table 8 lead to the assumption

that the dye distribution is irregular leading to different FRET distances and thus strongly different FRET efficiencies.

3.3.6 Gas sensor measurements

Images from optical microscopy and scanning electron microscopy show homogenous distribution of the particles in the xerogel films (Figure 13). CoCo SBA F/R HD coatings tend to form larger particle agglomerations in comparison to the other particle coatings (Figure 13a). Solvent casting of 20 µL of the reported sol solution on to a 1.5 × 1.5 × 0.1 cm^3 PMMA substrate resulted in smooth dry films with a thickness of 6 µm.[8] Coatings without particles display a smooth and even surface (Figure 13d, f) whereas coatings with particles show an irregular surface with embedded SBA particles (Figure 13a–c, e).

In order to investigate the dye accessibility of the coatings by the NH_3 gas, experiments were performed using the device shown schematically in Section 2.2.5. The gas flow was switched between a NH_3/N_2 gas mixture and pure N_2. When ammonia gas was introduced, it diffused into the xerogel film where deprotonation of the fluorescein dyes occurred, leading to the increase in rhodamine fluorescence emission. The dyes in the coatings were excited at 470 nm from the top of the gas sensor (Figure 1). The PMMA substrate acted as a waveguide and the fluorescence intensity was thus monitored at the edge perpendicular to the irradiation. The long pass filter only allowed light of wavelengths from 550 nm to pass to the phototransistor. Thus, the change in fluorescence from 490 to 550 nm upon fluorescein deprotonation-protonation was not monitored. To reduce cross-sensitivity or cooling with humidified air, care was taken, that during switching the gases, the humidity did not exceed 4%. A measurement was always started by purging the setup with gaseous N_2, which acted simultaneously as the reference gas and carrier gas. After 10 minutes, this valve was closed and the valve for purging with NH_3 gas was opened until the signal reached the maximum sensor response. The baseline was recovered by closing the NH_3-line and re-opening the N_2-line.

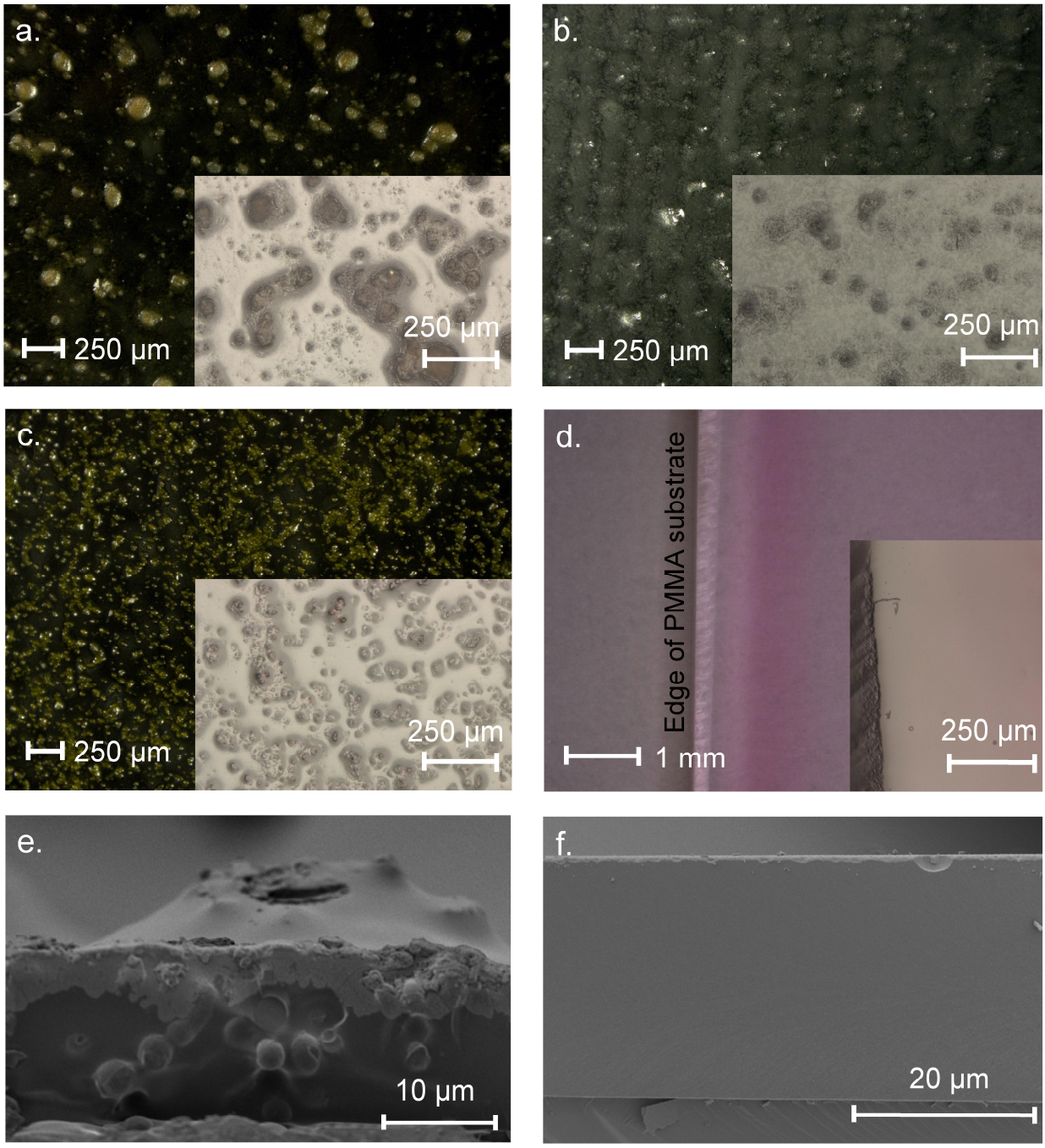

Figure 13: Optical microscopy images of the investigated coatings. a.: CoCo SBA F/R HD coating; b.: CoCo SBA F/R LD coating; c.: PG SBA F/R 1 coating; d.: 4:1 FITC/RBITC xerogel coating. SEM images. e.: Cut of PG SBA F/R 1 coating; f.: cut of 4:1 FITC/RBITC xerogel coating. The film thicknesses on the silicon wafers for the SEM images do not correspond to the thicknesses on the investigated PMMA substrates.

The top graph of Figure 14 depicts the sensor response for the different coatings towards 1,000 ppm NH_3. A similar response and change in rhodamine fluorescence intensity due to the energy transfer was obtained for the CoCo SBA F/R HD and PG SBA F/R 1 (Figure 14, top, responses a and b) coatings in accordance with the above spectral investigations (Figure 8). The fluorescence intensity of rhodamine changed by the factor 1.12 for CoCo SBA F/R HD and 1.17 for PG SBA F/R.

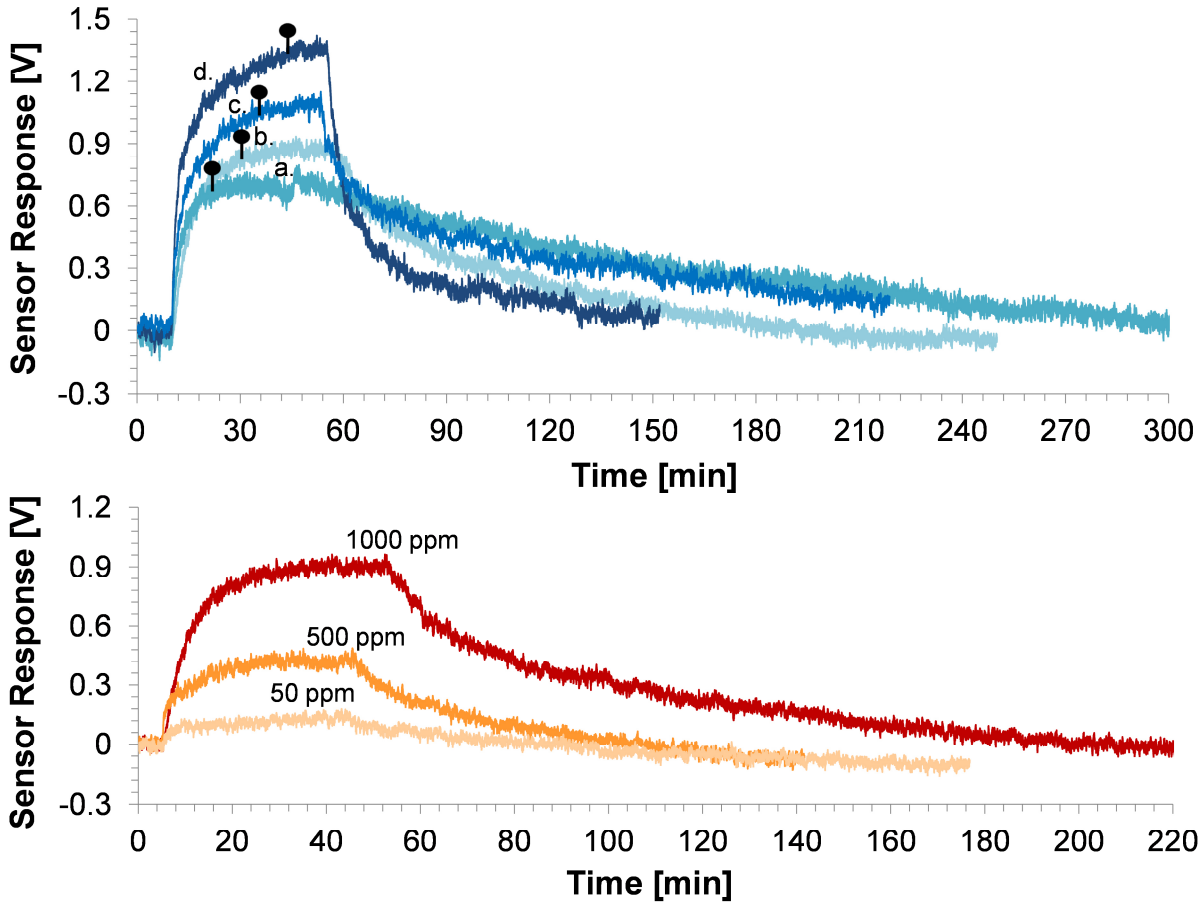

Figure 14: Flow cell gas sensor response upon exposure to 1,000 ppm gaseous NH_3. Top: a.: CoCo SBA F/R HD coating; b.: PG SBA F/R 1 coating; c.: unlabelled SBA in 4:1 FITC/RBITC xerogel coating; d.: 4:1 FITC/RBITC xerogel coating. The pins mark the time required to achieve 95% of the maximum sensor response. Bottom: Response of PG SBA F/R towards different NH_3 concentrations.

Because of the larger pore size and different morphology, the response time was slightly faster for the co-condensed material, due to the faster diffusion of NH_3 into the coating. However, the co-condensed SBA had a much longer recovery time than the post-grafted SBA. It is reported that co-condensed mesoporous materials have a higher number of free hydroxyl groups on the surface due to

the extraction of the template rather than calcination of the post-grafted materials.[41] Therefore, a possible reason for the lower recovery can be that the NH_3 gas is more strongly adsorbed by the co-condensed material by forming more hydrogen bonds with the free surface hydroxyl groups. In addition, the free silanol (SiOH) groups of the silica framework can be deprotonated by the basic NH_3 gas resulting in NH_4^+ and SiO^- leading to electrostatic NH_3 adsorption on the silica surface. Better responses were obtained for the 4:1 FITC/RBITC xerogel coatings (Figure 14, top, responses c and d). The fluorescence intensity of rhodamine changed by the factor 1.24 for both coatings. Since the xerogel is very smooth, the NH_3 gas permeability is reduced, leading to the longer response time. The incorporation of unlabelled SBA into the xerogel coating did not lead to faster response and recovery times (Figure 14, top, response c), as expected from the introduced porosity coming from the mesoporous particles. The exposure of the PG SBA F/R 1 coating to different NH_3 gas concentrations led to different sensor responses (Figure 13, bottom). The lowest detectable amount of ammonia with this setup was 10 ppm. Cyclic measurements with the PG SBA F/R 1 coating (Figure 15) demonstrate the reversibility of this coating by exhibiting the same loss and recovery in signal intensity in each cycle. The sensor response of the CoCo SBA F/R HD coating was not reproducible since the long recovery time is subjected to thermal drifting. It is reported that the photoluminescence intensity from a rhodamine and fluorescein contained silica gel decreases with temperature.[42] The response of CoCo SBA F/R HD could be reproduced when warming the coating to 70 °C for 2 h.

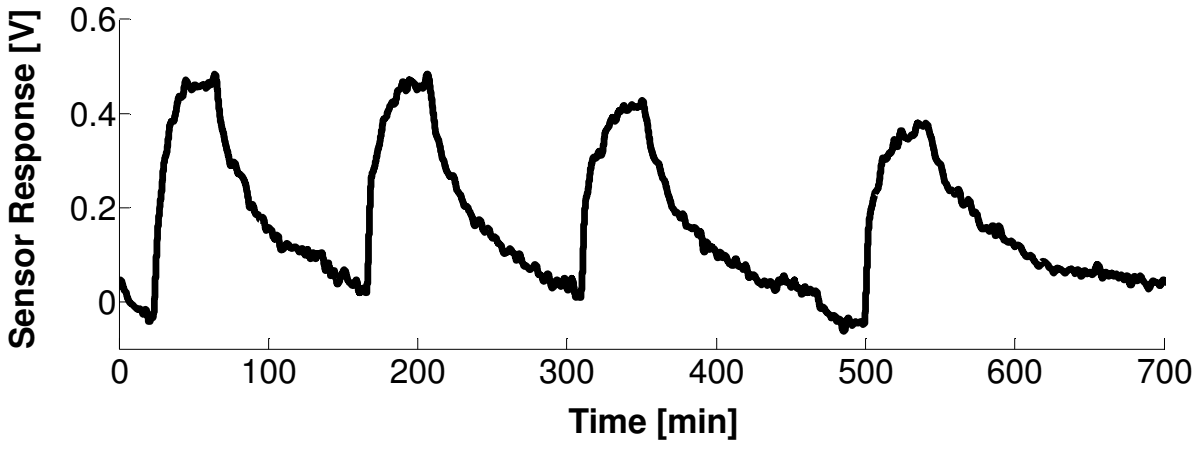

Figure 15: Drift compensated cyclic response of the PG SBA F/R 1 coating to 500 ppm NH_3.

3.4 Conclusions

The FRET activity of fluorescein and rhodamine modified mesoporous SBAs has been studied by observing the change in R fluorescence emission intensity when exposing the particles, immobilized into transparent xerogel coatings, to different NH_3 gas concentrations. Large dye loadings on the SBA lead to fluorescence quenching and hence to an inoperative FRET system. The impact of the different structural properties of co-condensed and post-grafted materials was investigated with the flow cell optical gas sensor setup. The integration of dye modified silica particles into the xerogel sensor resulted in shorter response times in comparison to the non-porous FITC/RBITC sensor coatings. The response time was dependent on the structure of the immobilized SBA material, whereas the recovery time was strongly dependent on the surface properties of the material. The free silanol groups probably adsorb the NH_3 molecules by the formation of hydrogen bonds or by electrostatic interaction. The ability to adsorb the NH_3 molecules on the silica surface determines whether the particle coatings can be applied for reproducible and fully reversible sensor applications. The relative change in rhodamine emission intensity upon ammonia exposure was similar for all coatings. However, the absolute response was higher for the FITC/RBITC xerogel coating which leads to better sensitivity and enhanced resolution of the optical sensor.

3.5 References

1 S. Widmer, M. J. Reber, P. Müller, C. E. Housecroft, E. C. Constable, R. M. Rossi, D. Brühwiler, L. J. Scherer and L. F. Boesel, *Analyst,* 2015, **140**, 5324-5334.

2 N. Gartmann, C. Schütze, H. Ritter and D. Brühwiler, *J. Phys. Chem. Lett.*, 2010, **1**, 379-382.

3 N. Gartmann and D. Brühwiler, *Angew. Chem. Int. Ed.*, 2009, **48**, 6354-6356.

4 Y. Ma, L. Qi, J. Ma, Y. Wu, O. Liu and H. Cheng, *Colloids Surf. A,* 2003, **229**, 1-8.

5 A. Katiyar and N. G. Pinto, *Small*, 2006, **2**, 644-648.

6 L. Wang, T. Qi, Y. Zhang and J. Chu, *Micropor. Mesopor. Mater.*, 2006, **91**, 156-160.

7 J. Lei, L. Wang and J. Zhang, *Chem. Commun.*, 2010, **46**, 8445-8447.

8 S. Widmer, M. Dorrestijn, A. Camerlo, S. K. Urek, A. Lobnik, C. E. Housecroft, E. C. Constable and L. J. Scherer, *Analyst*, 2014, **139**, 4335-4342.
9 E. P. Perman, *J. Chem. Soc.*, 1901, **79**, 718-725.
10 E. P. Perman, *J. Chem. Soc.*, 1903, **83**, 1168-1184.
11 S. Brunauer, P. H. Emmett and E. Teller, *J. Am. Chem. Soc.*, 1938, **60**, 309-319.
12 J. Landers, G. Y. Gor and A. V. Neimark, *Colloids Surf. A: Physiochem. Eng. Aspects*, 2013, **437**, 3-32.
13 M. Kruk, M. Jaroniec, R. Ryoo and J. M. Kim, *Microporous Mater.*, 1997, **12**, 93-106.
14 M. O. Okuom, M. V. Wilson, A. Jackson and A. E. Holmes, *Int. J. Spectrosc.*, 2013, DOI: 10.1155/2013/245376.
15 H. Leonhardt, L. Gordon and R. Livington, *J. Phys.Chem.*, 1971, **75**, 245-249.
16 http://www.multid.se/pdf/cps%20physchem%200309005.pdf, accessed June 2015.
17 P. I. Ravikovitch and A. V. Neimark, *J. Phys. Chem. B*, 2001, **105**, 6817-6823.
18 Q. Huo, D. I. Margolese, U. CIesla, D. G. Demuth, P. Feng, T. E. Gier, P. Sieger, A. Firouzi and B. F. Chmelka, *Chem. Mater.*, 1994, **6**, 1176-1191.
19 N. Gartmann and D. Brühwiler, *Materials*, 2011, **4**, 1096-1103.
20 F. Hoffmann, M. Cornelius, J. Morell and M. Fröba, *Angew. Chem. Int. Ed.*, 2006, **45**, 3216-3251.
21 F. López Arbeloa, P. Ruiz Ojeda and I. López Arbeloa*, J. Lumin.*, 1989, **44**, 105-112.
22 H. Ritter and D. Brühwiler, *J. Phys. Chem. C*, 2009, **113**, 10667-10674.
23 L. Peng, X. Yang, L. Yuan, L. Wang, E. Zhao, F. Tian and Y. Liu, *Opt. Commun.*, 2011, **284**, 4810-4814.
24 A. Persad, K.-F. Chow, W. Wang, E. Wang, A. Okafor, N. Jespersen, J. Mann and A. Bocarsly, *Sens. Actuators, B*, 2008, **129**, 359-363.
25 Y. Takagai, Y. Nojiri, T. Takase, W. L. Hinze, M. Butsugan and S. Igarashi, *Analyst*, 2010, **135**, 1417-1425.
26 T. Abel, B. Ungerbock, I. Klimant and T. Mayr, *Chem. Cent. J.*, 2012, **6**, 124.
27 C. Preininger, M. Ludwig and G. J. Mohr, *J. Fluoresc.*, 1998, **8**, 199-205.
28 Q. Chang, J. Sipior, J. R. Lokowicz and G. Rao, *Anal. Biochem.*, 1995, **232**, 92-97.

29 K. Waich, S. Borisov, T. Mayr and I. Klimant, *Sens. Actuators, B*, 2009, **139**, 132-138.
30 J. Lei, L. Wang and J. Zhang, *Chem. Commun.*, 2010, **46**, 8445-8447.
31 R. Sjöback, J. Nygren and M. Kubista, *Spectrochim. Acta, Part A,* 1995, **51**, L7-L21.
32 M. M. Martin and L. Lindqvist, *J. Lumin.*, 1975, **10**, 381-390.
33 H. Leonhardt, L. Gordon and R. Livingston, *J. Phys. Chem.*, 1971, **75**, 245-249.
34 R. W. Ramette and E. B. Sandell, *J. Am. Chem. Soc*., 1956, **78**, 4872-4878.
35 S. Woislawski, *J. Am. Chem. Soc*., 1953, **75**, 5201-5203.
36 S.-L. Hii, S.-Y. Yong and C.-L. Wong, *J. Appl. Phycol*., 2009, **21**, 625-631.
37 Y. A. Gomaa, M. J. Garland, F. McInnes, R. F. Donnelly, L. K. El-Khordagui and C. Wilson, *Int. J. Pharm*., 2012, **438**, 140-149.
38 A. J. G. Otuka, V. Tribuzi, D. S. Corrêa and C. R. Mendonça, *Opt. Mater. Express*, 2012, **2**, 1803-1808.
39 L. Zhang, Z. Fu, Z. Wu, Y. Wang, X. Fu and T. Cui, *Mater. Res. Bull*., 2014, **56**, 65-70.
40 Q. Wang, Z. Ci, G. Zhu, M. Que, S. Xin, Y. Wen and Y. Wang, J. *Solid State Sci. and Technol*., 2012, **1**, R92-R97.
41 F. Kleitz, W. Schmidt and F. Schüth, *Micropor. Mesopor. Mater*., 2003, **65**, 1-29.
42 W. Takechi, H. Yamaguchi, K. Ito and H. Aizawa, "Temperature Dependence of Phosphor Contained Silica Gel Sensor" in *SICE-ICASE International Joint Conference*, 2006, pp. 1574-1577.

Chapter 4

Fibre Ammonia Gas Sensor

4.1 Introduction

In the last step of this dissertation, the FITC/RBITC FRET sensor system discussed in Chapter 3 was applied to PMMA optical fibres in order to construct an intrinsic fibre-optic ammonia gas sensor. Fiber-optic chemical sensors provide an efficient method for in situ and real-time ammonia sensing.[1-5] The elastic and transparent ormosil based xerogel is an excellent cladding material for flexible fibres. Optical fibres have light weight, small size and resemble textile fibres. Thus, modified optical fibres could be integrated into clothing by common manufacturing processes such as weaving, sewing, knitting and lamination to add new features.[6] Wearable real-time sensors are comfortable and would facilitate working in a contaminated area monitoring the ammonia gas concentration at the current position. In this effort, a new flow cell sensor setup was built in which the clad fibre was fixed. This chapter presents the results from preliminary fibre sensor experiments.

4.2 Experimental

4.2.1 Preparation of xerogel claddings

Sol preparation. The FITC/RBITC (4:1 ratio) and unlabelled sols were prepared by the procedure reported in Section 3.2.3 and reference 7.

Fibre cladding. A bare PMMA fibre was purchased from AFO. The fibres were cleaved with a scissor into 9 and 60 cm long individual fibres. The fibres were coated in the entire length with the sol by manual dip-coating (coating speed was 5 ± 2 cm/s) into the dye-doped sol solution. The fibres were then vertically hanged up in the oven and dried at 70 °C for 3 days. To obtain thicker claddings of manually dip-coated fibres, the single dip-coated fibres were dip-coated a second time and dried for further 3 days. A cladding with integrated SBA-15 particles was obtained by dip-coating the fibre with the dye-doped sol solution. Then, the particles were trickled manually over the fibre from a distance of ca. 1

cm, the sol acting like a glue. The SBA-15 impregnated fibre was dried for 3 days at 70 °C.

4.2.2 Characterization methods

Optical microscopy. The images were recorded on the coatings prepared for the gas sensor measurements using an optical microscope from Keyence.

Refractive index measurement. Refractive index measurements on the sols were performed on a device from Atago equipped with an illuminator. The refractive indices of unlabelled solid xerogel and the bare PMMA fibre were determined using certified refractive index liquids made by Cargille labs.

Scanning electron microscopy (SEM). The clad fibres were cleaved with a scissor into 5 mm short pieces. The fibre pieces were placed orthogonally on the specimen. The images were recorded on a Hitachi S4000 instrument.

4.2.3 Gas sensor measurements

Laboratory set-up for testing the ammonia sensing probes. A clad fibre was placed in a flow cell as shown in Figures 1 and 2. The fibre was illuminated from the top by a 0.06 W LED with a peak wavelength of 470 nm (FWHM bandwidth 25 nm) purchased from Industrial Fiber Optics. To measure fluorescence emission, the photodetector (a phototransistor from Thorlabs) was placed in line to the incoming radiation at the end of the fibre. Additionally, an optical longpass filter was placed in front of the detector, which only allowed passage of light above 550 nm (FEL0550; Thorlabs). Electronic readout was based on a phototransistor circuit and a LabView-controlled digital multimeter. The gas flow could be switched between NH_3/N_2 mixture and N_2 using manual valves. During the experiments, the flow rate (800 mL/min ± 50 mL/min), the temperature (20 ± 2 °C), and the humidity (< 4%) were monitored in the line using a CMOSens EM1 (Sensirion) and an MSR 145 (Sensirion) respectively. Custom mixed gases 49.7 ppm ± 2% rel. NH_3, 99.6 ppm ± 2% rel. NH_3, 504.9 ppm ± 2% rel. NH_3, 0.101 ± 1% rel. NH_3 in N_2 (≥ 99.8%) and pure N_2 gas were acquired from Carbogas.

Measurement and measurement evaluation. Before the measurements were started, the system was flushed with N_2 gas for 5 min. An experiment always started with a 300–600 s N_2 gas flush followed by a flush with an NH_3 gas mixture. The amplification of the electronic and the LED light intensity was constant for each measurement. Raw data from the cycle measurements were plotted in Microsoft Excel and illustrated without further processing.

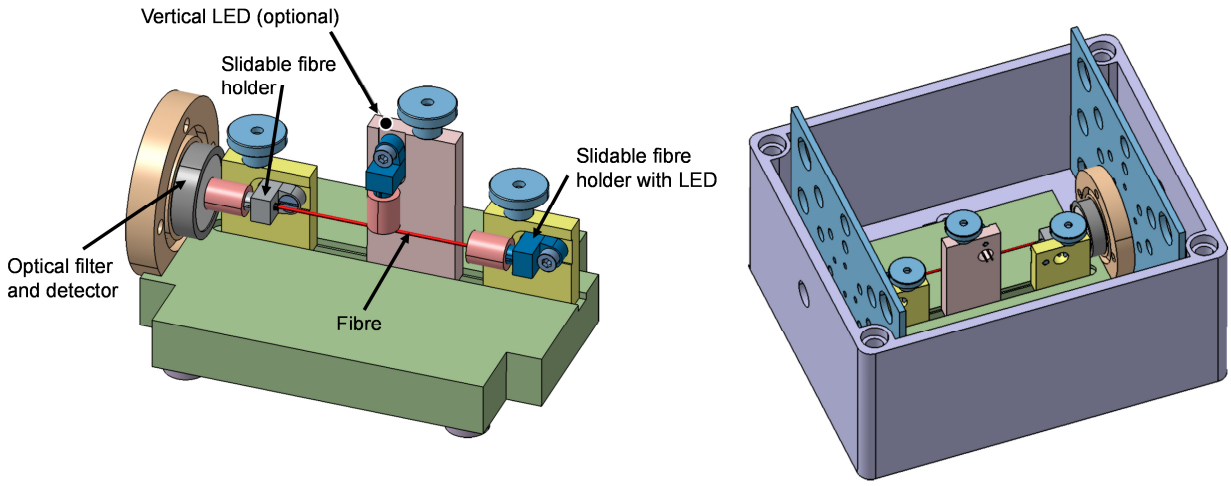

Figure 1: Schematic illustrations of the fibre gas sensor setup.

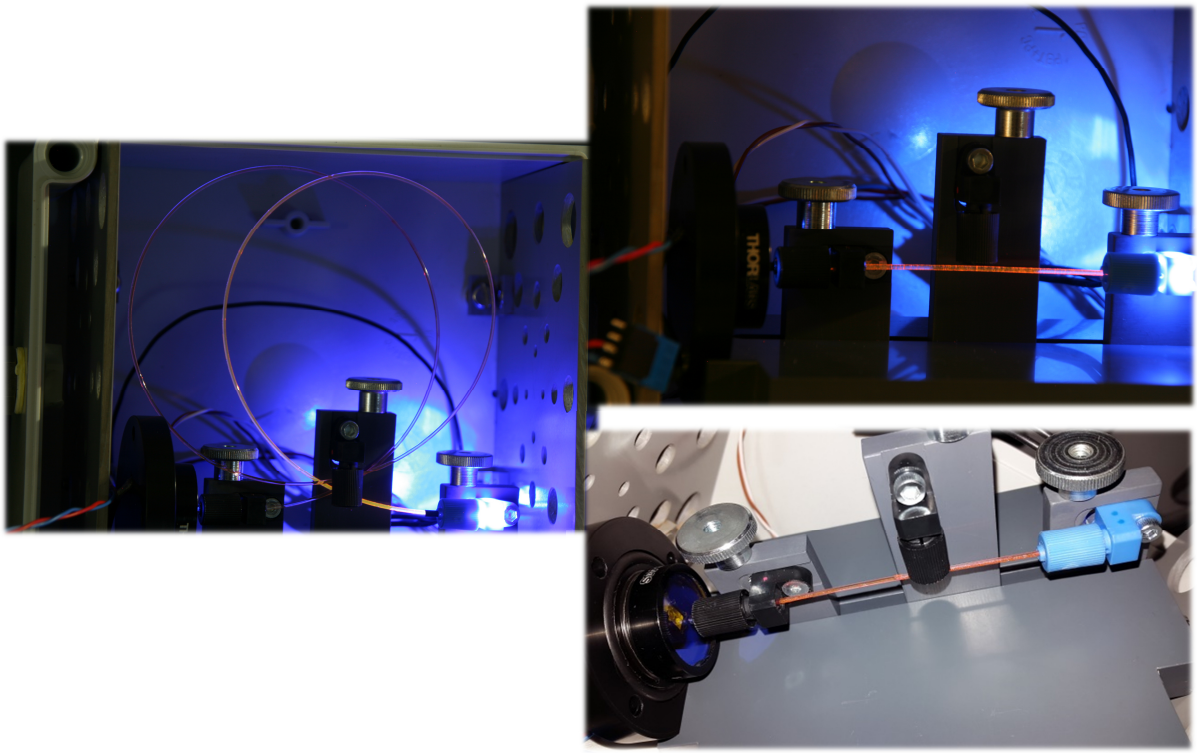

Figure 2: Photographs of the fibre gas sensor setup.

4.3 Results and Discussion

4.3.1 Fibre cladding

The manual dip-coating led to homogenous coatings (Figure 3, a and b). Comparing the fibre in image a with the fibre in image b, it is obvious that a second dip-coat led to a thicker cladding due to the more intensive characteristic pink colouration. A single dip-coat yielded a cladding thickness of 4 ± 2 µm. The cladding thickness of a twice dip-coated fibre was probably in the range of 8 µm. The cladding of the fibre in image c was obtained when SBA-15 particles were trickled over the fibre after the dip-coating procedure.

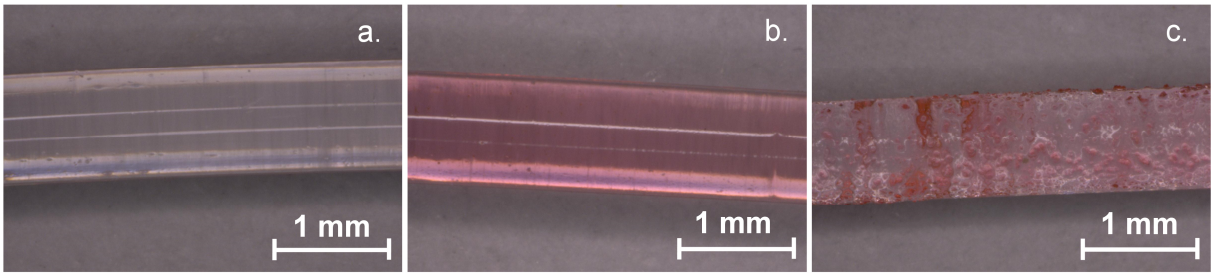

Figure 3: Optical microscopy images of xerogel clad fibres: a.: single dip-coated fibre; b.: twice dip-coated fibre; c: dip-coated fibre with integrated SBA-15 particles.

4.3.2 Ammonia response

When light is guided in an optical fibre, a fraction of the radiation extends a certain distance from the guiding core region into the medium with a lower refractive index (n of PMMA fibre = 1.49, n of unlabelled xerogel = 1.404). This evanescent field interacts with the fluorescent dyes in the cladding by exciting them and coupling their fluorescence intensity into the core of the waveguide. The evanescent-wave interaction changes in the presence of NH_3 due to the change in absorption and fluorescence characteristics of the dyes in the cladding leading to a modified light reaching the detector. In the case of the reported FITC/RBITC FRET system, more excitation light is absorbed due to the formation of FITC dianions that leads to an enhanced fluorescence intensity (FITC and RBITC fluorescence) of the cladding that is coupled into the waveguide. The RBITC fluorescence was monitored using a longpass filter.

The ammonia response was measured for a 9 cm straight fibre and a 60 cm long coiled fibre. The shape can have an influence on the light penetration depth

into the cladding and an increase in angle of incidence increases the number of skips of the propagating radiation along the core-cladding interface per unit fibre length.[8] However, the total internal reflection of the radiation modes is affected due to the bending of the fibre which leads to a loss of a few radiation modes into the environment.[8] This results in a reduction of the net radiation propagating along the coiled fibre with the attendant decrease in signal-to-baseline ratio (baseline = fluorescence in absence of NH_3). The length of the fibre determines the net absorption/fluorescence path length which is linked to the number of skips of the radiation propagating along the fibre core.[8] The fluorescence intensity change was ca. 1.1-fold for the long coiled fibre and 1.15-fold for the short straight fibre (Figure 4). Since the fibres did not have the same length, shape and probably not exactly the same cladding thickness due to the manual dip-coating procedure, clear correlations of sensitivity to the fibre properties could not be commented at this stage of investigation on the NH_3 response. However, the response time (defined as the time required to achieve 95% of the maximum fluorescence signal increase upon exposure to ammonia) was below 4 min and the recovery time was below 15 min. Therefore, response and recovery time were shorter for the fibre sensor platform than for the planar sensor platform reported in Chapters 2 and 3. This can be explained by the thinner xerogel cladding on the fibre which leads to a shorter diffusion distance and thus faster diffusion of NH_3 and N_2 into the cladding. Furthermore, the fibre sensor platform could be more effective for the physical processes taking place during the sensing procedure.

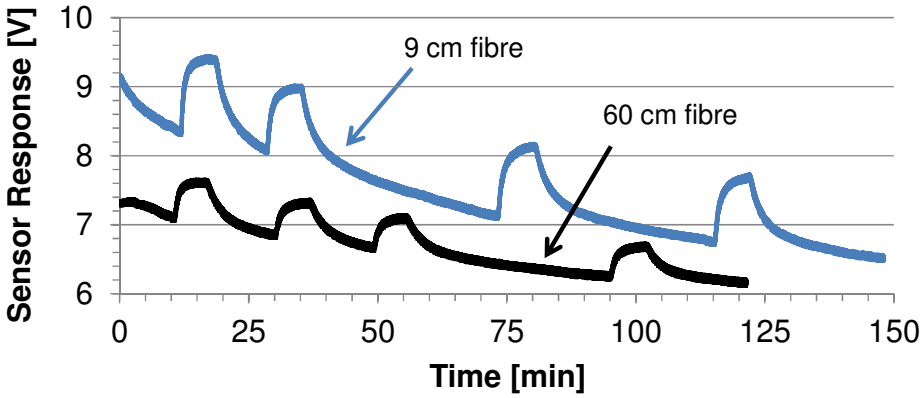

Figure 4: Sensor response of a single dip-coated straight 9 and coiled 60 cm long fibre to 500 ppm NH_3.

Figure 5 shows the response of the short fibre to three different NH_3 concentrations. The sensor performed good reproducibility of the signals. The sensor displayed the tendency to a logarithmic increase in the sensor response with increasing ammonia concentration which was expected from the results on the FITC/RBITC sensor coatings reported in Chapter 3. Figure 6 illustrates the response of a short and SBA-15 impregnated fibre twice to 500 ppm NH_3. The significant longer recovery time can be explained according to Section 3.3.6. Xerogel coatings with integrated particles exhibited long recovery times which were explained in terms of NH_3 adsorption on the silanol rich silica surface. The recovery with N_2 gas after the first NH_3 exposure cycle was too short for the complete recovery of the sensor response which led to a smaller sensor response in the second NH_3 exposure cycle.

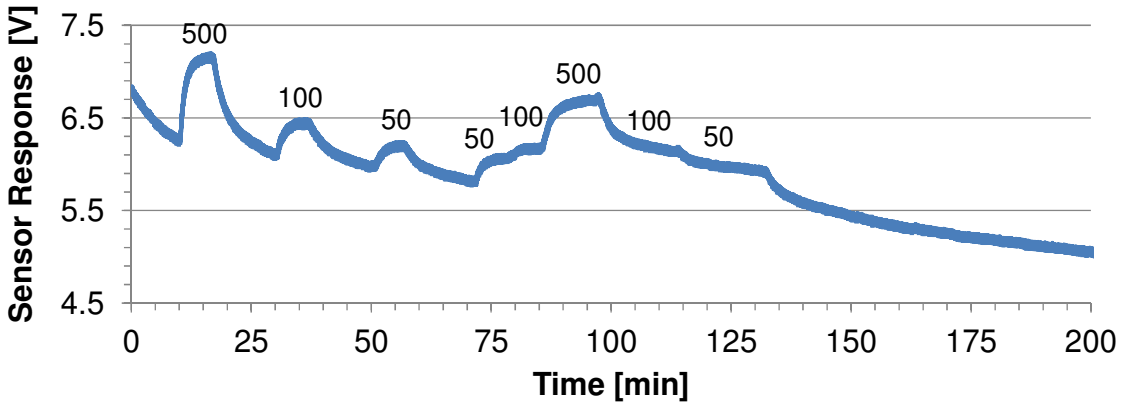

Figure 5: Response of a 9 cm single dip-coated fibre to different NH_3 concentrations. The numbers above the signals refer to the NH_3 concentration (50, 100 and 500 ppm).

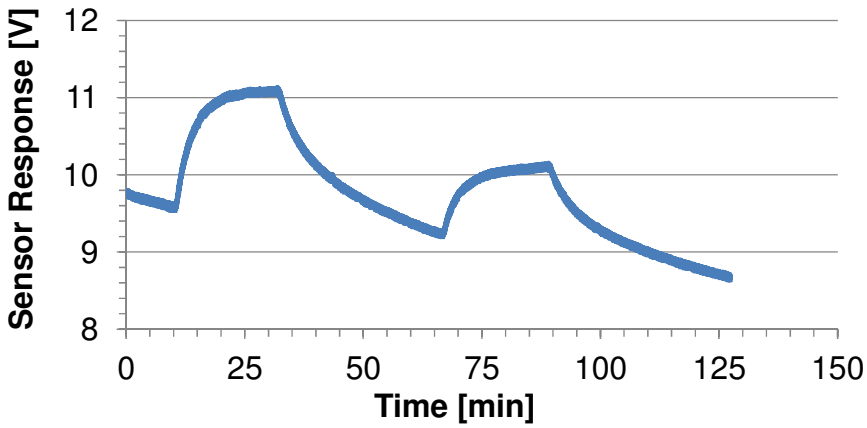

Figure 6: Response of a 9 cm long, with SBA-15 impregnated fibre to 500 ppm NH_3.

4.4 Conclusions

The optical fibre gas sensor demonstrated a promising sensitive and reversible sensor performance. Compared with the plate sensor platform this fibre sensor platform exhibited a similar sensitivity but shorter response and recovery times. This could be explained by the shorter diffusion distance due to the thinner xerogel cladding on the PMMA fibre substrate leading to faster complete diffusion of NH_3 and N_2 into the cladding. Another reason could be that this sensor platform is more effective for the physical processes taking place during this sensing procedure. More studies on cladding thickness, fibre properties and kind of fibre installation (straight, coiled or as a fibre bundle) should be performed in order to further improve the fibre sensor performance. Since the manufacturing process for integrating the fibre into the fabric might damage the xerogel-based sensing fibre cladding, the robustness of the cladding has to be investigated.

4.5 References

1 W. Cao and Y. Duan, *Sens. Actuators, B*, 2005, **110**, 252-259.
2 B. Renganathan, D. Sastikumar, G. Gobi, N. R. Yogamalar and A. C. Bose, *Opt. Laser Technol.*, 2011, **43**, 1398-1404.
3 Y. Huang and S. Tao, *J. Sensor Technol.*, 2011, **1**, 29-35.
4 T. Grady, T. Butler, B. D. MacCraith, D. Diamond and M. A. McKervey, *Analyst*, 1997, **122**, 803-806.
5 L. Peng, X. Yang, L. Yuan, L. Wang, E. Zhao, F. Tian and Y. Liu, *Opt. Commun.*, 2011, **284**, 4810-4814.
6 J. Rantala, J. Hännikäinen and J. Vanhala, *Pers. Ubiquit. Comput.*, 2011, **15**, 85-96.
7 S. Widmer, M. J. Reber, P. Müller, C. E. Housecroft, E. C. Constable, R. M. Rossi, D. Brühwiler, L. J. Scherer and L. F. Boesel, *Analyst*, 2015, **140**, 5324-5334.
8 P. G. Lye, M. Boerkamp, A. Ernest and D. W. Lamb, *J. Phys. Conf. Ser.*, 2005, **15**, 262-269.

Chapter 5

Conclusions and Outlook

The first part of this thesis contained the development of PMMA doped with a xerogel coating containing a C/F FRET dye pair. The performance of this FRET-based sensor system showed linear response on a wide range (40–40,000 ppm) of NH_3 concentrations. This linearity was not achieved when fluorscein alone was used to dope the xerogel coating. The potential of this FRET system as an NH_3 sensor was successfully demonstrated using an in-house built optical flow cell sensor setup. The sensor performance was dependent on the dye concentration in the film and on the film thickness. These results led to a better understanding of the sensor film properties required for promising gas sensor measurements. The negative sensor response to NH_3 was the major drawback of this FRET system since a loss in fluorescence can have other reasons such as photobleaching and sensor drift. FRET sensor systems exhibiting a gain in fluorescence in presence of the analyte are recommended since they do not suffer from these issues.

The second part of this thesis explored the integration of mesoporous silica particles into the non-porous xerogel sensor coating. The aim of this approach was to enhance the porosity of the xerogel film in order to fasten the NH_3 diffusion which ideally leads to shorter response and recovery times of the flow cell gas sensor. In a prestudy, MCM-41 particles were labelled with possible FRET dye pairs. The fluorescein/rhodamine FRET dye pair was found to respond to NH_3 by an increase in rhodamine fluorescence intensity. This FRET system was applied to SBA-15 particles. The structure properties, the amount of dye and the NH_3 sensing performance were compared for post-grafted and co-condensed SBA particles. The introduced porosity by the integration of the particles into the xerogel led to shorter response times but to longer recovery times which was explained in terms of the structure and surface properties (more or less silanol groups) of the corresponding SBA material. Passivation of the free silanol groups on SBA would possibly lead to a reduced adsorption of the NH_3 molecules. Furthermore, varying the structure properties of SBA by changing the synthesis conditions or the sample processing may improve the final sensor performance. It would be interesting to compare the sensor performance of the mesoporous system with micro- and macroporous systems.

The relative change in rhodamine emission intensity upon ammonia exposure was similar for F/R-labelled particle impregnated xerogels and FITC/RBITC-doped xerogel coatings. However, the absolute response was higher for the FITC/RBITC xerogel coating which led to better sensitivity and enhanced resolution of the optical sensor.

In the last part of this thesis, the evolved FITC/RBITC FRET sensor system was applied to an optical fibre sensor platform. A flexible PMMA fibre was clad with the corresponding xerogel by manual dip-coating. The sensitivity was comparable with the plate sensor platform. The shorter response and recovery times were explained considering the shorter diffusion distance due to the thinner xerogel coatings. Furthermore, this sensor platform could be more effective for the physical processes taking place during this sensing procedure. More studies on the cladding thickness, fibre properties and fibre installation (straight, coiled or fibre bundles) should be performed in order to further improve the fibre sensor performance. An ammonia gas sensor based on one or multiple flexible fibres would be suitable for being integrated directly into fabrics. In this way, a wearable gas detection for gas-protective clothing could be engineered.

A chemical sensor consists of three main elements: (1) a chemical sensor part, that interacts directly with the analyte; (2) an optical platform that transforms the chemical signal into an optical signal; (3) electronic components which transform the optical signal into an electrical signal and (4) a signal processing software, which transforms the raw signals in a filtered and readable output. Both, the fibre gas sensor and the plate gas sensor worked properly, this is where the focus of this work was. Until this stage of research, the sensor electronics was designed in a tunable manner in order to stay flexible in the FRET systems. In a next step, the sensor electronics and the signal processing should be adapted to one particular FRET system and one particular sensor platform. An improved electronic platform would provide the precondition to work with thinner sensor coatings which are necessary for shorter response and recovery times of the sensor. Furthermore, the fibre gas sensor or plate gas sensor prototype should be miniaturized, especially if a textile integration is envisaged. Additionally, the electronic components such as LED, the photodetector, the compensation and amplification circuits as well as the processor can be installed on one single chip which ensures the same environmental conditions for each electronic component and

minimizes the external disturbances. The influence of temperature and humidity can be compensated with the integration of corresponding sensors on the same chip. The selectivity of this miniaturized sensor system to other common gases should be investigated and improved with chemical or physical methods if necessary.